FEUP FACULDADE DE ENGENHARIA
UNIVERSIDADE DO PORTO

Study of Tube Rotary Draw Bending Process: Experimental and Numerical Analysis for Different Metallic Materials

Author:
Maria Nunes e Almeida

Supervisors:
Ana Reis

Co-supervisors:
Daniel Cruz
Rui Amaral

Master in Mechanical Engineering - Manufacturing
Faculty of Engineering of the University of Porto

DEMec, Faculdade de Engenharia da Universidade do Porto, Rua Dr. Roberto Frias, 4200–465 Porto, Portugal

Porto, 2025

Departamento de Engenharia Mecânica
Faculdade de Engenharia da Universidade do Porto

Rua Dr. Roberto Frias, s/n
4200-465 Porto
Portugal

Abstract

The Rotary Draw Bending (RDB) process is widely used in industry for the precise forming of metallic tubes. However, springback after plastic deformation compromises dimensional accuracy, requiring careful compensation in tooling design and process parameters. With increasing demands for lightweight structures and complex geometries, optimising the bending process has also become crucial to improve the product quality and reduce material waste.

This thesis aims to characterise the springback behaviour and the elongation induced during the RDB process, in order to understand the factors influencing elastic recovery and strain distribution in the bent tube. Numerical simulations using finite element method in ABAQUS were carried out on metallic tubes made from different materials, with a focus on SS304, S235, Fe510, AL2017A and Ti 99.5. Additionally, a series of experimental tests were conducted using SS304 and S235 materials with thicknesses of 1.5 mm and 2 mm, in order to evaluate the influence of variables such as centerline radius (CLR), bending angle, and final elongation. It was concluded that the CLR has a significant impact on springback behaviour. The influence of tube thickness was analysed for 1 mm, 1.5 mm and 2 mm tubes numerically but only minor differences were observed - the maximum 0.86 mm between thicknesses for ΔCLR when using Al2017A, corresponding to an error of 3.87%.

Higher CLR values correspond to increased springback in radius, whereas lower CLR values result in greater springback in angle. This trend was seen in both numerical and experimental results, though there was a discrepancy in the magnitude of the results. This study enhances dimensional control in the RDB process by proposing data-driven guidelines based on experimental evidence and advanced modelling techniques.

Keywords: Springback; Tube bending; Finite element simulation; Experimental validation; Numerical simulation.

Resumo

O processo de dobragem por estiramento rotativo é amplamente utilizado na indústria para a conformação precisa de tubos metálicos. No entanto, o retorno elástico após a deformação plástica compromete a precisão dimensional, exigindo uma compensação cuidadosa no projeto das ferramentas e nos parâmetros do processo. À medida que aumenta a procura de estruturas leves e geometrias complexas, torna-se crucial otimizar o processo de dobragem para melhorar a qualidade do produto e reduzir o desperdício de material.

Este projeto tem como objetivo caraterizar o comportamento do retorno elástico e o alongamento induzido durante o processo de dobragem, de modo a compreender os factores que influenciam a recuperação elástica e a distribuição de tensões no tubo curvado. Foram efectuadas simulações numéricas utilizando métodos de elementos finitos no ABAQUS em tubos metálicos de diferentes materiais, com destaque para SS304, S235, Fe510, AL2017A e Ti 99.5. Adicionalmente, foi efectuada uma série de ensaios experimentais com dois materiais (SS304 e S235) com espessuras de 1,5 mm e 2 mm, com o objetivo de avaliar a influência de variáveis como CLR, o ângulo de dobragem e o alongamento final. Concluiu-se que o CLR tem um impacto significativo no comportamento do retorno elástico.

A influência da espessura do tubo foi analisada para tubos de 1 mm, 1,5 mm e 2 mm, mas apenas foram observadas pequenas diferenças - o máximo de 0,86 mm entre espessuras para ΔCLR quando se utiliza Al2017A, correspondendo a um erro de 3,87%. Para valores mais elevados de CLR observou-se um maior retorno elástico no raio, enquanto que para valores mais baixos de CLR um maior retorno elástico no ângulo. Esta tendência foi observada em ambos os resultados numéricos e experimentais, embora tenha havido uma discrepância na magnitude dos resultados. Este estudo melhora o controlo dimensional no processo RDB, propondo diretrizes baseadas em dados e em provas experimentais e técnicas de modelação avançadas.

Palavras-chaves: Retorno elástico; Dobragem de tubo; Simulação de elementos finitos; Validação experimental, Simulação numérica.

Acknowledgments

I would like to start by thanking Dr. Ana Reis for making it possible for me to take part in this project and also for the encouragement during the process.

Secondly, i thank AMOB for the availability, support and help whenever necessary specially Eng. Pedro Oliveira e Eng. Pedro Cortez.

Next, I am grateful for my co-advisor Eng. Daniel Cruz who was always available to accompany me during AMOBs training and to answer questions at every stage.

Additionally, I want to thank Dr. Rui Amaral who was a crucial part in the meetings with his great ideas and even when I needed help with the simulation.

I want to thank Dr. Roya, Dr. Marco Parente, Sr. Rui and Prof. Miguel Figueiredo for all the support during this process whether it was in the workshop or in the simulation part.

To my friends, Beatriz, Miguel, Francisco, Vasco and Pedro, who accompanied me throughout the process and didn't let me give up. Thank you so much.

Finally, I would like to express my gratitude to my parents, without whom none of this would have been possible. I also want to thank my sister and brother-in-law for their insights, both professional and personal, on the subject. Last but certainly not least, I am deeply grateful to my boyfriend, who listened to my thoughts, frustrations, and reflections about the project over the past six months, and who supported me during the times when things didn't go as planned.

Thank you all for being part of this journey and may there be more challenges to come.

Institutional Acknowledgements

The author gratefully acknowledges the funding of Project "Smartubending - Curvadoras inteligente efi-cientes e conectadas" (COMPETE2030-FEDER-01480000) co-financed by COMPETE 2030, Portugal 2030 and European Union.

2030 Sustainable Agenda Framing

Given the objectives and scope of this thesis, analysing phenomena such as springback and stretching in the RDB process, specifically when using an eMOB (electrical bending machine), represents a significant advancement in sustainability within the tube bending industry. This research aligns with several of the 17 Sustainable Development Goals (SDGs) outlined in the United Nations' 2030 Agenda for Sustainable Development, such as:

- Goal 7. Affordable and Clean Energy: The use of electric tube bending machines enhance energy efficiency and sustainability in manufacturing. Unlike traditional hydraulic or pneumatic systems, they consume power only when needed, reducing energy usage and emissions. This approach lowers the manufacturing carbon footprint and supports the integration of renewable energy sources, aligning with global sustainability goals.

- Goal 9. Industry: Innovation, and Infrastructure. By the development of more efficient bending processes and improved understanding of material behaviour, such as springback and stretching.

- Goal 12. Responsible Consumption and Production: Improving the understanding of springback and stretching during forming processes can reduce material waste from overcompensation, trial-and-error, and rejected parts. This results in more precise manufacturing, better resource utilisation, and a lower environmental impact.

Contents

List of Figures

List of Tables

List of Acronyms

DoE	Design of Experiments
FE	Finite Element
FEA	Finite Element Analysis
FEM	Finite Element Method
RDB	Rotary Draw Bending
SB	Springback
UTS	Ultimate Tensile Strength
YS	Yield Strength

List of Symbols

α	Bending angle of the tube after unloading (after springback)
α_i	Bending angle of the tube before unloading (before springback)
$\Delta\alpha$	Springback angle
CLR	Centerline radius of the tube after unloading (after springback)
CLR_i	Centerline radius of the tube before unloading (before springback)
ΔCLR	Springback radius
ΔL	Difference between total length of the tube before and after springback
L	Length of the tube after unloading (after springback)
L_i	Length of the tube before unloading (before springback)
t	Tube thickness
D_e	Neutral Layer Position
D	Outsided diameter of the tube
K	Strength Coefficient
R_{out}	Outer radius
R_{in}	Inner radius
σ_0	Yield stress
E	Young's Modulus
ν	Poisson's ratio
d	Inside diamter of the tube
n	Hardening Exponent

Chapter 1

Introduction

Rotary draw bending (RDB) is a widely adopted metal forming technique, particularly in industries such as aerospace, automotive, and general manufacturing, where high-precision tube bending is essential [1]. With the growing demand for lightweight structures and complex geometries, optimising the RDB process has become increasingly important to enhance product quality and minimise material waste [2]. Figure 1.1 illustrates the fundamental stages of the RDB process, including the springback phenomenon, which constitutes the primary focus of this study. Through tube bending, the material undergoes elastic-plastic deformation, upon unloading, the elastic component of the deformation is partially recovered, leading to springback, a geometric deviation from the intended final shape. Understanding and mitigating this effect is critical for achieving accurate and repeatable bend geometries in advanced manufacturing applications. In Figures 1.2a and 1.2b, it is possible to visualise some of these applications [3].

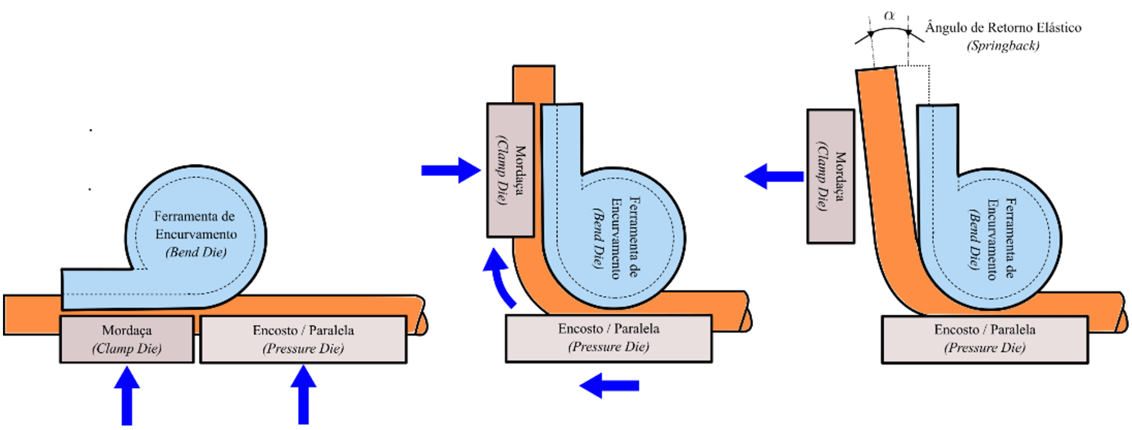

Figure 1.1: Representation of RDB process and springback phenomenon, adapted from [4].

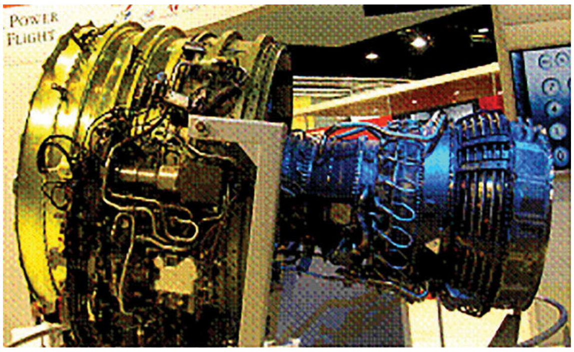

(a)

(b)

Figure 1.2: Applications of RDB in different fields: a) Aeroengine [2] and b) Naval and offshore flowlines [5].

In RDB process, several other phenomena can arise such as: cracking, distortion, wall thinning and wrinkling. These phenomena are a result of uneven stress distribution between the intrados and extrados (Figure 1.3), ultimately compromising bend quality [2]. Many of these issues arise from operator-related errors, including the application of excessive force on the pressure die, which can misalign the wiper die and damage the mandrel. Additionally, improper tool selection, that result from incorrect sizing, material incompatibility, or inadequate setup, often contributes to premature tool wear and part rejection. Ensuring consistent, high-quality bends thus requires careful tool selection, proper setup, and regular maintenance [6].

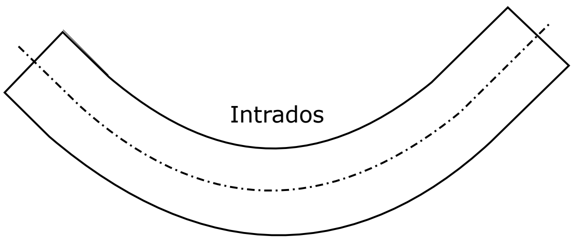

Figure 1.3: Intrados and Extrados, based on [7].

Figure 1.4 illustrates springback, a phenomenon of particular interest and a central key in this thesis, which can translate into changes in radius and/or angle in the final product. In addition to springback, tube stretching during the bending process is also investigated. Tube stretching happens when the length of the tube after bending is not the same as the starting tube. These phenomena are strongly influenced by several process parameters, including the centerline radius (CLR), tube diameter (D), wall thickness (t), and bending angle (α), all of which must be carefully considered to accurately predict and control the final tube geometry.

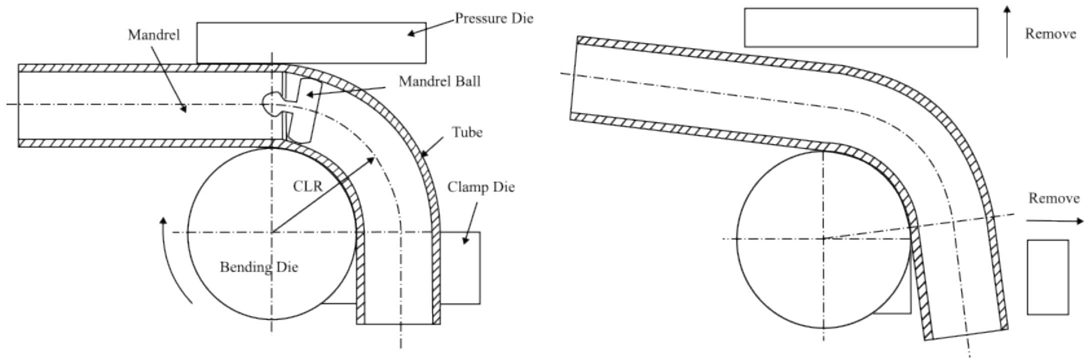

Figure 1.4: Representation of springback when bending a tube with RDB, adapted from [8].

Traditional methods for predicting and controlling these phenomena often rely on empirical approaches, which tend to be time-consuming and inefficient. To address these limitations, finite element models are increasingly used to provide faster and more accurate predictions. Finite Element Analysis (FEA) has become a valuable tool, especially for evaluating material behaviour under complex forming conditions [9]. Many commercial metal forming processes involve nonlinear material responses, significant deformation, and complex sliding contact between tools and workpieces, making FEA inherently complex.

To manage this complexity, different solution strategies are employed, notably implicit and explicit approaches. The implicit method is efficient for static and quasi-static analyses due to its unconditional stability with respect to time increment size. However, it struggles with discontinuous nonlinearities—such as stick/slip friction—where computational cost and memory usage rise sharply with model size, potentially causing convergence issues. On the other hand, the explicit method is advantageous for complex 3D contact problems. Its computational cost per increment scales with model size, and it avoids memory-related constraints. The size of each time increment depends only on element dimensions and material properties, not on model complexity [10].

An important consideration is whether parts are modelled as shells or rigid bodies. In the automation of finite element modeling (FEM), using deformable shell elements offers key benefits: they reduce manual error, enhance computational efficiency, and allow rapid adjustment across simulation scenarios. Furthermore, they provide reliable input for developing analytical models to predict process behaviour, thereby supporting optimisation of the tube bending process.

1.1 Motivation

The increasing demand for lightweight and strong components across various industrial sectors has driven the widespread adoption of tubular structures. RDB is one of the most prevalent techniques used to shape these tubes, because it can create precise bends with small radii and consistent quality. However, the RDB process is still complex, mainly due to the combined effects of springback and material stretching during bending.

Springback leads to deviations from the intended geometry, resulting in increased manufacturing variability, reduced dimensional accuracy, and the potential need for iterative tooling adjustments or costly post-processing. Accurate prediction and control of springback are essential to achieving the required tolerances, especially in high-performance applications where even minor geometric deviations can compromise structural integrity or assembly precision.

This thesis is motivated by the need to develop a deeper and more quantitative understanding of the springback and stretching phenomena in RDB processes, particularly for materials such as steel, aluminium and titanium alloys. By systematically analysing the influence of key parameters—such as bend radius, wall thickness, and material properties—this work aims to contribute to more accurate predictive models and better-informed process design decisions. The goal is to improve the geometric and mechanical quality of bent tubes while reducing manufacturing costs and enhancing process efficiency.

Ultimately, the findings of this research may serve as a foundation for optimising RDB in both simulation and pratical applications, facilitating the production of high-performance tubular components in demanding engineering environments.

1.2 Objectives

This thesis aims to study the RDB process using Finite Element Analysis (FEA), along with experimental validation. The goal is to achieve accurate results when bending a tube on the first try, which means having proper calibration of the bending angle, to correct springback and stretching, without manual adjustments.

To achieve the goals, it was established some sub-objectives for this thesis:

- Develop a numerical model to simulate the RDB process using the Finite Element Method;

- Analyse the influence of different metallic materials on the bending process, focusing on phenomena such as springback and tube stretching;
- Establish a Design of Experiments (DoE) to systematically study the effects of variables such as CLR, bending angle, material and thickness;
- Validate the numerical model by comparing simulation results with experimental data.

In a nutshell, the thesis aims to understand the RDB process and evolve the actual acknowledgement of this field, providing more useful information for the industry.

1.3 Structure of the Document

This thesis is divided into five chapters:

- Chapter 1 : Introduction

  Chapter one discusses RDB, the primary focus of this thesis. It outlines the thesis's objectives and the motivation behind it.

- Chapter 2 : State of art : Rotary Draw Bending Process

  Chapter two gives a contextualization of RDB and what have been developing in last years by analysing studies; it starts by explaining the process and its components; then defines the main variables for this thesis; and finally provides an overview of the possible defects with the analysis of several studies related.

- Chapter 3 : Methodology

  Chapter three provides a comprehensive overview of the tasks that were performed. It delves into the characterization of the materials, offers description of the FEM simulation, outlines the experimental methodology employed, and gives an explanation of the 3D digitalization processes. Each section aims to emphasise the importance of these tasks in relation to the research objectives and to convey the complexities involved in each methodological approach combined with 3D digitalization.

- Chapter 4 : Results

  Chapter four starts by presenting all the results from the simulation and the experimental test and the corresponding comparison, doing an initial analysis of them. Also details the validation of previous data through experimental methods.

- Chapter 5: Conclusions

  This chapter puts in a nutshell all the conclusions achieved during the development of this thesis and some possible future works.

Chapter 2

State of Art: Rotary Draw Bending Process

A tube is typically a long, narrow cylinder—or other similar geometry—with openings at both ends, commonly used for transporting liquids, gases, and other substances. Various manufacturing methods are employed in the production of circular tubes, including extrusion, roll forming, and butt-seam welding (e.g., electric resistance welded pipes). Tubes are essential components across a wide range of industrial sectors, driven by the increasing demand for lightweight, high-strength, and high-performance products.

To meet these requirements, several tube bending techniques have been developed, such as stretch bending, roll bending, push bending, compression bending, pure bending, laser bending, and rotary draw bending. Each method offers distinct advantages and is suited to specific materials, geometries, and application domains [2]. The choice of the most suitable process depends on factors such as thickness, diameter and application of the tube to be formed. Among these processes, RDB offers a good compromise between precision and repeatability of the result. Some innovations promote the transition from traditional hydraulic actuators to faster and more precise electric motors, increasing competitiveness in terms of productivity and efficiency [11].

Among the listed methods, RDB is considered the most precise, especially for applications involving thin wall thicknesses and small bending radii. However, the complexity of the process increases considerably with a decreasing centerline radius-to-diameter ratio (CLR/D) and an increasing diameter-to-thickness ratio (D/t), both of which negatively affect formability and dimensional stability [12].

As with all forming processes, RDB presents both advantages and limitations. With advancements in digital manufacturing technologies, computer numerical control (CNC) has been integrated into mandrel rotary draw bending (MRDB) systems to improve accuracy, repeatability, and automation. CNC integration enables precise control over bending parameters, facilitating high-volume production without compromising quality standards [13].

In Figure 2.1 represents the normal force applied in pressure die over the normalised bending angle, illustrating the process window for producing high-quality bent tubes is extremely narrow. This window corresponds to the most demanding bending operations—characterized by small radii and thin walls. The boundaries of this window are typically defined by two critical failure modes: cracking on the outer surface of the bend and wrinkling on the inner surface [12].

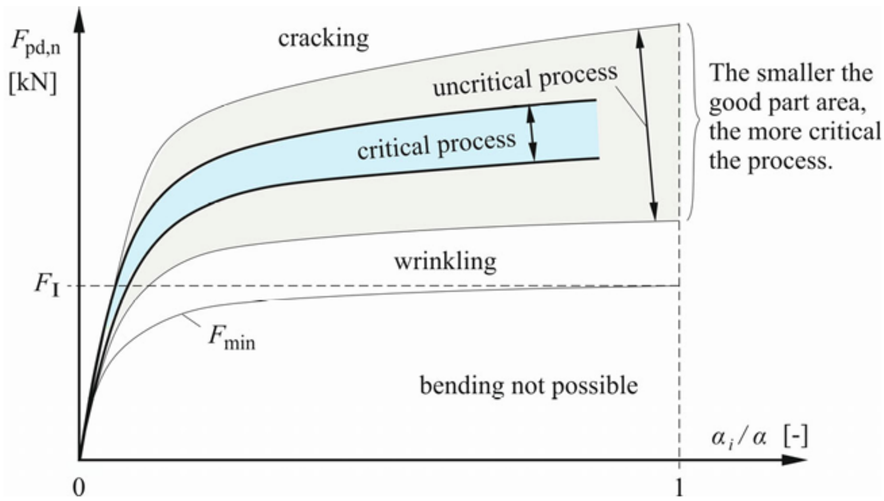

Figure 2.1: Process window of the pressure die's normal force $F_{pd,n}$ over the normalized bending angle α_i/α [12].

To fully comprehend the RDB process, it is essential to first understand the mechanical behaviour of the tube during bending. As shown in Figure 2.2a, the tube cross-section contains a region surrounding the neutral axis (NA) where the induced stresses remain below the material's yield strength, resulting in purely elastic deformation. In contrast, regions located further from the NA are subjected to stresses that exceed the yield limit, leading to plastic deformation. Plastic deformation implies that the material has surpassed its elastic limit and will not return to its original shape upon unloading [14]. A critical aspect of this deformation process involves the stress distribution across the tube wall. As shown in Figure 2.2b, tensile stresses develop on the extrados (outer region of the bend) due to stretching, while compressive stresses occur on the intrados (inner region) due to material compression. These opposing stresses are balanced at the neutral axis, where the net stress is theoretically zero. This stress gradient across the tube wall can result in undesirable effects such as wall thinning on the extrados and thickening or wrinkling on the intrados—phenomena that compromise structural integrity and dimensional accuracy of the bent tube.

The exact location of the neutral axis and the distribution of internal stresses are influenced by several parameters, including material properties, tube geometry, and tooling/machine setup. These factors collectively dictate the quality and final shape of the bent component. Bending hollow tubes presents greater complexity than bending solid bars or sheets, primarily due to the heightened risk of defect formation caused by the non-uniform stress state around the tube circumference [6].

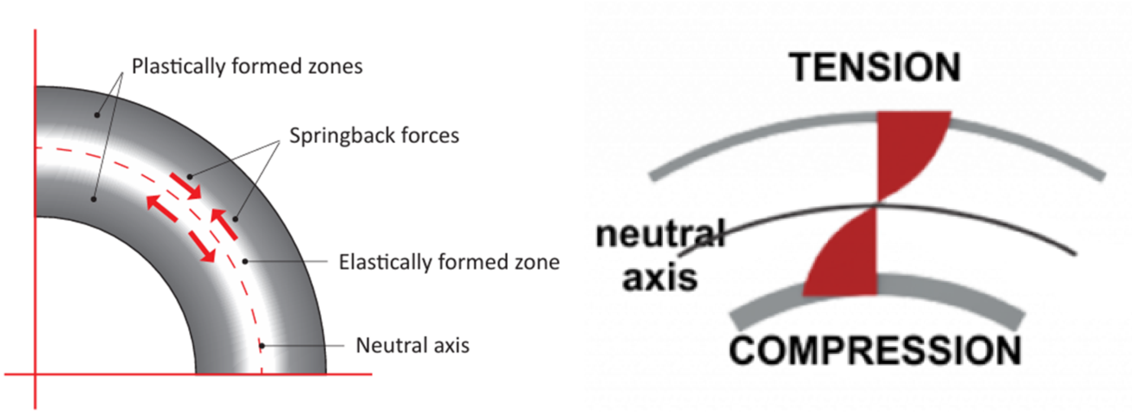

(a) (b)

Figure 2.2: Visual representation of: a) zones of plasticity and elasticity, with forces represented [14] and b) distribution of stress along the diameter of the tube [6].

2.1 Process and Components

Figure 2.3 illustrates a schematic representation of the typical RDB tool configuration and setup. The RDB process consists of several key steps: positioning the tube, securely clamping it, performing the bending operation using appropriate tooling, and subsequently unloading the formed part. To achieve accurate and defect-free bends, a combination of primary and auxiliary tools is employed. The clamp die, bend die, and pressure die are fundamental components of the tooling configuration, each playing a critical role in constraining, guiding and forming the tube. In addition to these, optional tools such as the mandrel, wiper die, and booster may be used depending on the application and material. These auxiliary components are specifically designed to minimise common defects such as wrinkling, wall thinning, and ovalisation, especially in challenging bending scenarios involving tight radii or thin-walled tubes.

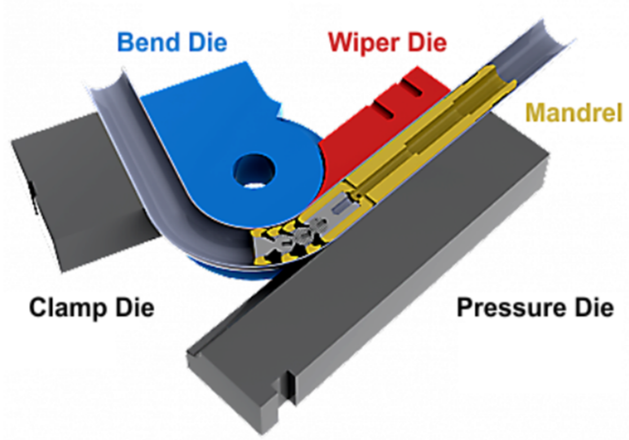

Figure 2.3: Setup representation of rotary draw bending manufacturing process [6].

The clamp die plays a crucial role in preventing tube slippage during the RDB process. By securely pressing the tube against the straight portion of the bending die, it ensures a firm grip throughout the operation. This component moves synchronously with the bend die and contributes directly to defining the bending angle. The bend die itself is the central element of the setup, primarily responsible for determining the CLR of the bend.

The pressure die provides additional radial support and maintains contact with the outer surface of the tube. It travels longitudinally along the tube during bending and prevents excessive deformation by distributing forces evenly. The die includes a cavity tailored to the tube's diameter, allowing for controlled axial movement while maintaining contact pressure.

The wiper die is positioned at the intrados of the bend and is specifically designed to mitigate wrinkling, which is a common defect in tubes with thin walls and tight bend radii. Typically manufactured from copper or other soft alloy, the wiper die is considered a consumable component due to progressive wear from repeated friction and mechanical contact during operation.

The mandrel offers internal support to the tube and plays a key role in maintaining the structural integrity of the tube during bending. It helps prevent cross-sectional deformation and wrinkling on the intrados. Mandrels are typically made from aluminium-bronze or hardened chromium steel, and they are available in various configurations, including fixed and articulated (ball-type) designs. The selection of mandrel type and number of balls is often guided by empirical nomograms, such as the one shown in Figure 2.5, which was developed by SSAB [14], a global leader in advanced steel production. This nomogram considers key geometric parameters, including the D/t and CLR/D ratios. In addition to SSAB's guidelines, there are other manufacturers providing recommendations for tool and mandrel selection based on tube geometry and bending requirements.

The booster , which is not represented, applies a longitudinal thrust force in the direction of the bend. This axial force can be precisely adjusted before or during the bending operation to regulate material flow, reduce tensile elongation, and prevent wall thinning at the extrados.

The collet, which is represented in Figure 2.4, is the component that secures the tube within the bending machine's carriage or trolley. It ensures accurate positioning and consistent feed during the bending operation.

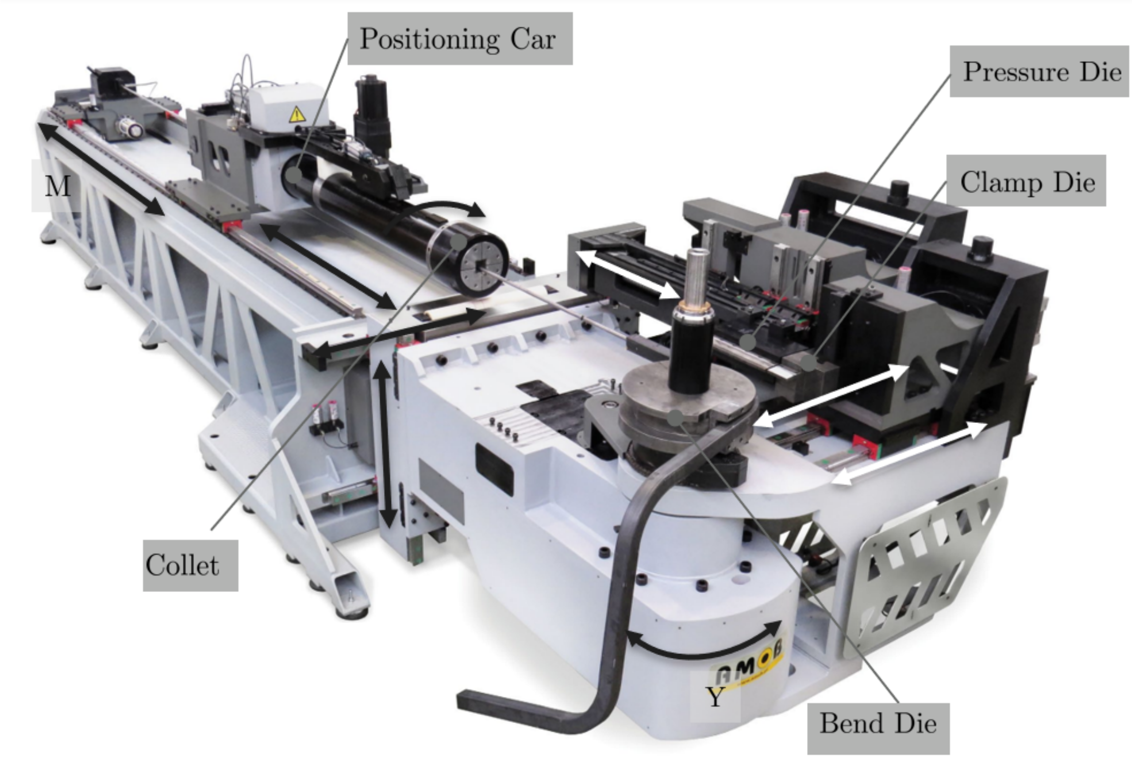

Figure 2.4: Representation of some components in a real Emob.

Finally, it is essential to emphasise that all of the previous tools must be appropriately sized and configured according to the specific tube dimensions (diameter, wall thickness, and material) to ensure high-quality and defect-free bending outcomes.

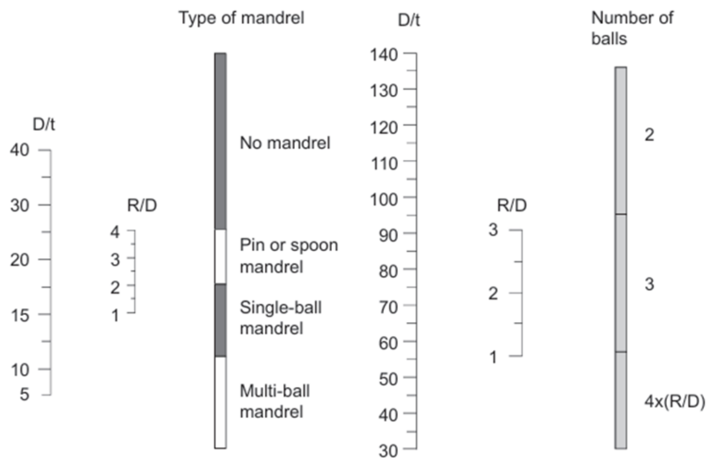

Figure 2.5: Nomogram that predicts the necessity of using a mandrel based on the D/t and CLR/D ratios [14].

2.1.1 Variable Definition

For the dimensions associated with the process, it is essential to establish a clear and consistent nomenclature for use throughout this thesis. Figure 2.6 illustrates the primary dimensions considered.

The geometry of the tube and the bend is characterised by the following parameters: outside diameter (D), inside diameter (d), wall thickness (t), outer radius (R_{out}), inner radius (R_{in}), centerline radius (CLR), bending angle (α), and bend length (L).

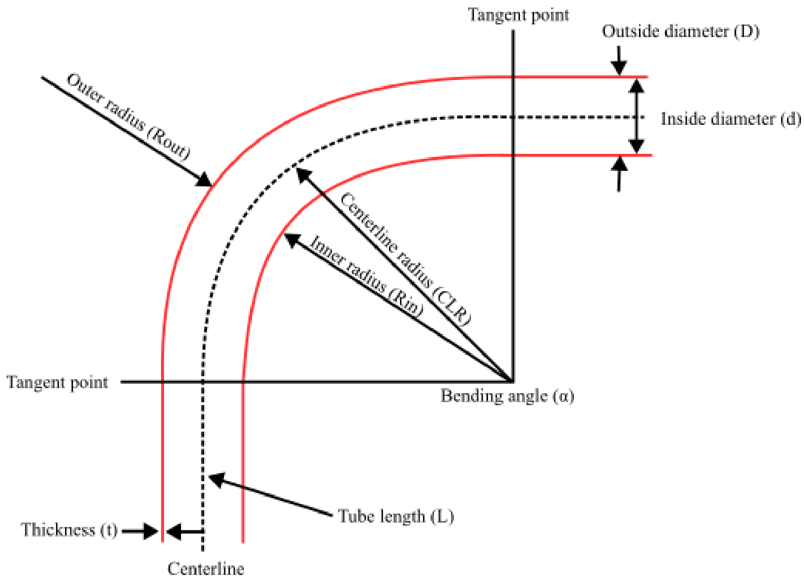

Figure 2.6: Schematic illustration of a bent tube with a graphical depiction of the applied nomenclature, adapted from [14].

Some of these variables will change during the process due to elastic recovery (springback) and material deformation, so it is necessary to account for their variation:

- CLR_i corresponds to the initial centerline radius, i.e. before the unloading (before springback) and CLR corresponds to the centerline radius after unloading (after springback);
- α_i corresponds to the initial bending angle, i.e. before unloading (before springback) and α corresponds to the bending angle after unloading (after springback);
- L_i corresponds to the initial length of the tube, i.e. before bending and L corresponds to the length of the tube after unloading (after springback).

In addition to the primary parameters, three derived variables are introduced to quantify critical effects of the bending process. The springback in angle ($\Delta\alpha$), which is defined in Equation 2.1. The springback in radius (ΔCLR) is defined in Equation 2.2. Finally, the tube elongation (ΔL) is defined in Equation 2.3.

$$\Delta\alpha = |\alpha - \alpha_i| \tag{2.1}$$

$$\Delta CLR = |CLR - CLR_i| \tag{2.2}$$

$$\Delta L = |L - L_i| \tag{2.3}$$

2.2 Phenomena that Influence the Geometry of the Product

In the RDB process, as in any manufacturing operation, defects may arise despite efforts to minimise or even eliminate them. These phenomena primarily result from uneven distributions of tension and compression stresses along the intrados and extrados of the tube during bending. Such stress affects the quality of the bend and consequently increases production costs. Common phenomena include cracking, cross-sectional distortion, wall thinning, wrinkling, and springback [2].

The quality of the bend is highly dependent of operator skills. For example, excessive force applied to the pressure die can cause displacement of the wiper die, leading to wrinkles and even mandrel cracking. Overloading the tooling not only accelerates tool wear but also imposes unnecessary stress on the bending machinery. Additionally, the use of damaged tools reduces the overall effectiveness of the bending system, as the performance and durability of the setup depend on the condition of all components. Bending with compromised tools not only generates higher scrap rates but also shortens tool lifespan considerably. Another critical source of defects is the improper selection of tooling. For instance, employing a mandrel that is undersized relatively to the tube diameter can result in wave-like deformations and wrinkles, potentially causing damage to the wiper die. Suboptimal material choices for tooling or incorrect tool configurations further degrade process performance. Therefore, ensuring correct tool selection, rigorous maintenance, and precise setup is essential to achieve consistent, high-quality bends [6].

Predictive systems have been developed to assess the risk of defects and optimise tooling configurations. A notable example is the system proposed by Strano [11], which integrates numerical methods, fuzzy logic, and empirical rules into a computer-based automatic process design framework. This system has demonstrated its effectiveness by producing feasible bending processes and high-quality products, as validated in trials conducted at Sicamb in Italy. However, it currently lacks the capability to evaluate the economic feasibility of the suggested processes.

Several specific phenomena are commonly encountered in tube bending:

- Cracking occurs when tensile strain exceed the material's ductility limits or when process parameters are improperly set. This defect typically appears on the outer bend radius (extrados), where tensile strain is highest.

- Wrinkling arises on the intrados due to compressive stresses that cause local thickening and instability, as illustrated in Figure 2.7a. Wrinkling compromises the tube's strength, stiffness, and fatigue life, while also accelerating tool wear and potential damage.

- Wall thinning on the extrados and wall thickening on the intrados are inevitable to some degree, as shown in Figure 2.7b. Although these effects can be mitigated, they cannot be fully eliminated and may lead to fracture if not properly controlled. The use of a mandrel helps manage the pressure distribution and reduce these defects [2].

- Cross-sectional distortion involves the deformation of the tube's originally circular cross-section into an oval or other irregular shape, depicted in Figure 2.7c. This distortion results from uneven force distribution during bending and can be minimised by employing internal supports such as mandrels [6].

- Springback refers to the elastic recovery of the tube after unloading, which reduces the bend angle or increases the bend radius, as shown in Figure 2.7d. This phenomenon diminishes bending accuracy and can negatively affect the fitting and sealing performance of the tube in its final application [2; 15].

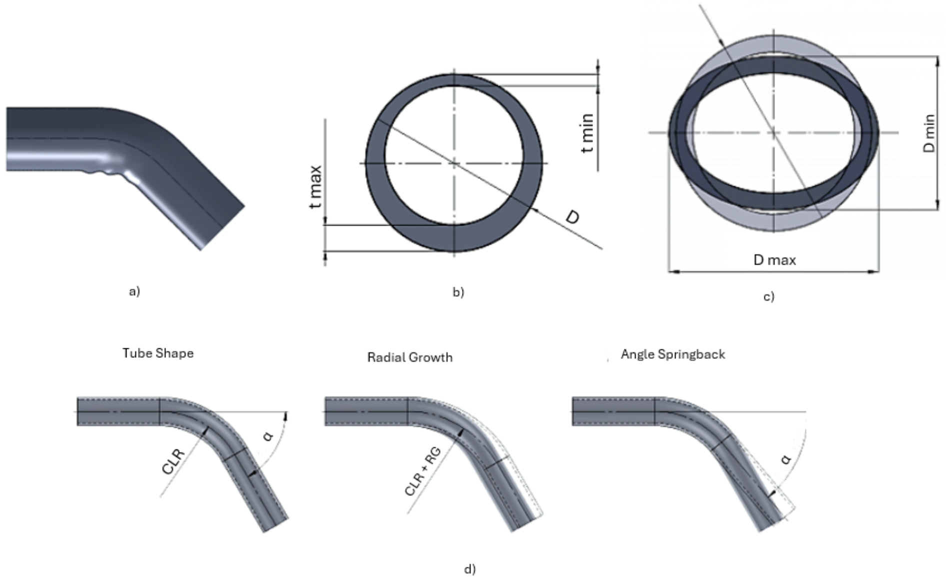

Figure 2.7: Main Defects found in bending process: a) Wrinkling; b) Wall thinning/thickening; c)cross-section distortion; d) Springback, adapted from [6].

Next, several studies on the relationship between certain defects and processing parameters will be analysed to support improved interpretation and discussion later.

As mentioned previously, wrinkling and cracking are key indicators for determining process limits. Borchmann et al. [12] present a fuzzy control system based on the forces applied during the bending process. This system utilises pressure dies and collet tools to prevent wrinkles without requiring operator intervention. The tools are calibrated to apply only the necessary force, which minimises tool wear and reduces the risk of cracking. Additionally, integrating thermal cameras could further decrease the likelihood of cracking by detecting critical temperature changes, as temperature gradients serve as indicators of potential cracks. Early detection can help address the issue before it escalates. In Figure 2.8, three different bends performed at varying speeds are shown, along with the temperature variation corresponding to each bend. For X5CrNi18-10 (1.4301), it can be concluded that higher speeds lead to higher temperatures and an increased probability of cracking and wrinkling.

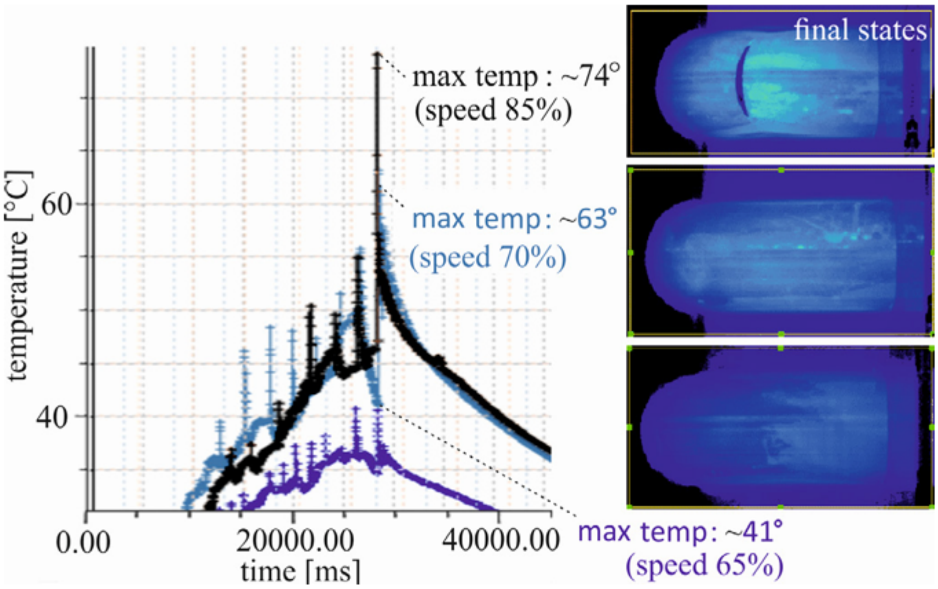

Figure 2.8: Maximum temperature at the outer tube bend throughout the entire bending process, considering variations in collet speed, along with corresponding thermal camera images, for X5CrNi18-10 (1.4301) with an outer diameter of 22 mm and a wall thickness of 1 mm [12].

Still concerning wrinkling defects, Li et al. [16] studied the influence of mandrel in such defects, when bending thin walled aluminium tubes. Their study reveals that tubes with larger diameters exhibit greater sensitivity to process parameters than those with smaller diameters. Furthermore, the mandrel's dimensions significantly affect this behaviour, a conclusion that is supported by finite element (FE) simulations presented in their work. Figure 2.9 illustrates the effect of mandrel extension on the wall thinning rate. It is evident that an increase in mandrel extension correlates with a higher thinning rate. The length of the mandrel extension is a critical parameter: insufficient extension length may result in wrinkling, whereas an excessively long mandrel can lead to fracture on the tube's outer surface [16].

In addition to the effect of mandrel extension, the same study conducted experiments to investigate the influence of the number of balls on both the wall thinning rate and cross-sectional distortion. The results are presented in Figures 2.10a and 2.10b. In the case of wall thinning, a lower number of balls yielded improved results, which can be attributed to the reduced friction between the balls and the tube. Fewer balls obstruct the material flow less, allowing increased tangential strain and consequently leading to less pronounced wall thinning. Conversely, regarding cross-sectional distortion, a higher number of balls resulted in a reduced percentage of distortion. This improvement is likely due to the enhanced support provided by a greater number of balls, which helps maintain the circular shape of the tube more effectively [16].

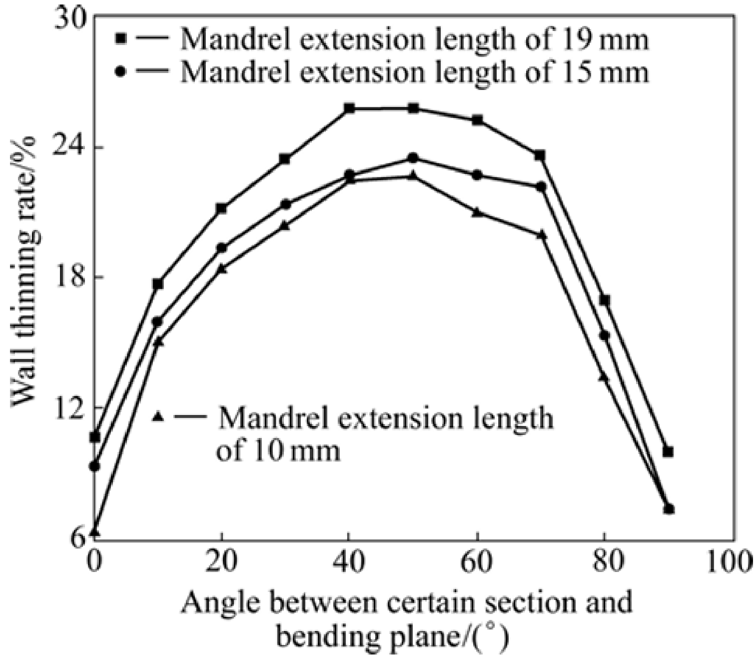

Figure 2.9: Influence of the extension of the mandrel with 2 balls in the wall thinning % [16].

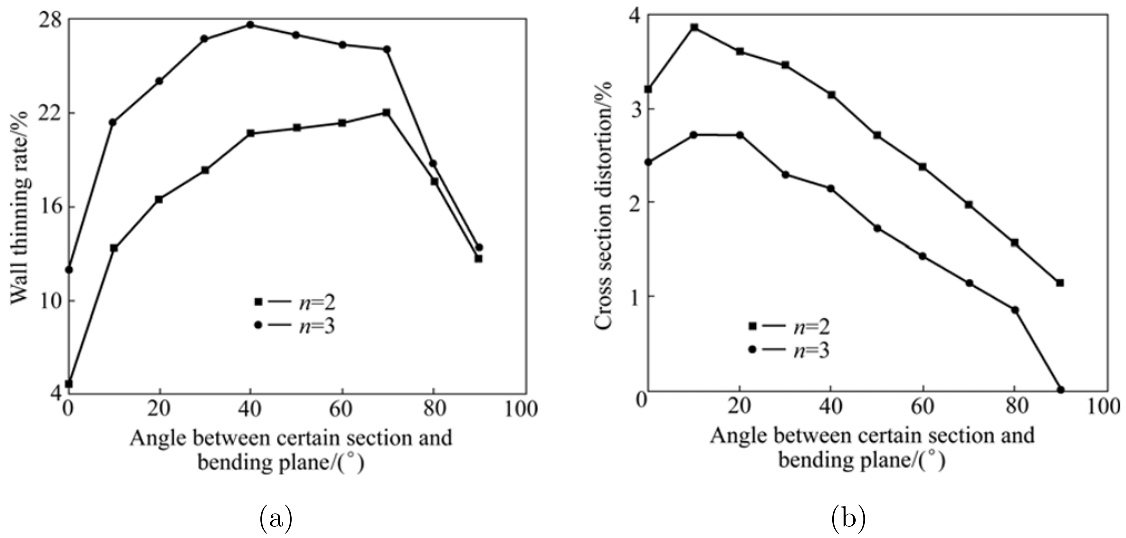

Figure 2.10: Influence of number of balls in the: a) wall thinning rate and b) cross-section distortion [16].

Considering that the diameter of the balls can also influence the result of the bend, so it was also conducted experiments using 2 balls in the mandrels, with different diameters, and the results are in Figures 2.11a and 2.11b. A ball with a smaller diameter yields better results for wall thinning because it produces less friction between the ball and the tube inner surface, resulting in lower tangential strain. However, this smaller diameter can also lead to more severe cross-section distortion, as it is less effective at maintaining the circular shape of the tube compared to a larger diameter [16].

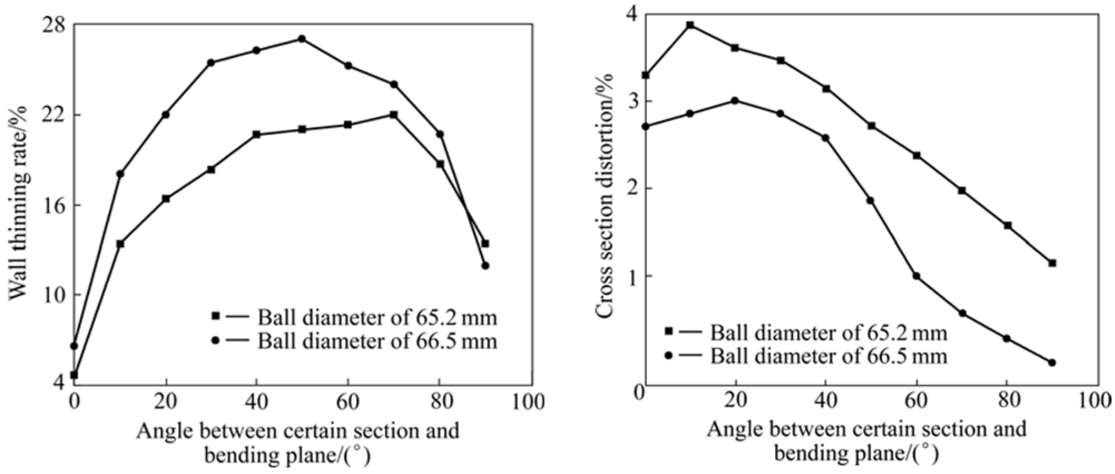

(a) (b)

Figure 2.11: Influence of diameter of balls in the: a) wall thinning rate and b) cross-section distortion [16].

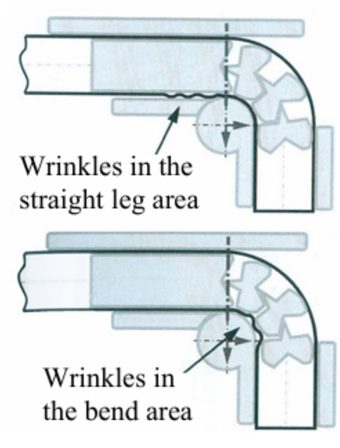

Figure 2.12: Differences in wrinkles areas [17].

A different approach regarding the wrinkling was explored by Borchmann et al. in 2019 [18], in which the detection of wrinkles was the focus. The study focused in the application of a laser line scanner, combined with a force measuring sensor in

RDB process, to detect them, both in straight area and in bend area as represented in Figure 2.12. The research was then improved, and new results were presented in 2020 [17].

In the first stage, the impact of the speed factor and the offset of the pressure die was analysed. For a better understanding of the speed factor: If the speed factor is 1, the distance travelled by the collet and the distance travelled by the tube are equal and if is 0.8, the distance travelled by the collet is 80% of the distance travelled by the tube [17]. With the results of Figure 2.13 it is possible to see the big influence of these parameters and the importance to achieve a perfect equilibrium of them. If the pressure die offset is 0 mm, the collet's velocity can be increased. However, if the pressure die offset increases, the collet's velocity needs to be lowered.

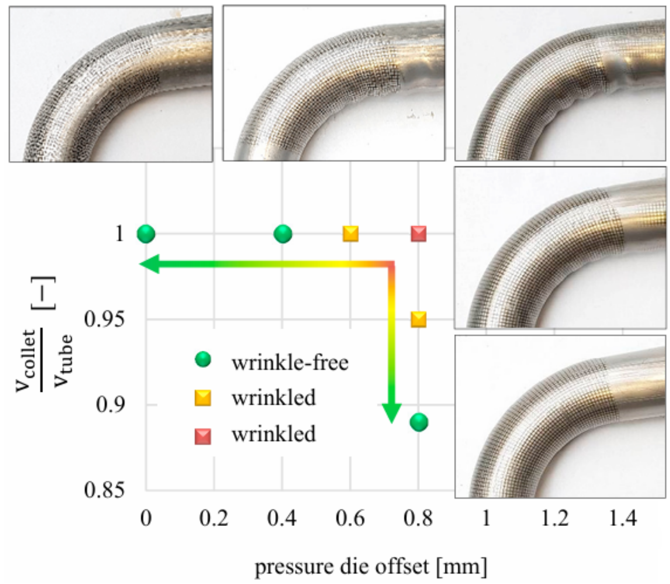

Figure 2.13: Influence of the pressure die offset and the collet velocity on the wrinkle development [17].

One established method for measuring and detecting wrinkles involves using a precision probe to trace the path along the bending angle. However, in this study, the second experimental stage employed a more comprehensive measurement system comprising three distinct pieces of equipment: a tension-compression sensor, a laser line sensor, and three load cells. The experimental tool setup used is illustrated in Figure 2.14. The tension-compression sensor was mounted on the mandrel to record the force profile acting on this tool. The laser line sensor was positioned behind the wiper die holder, ensuring that the laser line scanned the tube surface specifically in the wiper die region. Additionally, three load cells were installed: one on the pressure die, one on the mandrel, and one on the wiper die, enabling precise measurement of the forces exerted at each location. The test specimens consisted of X5CrNi18-10 (1.4301) stainless steel tubes, with an outer diameter of 40 mm and wall thicknesses of 2 mm, 1 mm, and 0.8 mm, respectively [17].

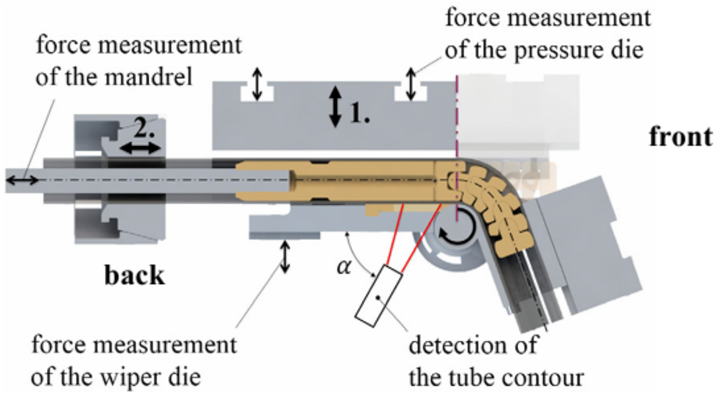

Figure 2.14: Schematic illustration of the experimental setup [17].

To gain a deeper understanding of the data, it is essential to analyse the correlation between the forces exerted on the wiper die and the occurrence of wrinkles in the straight leg area, as well as the relationship between the forces on the mandrel and the wrinkles in the bend area. These insights are derived from the analysis of the corresponding graphs. Figure 2.15 presents the force data on both the wiper die and the mandrel for the three mentioned material thicknesses, with variations in the offset position of the pressure die. In Figure 2.15a, it can be observed that, across the three pressure die positions, all measured forces increase. Notably, at the 333.4 mm position, the force shows a more significant increase at a bending angle of 60°. Figure 2.15b reveals that the number of wrinkles increases as the pressure die position is raised. The positions at 333.8 mm and 334.0 mm exhibit similar force behaviour and remain wrinkle-free. However, at the 334.2 mm position, wrinkles begin to appear at a bending angle of approximately 70°. A further increase to the 334.4 mm position leads to a marked change in forces at a bending angle of 55°, indicating the onset of wrinkle formation. In Figure 2.15c, the wrinkles become more pronounced at the highest position analysed (336.0 mm). At 335.8 mm, wrinkles start to form at a bending angle of 35°, though they are less severe in comparison [17].

On the other hand, Figure 2.15 illustrates the data for the same forces, this time focusing on the variation of the speed factor. Figure 2.15a shows that only noticeable wrinkles appear in the straight leg area. This indicates that the forces on the wiper die will be the first to experience any changes, even if those changes are not very significant. Notably, at 40°, there is a steeper increase as the speed factor rises. Figure 2.15b clearly demonstrates the effect of wrinkles in the straight and bent areas on the forces acting on the wiper die and mandrel, respectively. At a speed factor of 0.90, wrinkles are only detected in the bent area and changes in mandrel forces are only observable at 30°. However, at a speed factor of 0.94, both types of wrinkles are presented, but they are detected at different angles by different tools. The mandrel identifies the wrinkles in the bend area at 30° while the wiper die detects the wrinkles in the straight area at 80°. Figure 2.15c shows only wrinkles in the straight area. A pattern emerges among all the speed factor values in the mandrel forces. However, a noticeable change occurs in the wiper die forces at speed factors of 0.98, 1.00 and 1.04, particularly at 50° for the speed factor of 1.04 [17].

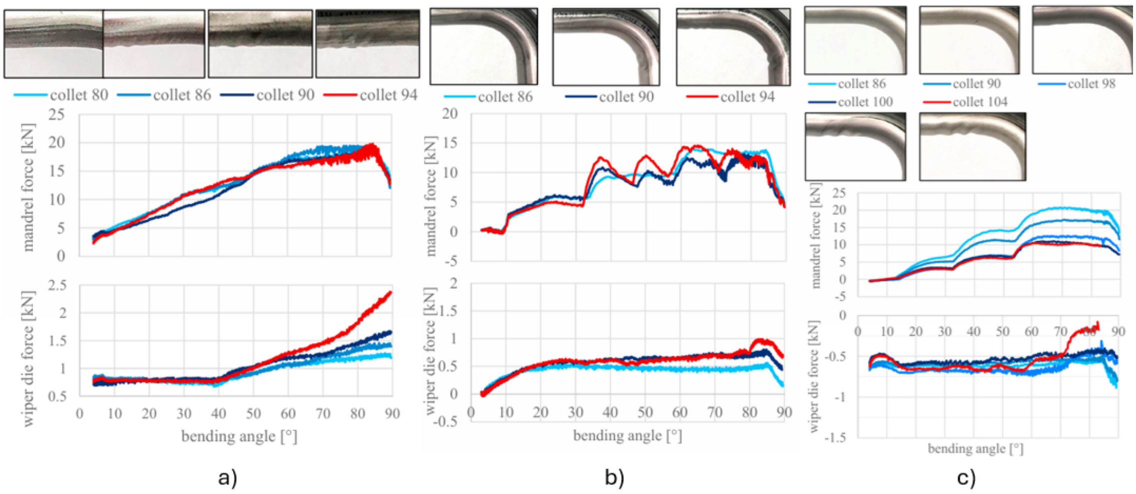

Figure 2.15: Reaction forces for wiper die and mandrel, when varying the speed factor, for different thicknesses: a) t=0.8 mm b) t=1 mm c) t=2 mm [17].

In summary, Borchmann [17] demonstrated that wrinkles forming in the straight section of the tube are detected using a laser line scanner alongside a force sensor mounted on the wiper die. These wrinkles induce alternating transverse forces as a result of bulging behavior. A similar, though less pronounced, effect is observed on the pressure die. Meanwhile, near the clamp die, the force sensor on the mandrel identifies wrinkles as they pass through the mandrel balls during bending, causing fluctuations in the tensile forces.

Another complex phenomenon that has been extensively studied considering the numerous factors that can influence it, is the springback. These investigations offer critical insights into the variables that govern springback behaviour. Murata et al. [19] specifically examine the effect of the hardening exponent on springback behavior through FEM. Their study focuses on a tube with a diameter (D) of 38.1 mm, wall thickness (t) of 1.8 mm, and a CLR of 171.5 mm, using the material properties summarised in Table 2.1. The results are represented in Figure 2.16 and it is possible to conclude that the springback percentage does not exceed 7%, which means that the hardening exponent has little effect in this phenomenon.

Table 2.1: Simulation parameters. [19]

Parameter	**Value**
Yield stress, Y (MPa)	200
Hardening exponent, n	0.1, 0.3, 0.5, 1.0
Hardening coefficient, K (MPa)	180
Young's Modulus, E (GPa)	193
Poisson's ratio, ν	0.32
Tube's initial diameter, D_0 (mm)	38.1
Tube's initial thickness, t_0 (mm)	1.8
Bending stroke, S (mm)	250
Bending factor, R/D_0	4.5

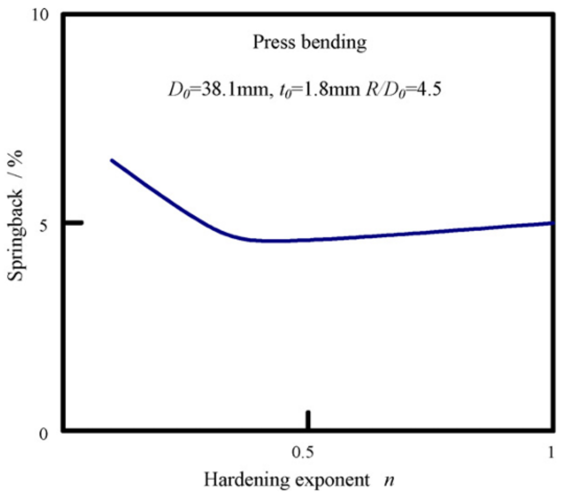

Figure 2.16: Influence of hardening exponent in springback [19].

Finally, Zhan et al. [15] developed an analytical elastic-plastic springback model grounded in static equilibrium conditions, which explicitly incorporates variations in young's modulus (E), wall thickness (t), and the neutral layer position (D_e). This model was validated using Ti-3Al-2.5V tubes subjected to various loading conditions. The results demonstrate that including these material and geometric variations significantly enhances the model's predictive accuracy, reducing the overall error by 67.5%. Among the parameters studied, variations in wall thickness had the most substantial effect, contributing to an error reduction exceeding 40%, whereas changes in young's modulus yielded a comparatively smaller impact, reducing error by over 20% [15]. Figure 2.17 illustrates how springback varies with several key variables. It reveals an approximately linear increase in the springback angle with increasing tube diameter, strength coefficient, and relative bending radius. Conversely, springback decreases as wall thickness, hardening exponent, and poisson's ratio increase, although the latter two factors exert only a minimal influence.

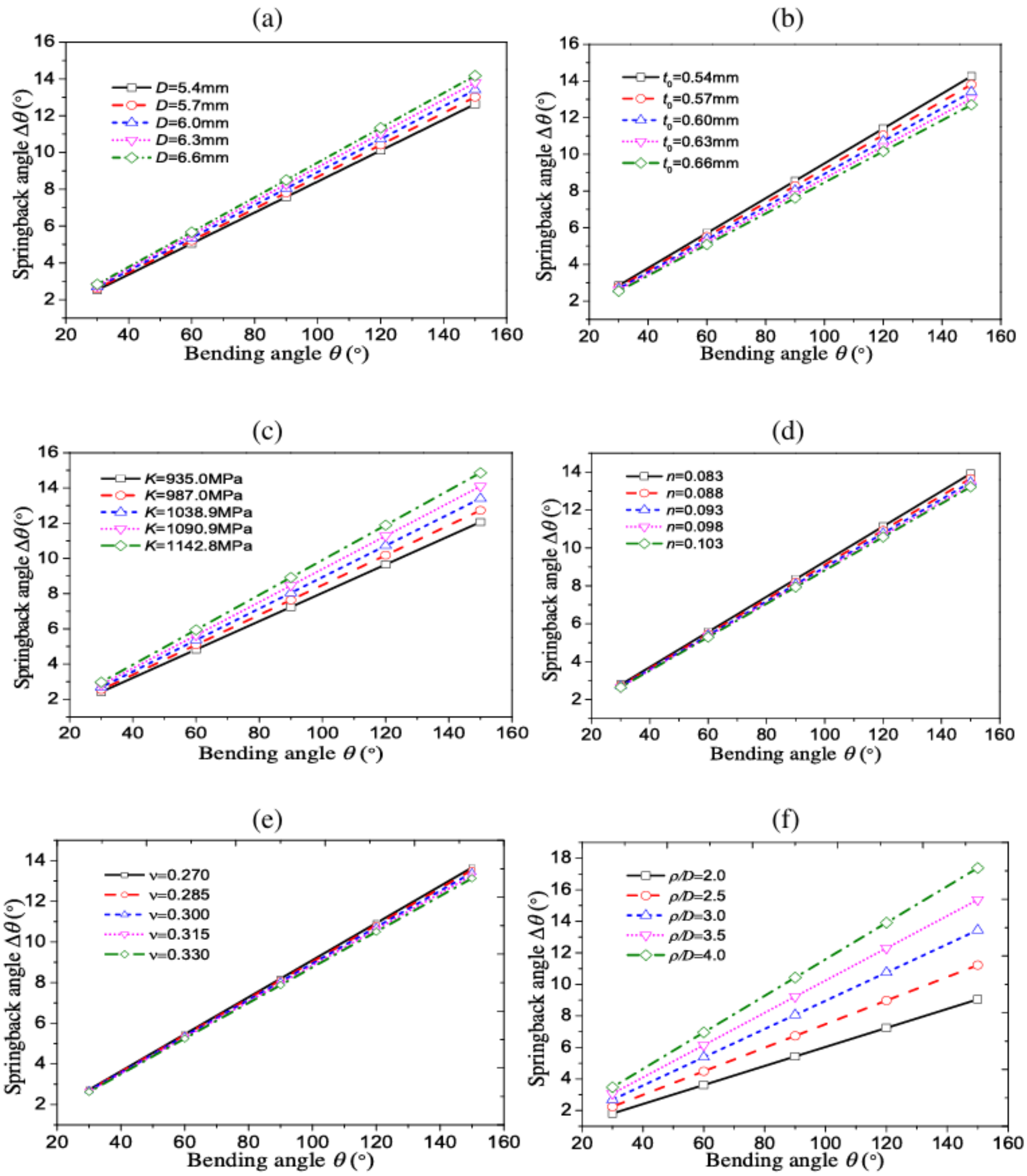

Figure 2.17: Springback variation with a) outer diameter, b) wall thickness, c) strength coefficient, d) hardening exponent, e) poison ratio and f) relative bending radius [15].

An important and complex aspect of springback is its influence on the curvature of the bend. Li et al. [20] conducted a comprehensive investigation into the springback behaviour of high-strength thin-walled tubes (HSTT) subjected to multi-die RDB. Their study combined experimental testing, analytical modelling, and three-dimensional finite element (FE) simulations to provide a detailed understanding of the phenomenon. The materials selected for this study—Ti-3Al-2.5V, 5052-O aluminum alloy, and 1Cr18Ni9Ti stainless steel—were chosen to represent a range of mechanical properties and deformation behaviours. The findings revealed that angular springback arises primarily from elastic recovery occurring in both the bent region and the straight tube ends. In contrast, radius growth is confined to the bent section and does not depend on the bending angle. This distinction is critical for accurately predicting and controlling springback in bending operations.

Controlling springback remains challenging due to the inherent variability in material properties and processing parameters. Variations in material behaviour can significantly amplify springback deviations, especially at higher bending angles, complicating the precision of forming processes. Figure 2.18 illustrates the comparative influence of the different materials on springback under identical bending conditions. Among these, steel shows slightly higher springback than aluminium, a phenomenon attributed to residual elastic strain observed after bending and the subsequent retraction of the tube walls [20]. These insights underscore the necessity of carefully considering material selection and process parameters to effectively manage springback in manufacturing.

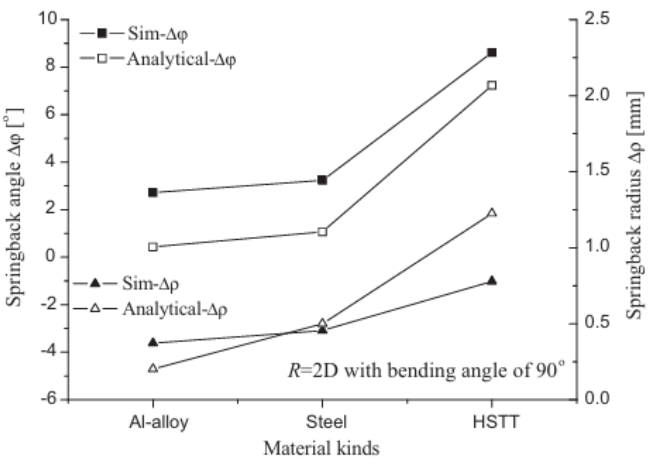

Figure 2.18: Impact of the material in springback [20].

Another interesting analysis performed in the previously mentioned study was the impact of different mechanical properties in the radius springback. Notably, the properties that have the greatest impact are young's modulus (E), the strength coefficient (K), and the normal anisotropic exponent (R), affecting the springback in radius.

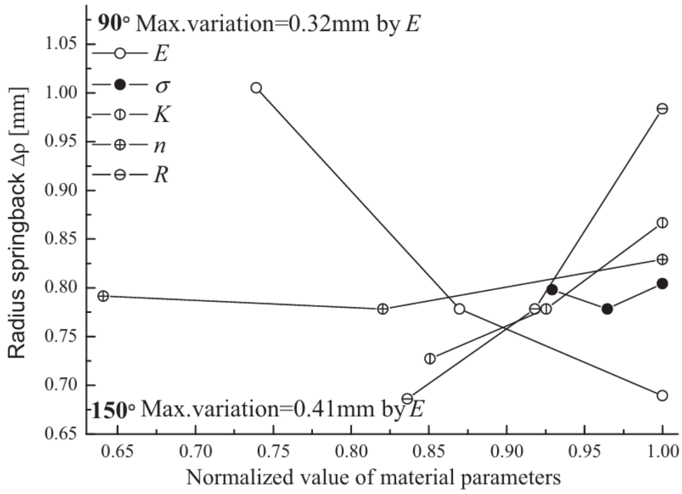

Figure 2.19: Comparison of the springback taking into account the mechanical properties [20].

Additionally, Figure 2.20, the influence of the bending angle on angular springback and radius springback is illustrated. As the bending angle increases, angular springback also increases, while radius springback tends to stabilise.

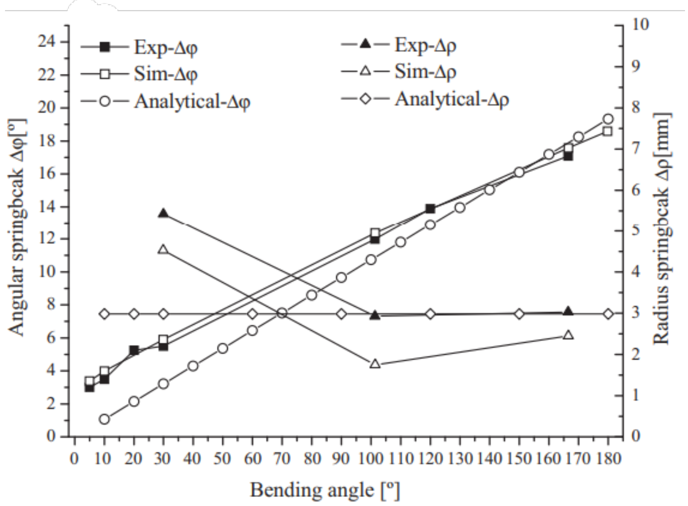

Figure 2.20: Impact of bending angle in the springback [20].

To mitigate inaccuracies caused by springback, a two-level compensation strategy was developed, targeting both angular and radial deviations to improve bending precision. This approach ensures that the deformation remains free from wrinkling and within acceptable limits of wall thinning and cross-sectional distortion by carefully selecting appropriate tooling and processing parameters. The strategy employs either three-dimensional finite element (3D-FE) modelling or a linear fitting method to iteratively adjust the bending radius, thereby compensating for radial springback. By continuously comparing the simulated geometry with the target shape, the bend die radius is refined through successive iterations until the deviation falls within a predefined tolerance range, ensuring accurate and consistent tube bending results. Following the compensation of the bending radius, a similar iterative procedure is applied to correct for angular springback. The designed bending angle is adjusted by incorporating a predicted springback value to obtain a compensated angle, which is subsequently validated through 3D-FE simulation. If the resulting angle deviates beyond the specified tolerance, further iterations are performed by incrementally updating the angle until convergence is achieved. This two-stage compensation process effectively ensures that both the final bending radius and angle closely match the intended design specifications, thereby enhancing dimensional accuracy and forming reliability in tube bending operations [20].

2.3 Final Remarks

The RDB process is distinguished among bending techniques for its exceptional accuracy and versatility across a wide range of industrial applications. However, its complexity stems from the intricate interplay between mechanical forces, material behaviour, and process parameters. Common phenomena such as wrinkling, wall thinning, cross-sectional distortion, cracking, and springback are predominantly influenced by stress distribution, tooling configuration, and the intrinsic properties of the material. Consequently, careful selection of tooling and process parameters—such as pressure die force, mandrel type, and wiper die alignment—is critical for effective defect mitigation.

Extensive research has demonstrated the significant impact of variables including tube diameter, wall thickness, bending angle, and material characteristics on springback and deformation outcomes. Advanced tools like FEM, analytical models, and sensor-based control systems have proven invaluable in predicting and understanding these phenomena, thereby facilitating more precise and repeatable bending processes.

Particularly, material properties, such as young's modulus and strength coefficient, as well as tooling design elements, including mandrel ball count and diameter, exert a decisive influence on process stability. Despite these advances, springback remains a persistent challenge, often requiring iterative compensation strategies to achieve dimensional accuracy. These observations underscore the importance of combining numerical modelling with experimental validation to optimise RDB operations and ensure the dimensional and structural integrity of the final components.

The subsequent chapters will detail the methodology employed in this thesis, followed by a comprehensive analysis of the results and final conclusions.

Chapter 3

Methodological Framework and Procedures

This chapter outlines the methodology adopted to investigate the influence of material properties on the tube bending process, with a particular focus on springback and stretching behaviour. To ensure the accuracy and reliability of the experimental and numerical results, a combined approach involving physical testing and numerical simulation, supported by a systematic design of experiments (DoE), was employed.

Key process parameters were selected as input variables, including tube diameter, centerline radius of the bending tool, tube material and thickness, and bending angle. These parameters were systematically varied to understand their individual and combined effects on the bending response.

Numerical simulations were performed using the FEM, which allowed for a detailed analysis of the mechanical behaviour of the tubes during bending, including stress distribution and deformation patterns. These simulations were essential for predicting critical outcomes, such as springback and material stretching.

To validate the numerical models, experimental tests were conducted under controlled conditions, replicating the same parameter combinations used in the simulations. Comparing the simulated and experimental results provided a basis for evaluating the accuracy of the FEM predictions and refining the models when necessary.

3.1 Materials

To investigate the influence of material properties on springback, five materials with different ultimate tensile-to-yield stress ratios were selected: Fe510, SS304, S235, Ti 99.5, and AL2017A. This ratio is a critical factor in sheet metal bending, strongly affecting the springback response and is strongly correlated with the extent of elastic recovery after deformation, as a higher value typically indicates that the material stores more elastic energy during forming, which is subsequently released upon unloading, resulting in greater springback. To enable a more comprehensive analysis of this phenomenon, the selected materials include intentionally cases with similar ultimate tensile-to-yield ratios but differing yield strengths [21].

Fe510 is an unalloyed structural steel, predominantly available in round and sheet forms. It is widely used in welded constructions due to its versatility and strength. Its primary applications include structural frameworks, bridge components, cranes, platform structures, and wind turbine towers [22].

SS304 is a chrome-nickel stainless steel that is non-hardenable. It exhibits good oxidation resistance up to 850°C; however, it is recommended for use only up to 300°C to avoid intergranular corrosion. SS304 can be easily welded without requiring pre-treatment or post-treatment and possesses good machinability. It is well suited for deep drawing applications due to its excellent elongation properties. Furthermore, its corrosion resistance improves with higher polishing quality. Typical applications include the chemical and food industries, handrails, handles and railings [23].

S235 is an economical construction steel suitable for structural applications, machine parts, hardware, and various support elements. This steel is commonly used in cold-drawn or turned conditions. While it is generally not recommended for heat treatment, carbonitriding or nitriding may be applied under specific circumstances [24].

Ti 99.5 corresponds to Grade 1 commercially pure titanium, noted for its exceptional ductility and formability, the highest among the four standard grades of pure titanium. It offers excellent corrosion resistance in both oxidising and mildly reducing environments, including those containing chlorides. This grade also maintains good toughness at low temperatures and exhibits excellent weldability, machinability, and formability under both hot and cold working conditions. Besides its corrosion resistance, Ti 99.5's formability and weldability are key advantages. Titanium Grade 1 tubes find extensive use in the defence industry [25].

AL2017A is an aluminium alloy enriched with copper, resulting in high mechanical properties and increased yield strength. It is among the most durable and reliable materials utilised in the aerospace industry [26].

The chemical compositions of these materials are summarised in Table 3.1 , Table 3.2 and Table 3.3 presents their mechanical properties (information from supplier), including ultimate tensile strength (UTS), which reflects the maximum stress the material can withstand before fracture, and yield strength (YS), which marks the onset of permanent deformation. The UTS/YS ratio provides insight into the elastic recovery capacity, while the material density (ρ) indicates mass per unit volume. Poisson's ratio (ν) describes the ratio of lateral contraction to axial elongation under stress. Elongation (a) represents the material's ductility, and young's modulus (E) quantifies its stiffness under elastic deformation.

To characterise the plastic deformation behaviour of each material, Swift's law was employed. This empirical law, given by Equation 3.1, defines the stress–strain relationship in the plastic region through three material-specific parameters: the strength coefficient (K), the reference strain (ε_0), and the hardening exponent (n). These parameters are listed in Table 3.4.

$$\sigma = K(\varepsilon_0 + \varepsilon_p)^n \tag{3.1}$$

This model provides the basis for the construction of hardening curves used in the numerical simulations, allowing for the accurate prediction of plastic flow during bending.

Table 3.1: Chemical composition of the ferrous materials.

Element	C	Si	Mn	P	S	Cr	Ni	Cu
SS304	0.07	1	2	0.045	0.03	19.5	10.5	-
Fe510	0.22	0.55	1.60	0.030	0.030	-	0.012	0.55
S235	0.17	-	1.4	0.04	0.04	-	0.009	-

Table 3.2: Chemical composition of the non ferrous materials.

Element	C	Si	Mn	Cr	Ni	O	H	Fe	Ti	Al	Cu	Mg	Zn
Ti 99,5	0.08	-	-	-	0.03	0.18	0.015	0.2	Bal.	-	-	-	-
Al2017A	-	0.8	1	0.1	-	-	-	0.7	0.15	Bal.	4.5	0.8	0.25

Table 3.3: Mechanical properties of the materials.

Material	UTS (MPa)	YS (MPa)	ρ (g/cm^3)	ν	A (%)	E (GPa)	UTS/YS
SS304	505	215	7.85	0.30	0.40	195	2.349
Fe510	510	355	7.85	0.28	0.21	206	1.437
S235	360	235	7.85	0.28	0.22	206	1.532
Ti 99.5	410	180	4.51	0.34	0.25	105	2.278
Al2017A	370	240	2.70	0.28	0.15	70	1.542

Table 3.4: Swift's law parameters for the different studied materials.

Material	n	ε_0	K (MPa)
SS304	0.208	0.0011	886.6
Fe510	0.178	0.0017	749.3
S235	0.121	0.0011	533.9
Ti 99.5	0.215	0.0017	707.0
Al2017A	0.153	0.0034	575.5

Figure 3.1 presents the hardening curves of the five materials studied, plotted up to a strain of 0.2, which corresponds to the typical strain range encountered in tube bending operations. Among these, SS304 exhibits the most pronounced hardening behaviour, characterised by a continuous increase in stress at higher strain levels. This behaviour is consistent with its relatively high hardening exponent, indicating a strong capacity for strain hardening. Conversely, S235 and AL2017A display limited strain hardening, with their stress levels reaching a plateau at relatively low strains, consistent with their lower hardening exponent values. Fe510 and Ti 99.5 demonstrate intermediate hardening behaviour, with a gradual yet sustained increase in stress as strain progresses.

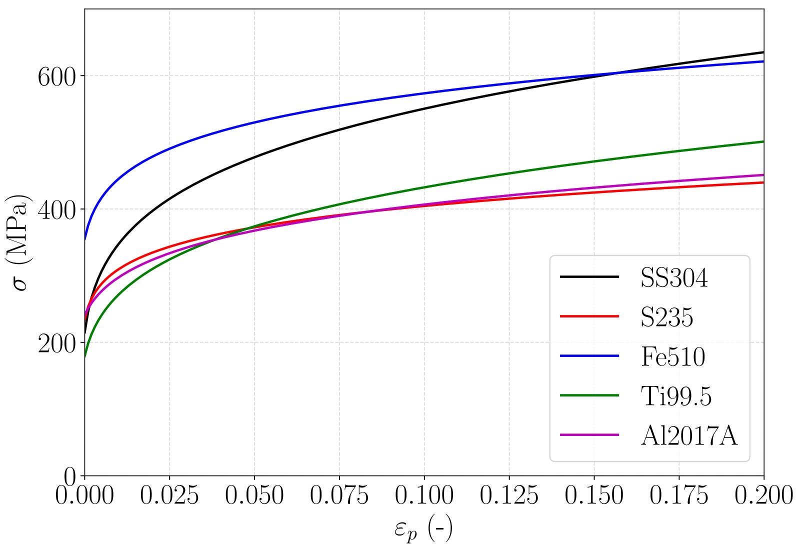

Figure 3.1: Hardening curves for all materials: SS304, S235, Fe510, Ti99.5 and Al2017A.

After reviewing the data presented in the previous tables, it is evident that the five materials differ in both their chemical compositions and mechanical properties, which determine their suitability for various applications. SS304 contains significant amounts of chromium (19.5%) and nickel (10.5%), imparting excellent corrosion resistance. It exhibits a high tensile strength of 505 MPa coupled with a relatively low yield stress of 215 MPa, resulting in a high ultimate tensile-to-yield strength ratio (UTS/YS) of 2.35. This ratio indicates that SS304 can undergo considerable plastic deformation before failure. Fe510 provides a balanced combination of strength and ductility, featuring a higher yield stress (355 MPa) than SS304 and a slightly greater tensile strength (510 MPa). In contrast, S235 presents lower strength (360 MPa tensile strength) but remains a cost-effective choice for less demanding structural applications. Ti 99.5 is characterised by its low density (4.51 g/cm^3) and high elongation (0.215). As a nearly pure titanium grade, it contains minimal amounts of other elements. Al2017A exhibits the lowest density among the materials studied (2.7 g/cm^3) and possesses an excellent strength-to-weight ratio—reflecting its mechanical strength relative to its weight—attributed to alloying elements such as copper (4.5%), magnesium, and manganese. While it does not reach the absolute strength levels of steel, its combination of lightness and strength (370 MPa of tensile strength) makes it highly advantageous for specialised applications.

3.2 Finite Element Model

A FEM was employed to simulate the bending process and predict the behaviour of the bend. Developing a deeper understanding of this process enables more accurate outcome predictions and supports the calibration of the bending machine. The simulations were conducted using ABAQUS, a widely recognised and powerful finite element analysis (FEA) software extensively utilised in both academia and industry for addressing diverse engineering challenges.

The computational scripts used in this study were adapted from a thesis by Santos [27]. Figure 3.2 provides an overview of the workflow and the various scripts implemented. Python scripts are employed to automate the modelling, simulation, and extraction of results within ABAQUS. These scripts are to parameterising the RDB process, thereby ensuring efficiency, accuracy, and repeatability throughout the simulation workflow. Furthermore, they enable rapid adjustments to a range of bending conditions, facilitating flexible and robust analysis.

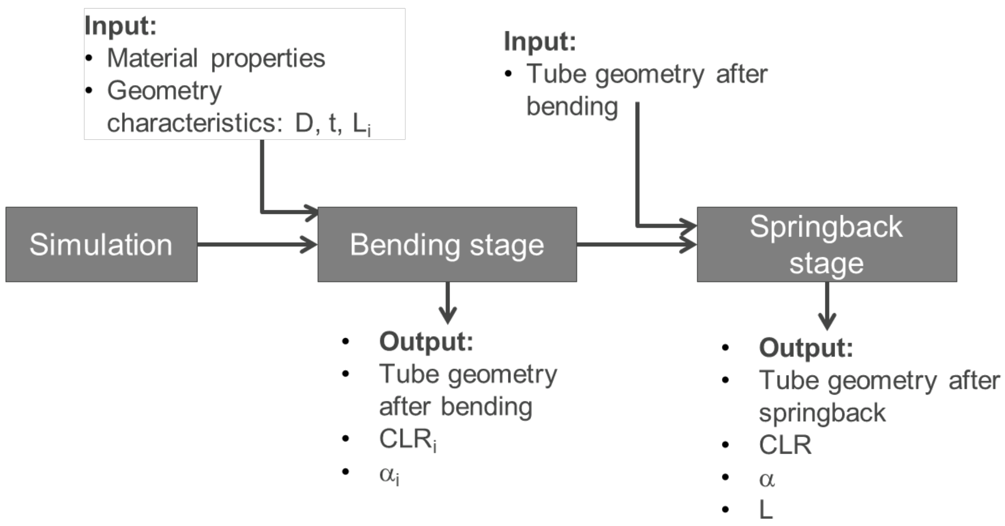

Figure 3.2: Fluxogram of the numerical approach.

Two primary scripts were developed for this study: one dedicated to the bending stage and the other to the springback stage. The first script simulates the tube bending process, while the second model the elastic recovery that occurs after unloading [27].

In the bending stage was simulated using a dynamic explicit finite element model, where the tube was defined as a deformable shell part, and the bending die, pressure die, and tube end were represented as analytical rigid bodies to reduce computational cost. The bend die was characterised by its CLR, the pressure die by its length (L), and the tube by its outer diameter (D) and thickness (t). The tube was discretised using S4R shell elements with reduced integration and five integration points through the thickness. A convergence study determined an optimal mesh nodes around the perimeter and along the length. Node placement was optimised to support accurate calculation of the centerline radius after deformation. Boundary conditions were applied such that the bend die rotated at a prescribed angular velocity of 10 rad/s around the global Oz axis, achieving a maximum bending angle of 200°, while the pressure die translated in coordination with the tube to prevent undesired deformation. Contact interactions were modelled using surface-to-surface definitions: the tube–bend die contact used a friction coefficient of $\mu = 0.1$, while the tube–pressure die contact was defined as frictionless ($\mu = 0$) due to the lack of relative motion. These settings enabled accurate force transmission during bending. A dynamic explicit analysis was conducted to capture the plastic forming behavior. Prior to unloading, critical nodal positions were extracted from the deformed tube to calculate the instantaneous centerline radius, providing essential data for evaluating the tube's bending characteristics. Figure 3.3 illustrate the tooling geometry and mesh configuration used in the simulation alongside their respective mesh configurations. [27].

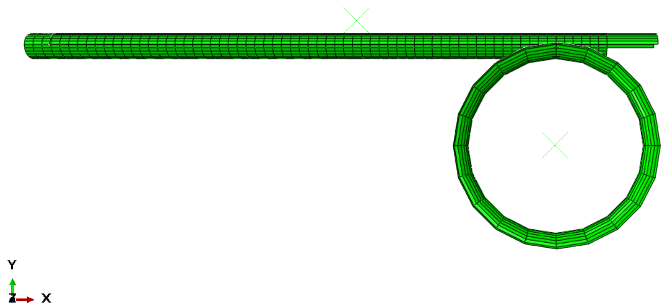

a)

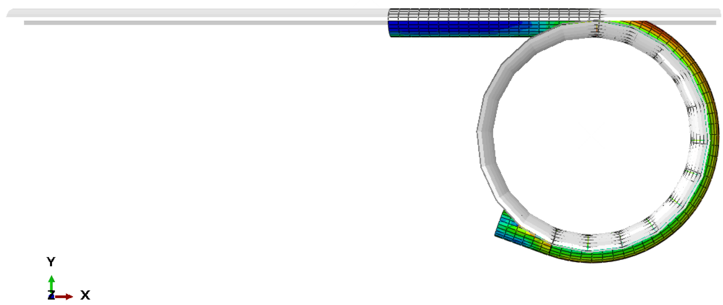

b)

Figure 3.3: Representation of the tools and mesh: a) before and b) after the bending process

The springback stage begins with the deformed geometry obtained from the bending simulation, using the existing stress and strain fields as the initial state. All tooling is removed, and only the tube is considered. A static implicit analysis is conducted to simulate the elastic recovery of the tube, with a single boundary condition applied (fixing one tube end) to prevent rigid body motion while allowing free springback. No contact interactions are included in this stage. The simulation outputs the final tube geometry, from which springback radius (ΔCLR) and springback angle ($\Delta\alpha$) are calculated, as defined in Equations 1 and 2. These metrics are essential for assessing dimensional accuracy after forming. Springback was evaluated at twenty intermediate bending stages between 10° and 200°, providing a detailed understanding of recovery behaviour. For each stage, the tube geometry before and after springback is compared, and the von Mises equivalent stress distribution is visualised on the outer surface. The simulation scripts include automated post-processing routines to extract key numerical results such as springback metrics, stress fields, and final geometry. The parameterised structure of the scripts allows for rapid modification of variables like tube diameter, thickness, bending die radius, and bending angle, facilitating efficient execution of parametric studies [27].

Minor modifications were made to the original scripts to enhance usability and improve the simulation process. For example, the tube model was divided into four equal partitions to optimise node management. Additionally, a feature was implemented to measure the length of the bend both before and after springback. This was achieved by developing a script that extracts node coordinates from both the bending and springback simulations. These coordinates are then processed to accurately calculate the bend length and the CLR.

For the calculation of the CLR before and after springback, the center of the circle was first determined, followed by the calculation of the radius for each node coordinate using equations 3.2 and 3.3. The average of these radii was then computed. The center point (X_{center} and Y_{center}) was calculated separately for the coordinates before and after springback along with the coordinates of which point (x_{ini} and y_{ini}).

$$CLR_i = \sqrt{(x_{ini} - X_{\text{center}})^2 + (y_{ini} - Y_{\text{center}})^2} \tag{3.2}$$

$$CLR = \sqrt{(x_{fin} - X_{\text{center}})^2 + (y_{fin} - Y_{\text{center}})^2} \tag{3.3}$$

Beside that, the bending angle before and after was also calculated using the Equations 3.4 and 3.5. For that a node at the end of the tube was strategically chosen for the calculation, using its coordinates before and after the unloading.

$$\alpha_i = (\text{atan2}(1,0) - \text{atan2}(y_{ini}, x_{ini})) * \frac{180}{\pi} \tag{3.4}$$

$$\alpha = (\text{atan2}(1,0) - \text{atan2}(y_{fin}, x_{fin})) * \frac{180}{\pi} \tag{3.5}$$

At last, the length of the tube was calculated using the coordinates and the sum of distances between the consecutive nodes align with the CLR line, as the example of Figure **??**a). The Equation 3.6 was used for calculate the length of the tube using the coordinates before SB and after SB.

$$L = \sum \sqrt{(x_i - x)^2 + (y_i - y)^2} \tag{3.6}$$

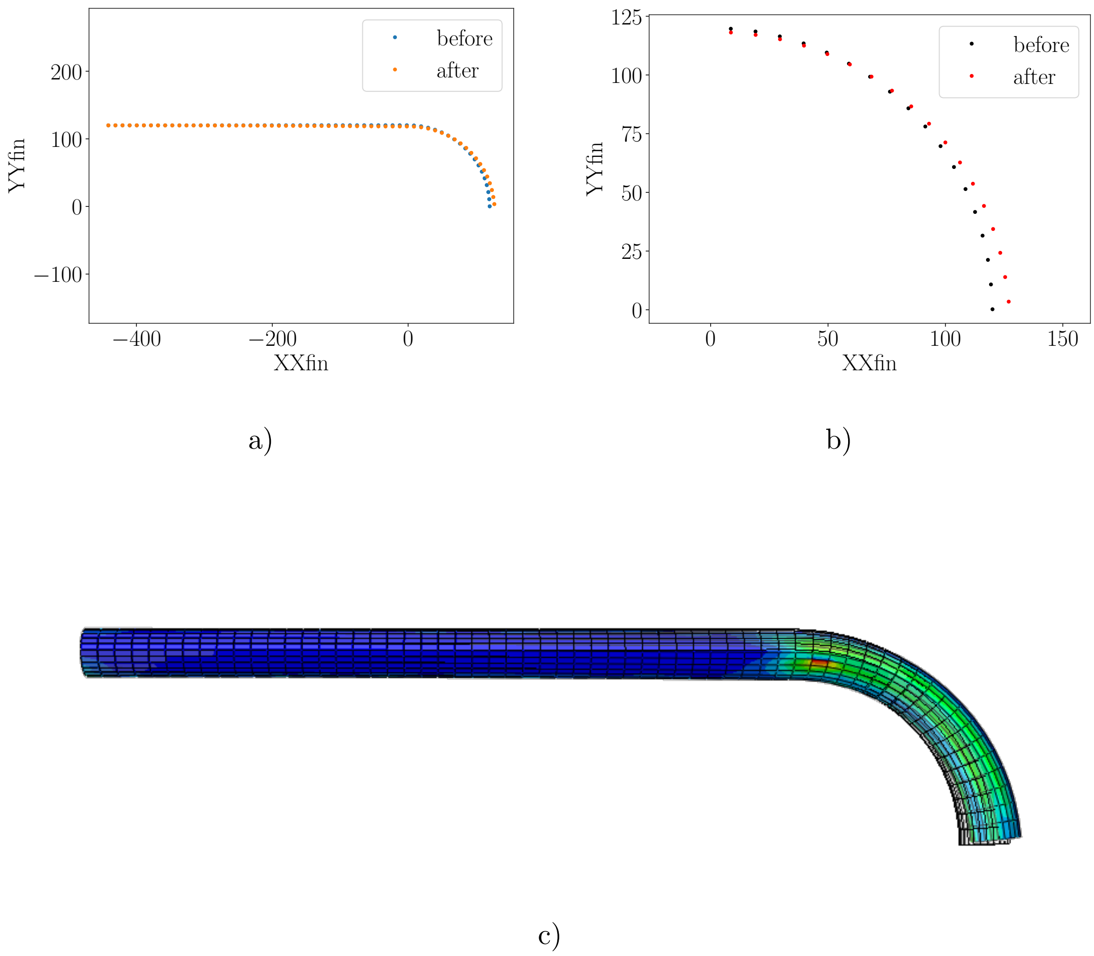

Figure 3.4: Example of representation of a) all the nodes, b) the nodes used for calculations, c) numerical simulation representing the springback for a bending angle of 90° with a CLR of 120 mm (CLR120).

After having these values, the analysis consisted of calculating the ΔCLR, $\Delta\alpha$, ΔL and comparison, as will be shown later by graphics. These results will be shown in Section 4.1.2

3.3 Design of Experiments

The Design of Experiments (DoE) was developed considering a tube with a fixed diameter of 30 mm, while varying the material, thickness, bending angle and CLR. Since these variables could generate an infinite number of combinations, the study focused on five selected materials, three thicknesses, and two CLR values. The bending angle was varied from 0° to 200° in increments of 10°. Figure 3.5 illustrates the DoE configuration employed in this study.

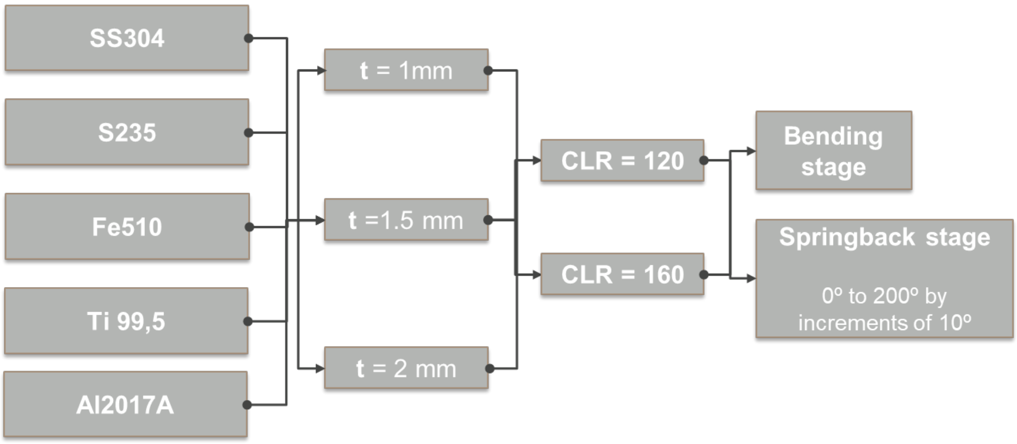

Figure 3.5: DoE for numerical analysis.

3.4 Experimental Approach

In the experimental analysis, tests were performed using two CLR of 120 and 160 mm, two materials(SS304 and S235). For each material, two thicknesses were considered (1.5 and 2.0 mm). Bending operations were carried out at five different angles: 45°, 70°, 90°, 150°, and 180°.

The experimental tests were conducted in an eMOB 52 (Figure 3.6a) placed in a workshop at FEUP. In Figure 3.6b it is presented a different view of the machine, for better understanding of the dimensions.

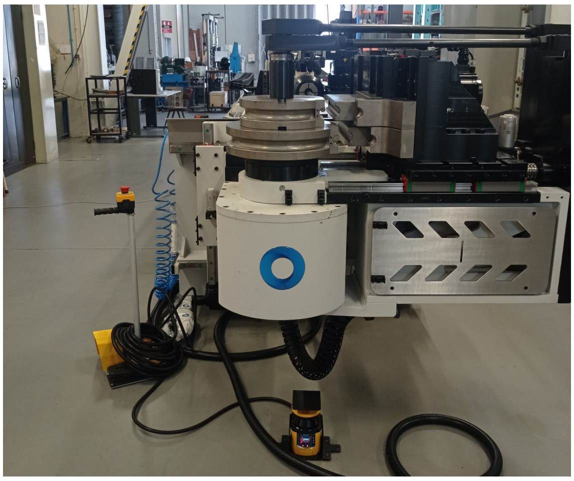

(a)

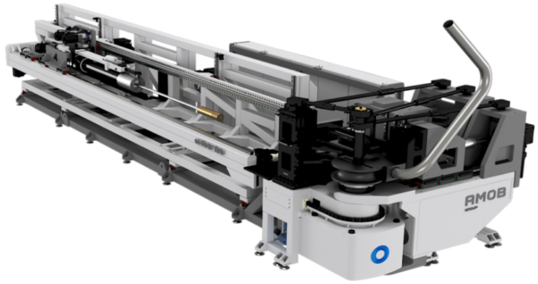

(b)

Figure 3.6: Different representations of the machine used: a) eMOB 52 at FEUP workshop and b) perspective view of eMOB 52 [28].

AMOB provides a very interactive and user-friendly software for operators allowing an easy and light experience. Figure 3.7 shows the machine's software that controls all ten axes. The axes are identified by letters starting by:

- **X** : longitudinal movement corresponding to the tube feeding;
- **Y** : rotation around the tree axis controlling the bending angle;
- **Z** : rotation around the tube axis allowing to change the bending plane;
- **T** : opening and closing movement of the clamp;
- **E** : movement of the pressure die along the tube axis;
- **H** : vertical movement of the tree;
- **W** : horizontal movement of the tree;
- **M** : movement of the mandrel;
- **C** : movement of the pressure die against the tube;
- **P** : movement of the clamp die.

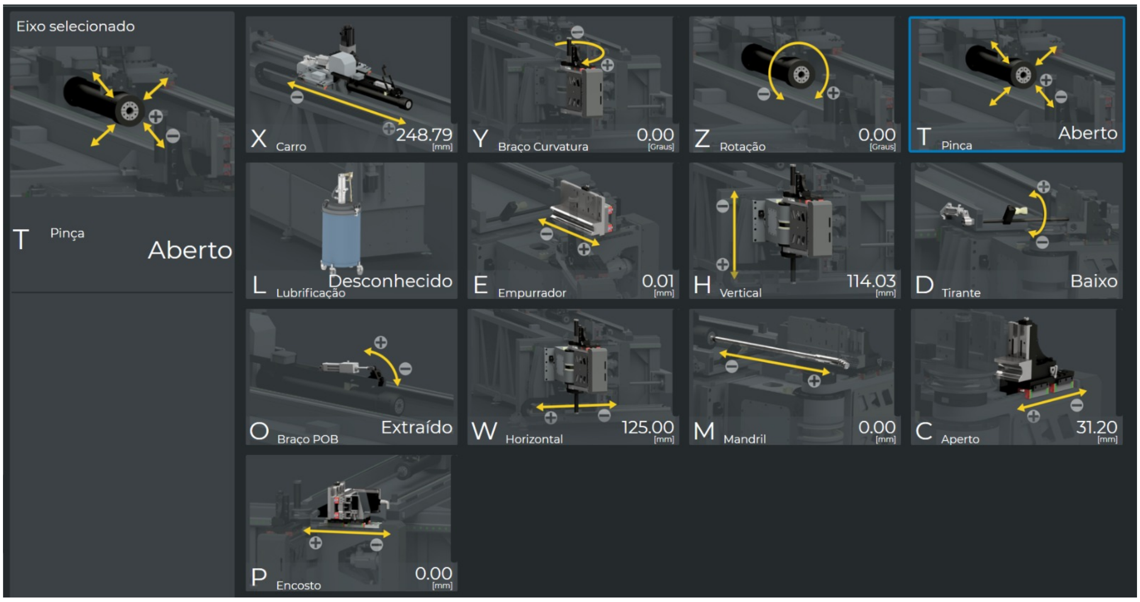

Figure 3.7: Representation of the axis in the AMOB's software.

It was followed the DoE presented in previous chapters, but only for thicknesses 1.5 and 2 mm, two materials (SS304 and S235) and regarding five bending angles: 45°, 70°, 90°, 150°, 180°.

All material was catalogued for easier organisation as seen in Figures 3.8a and 3.8b. Then the programs were developed and implemented for each combination. It was very important to keep all the tests consistent, for that it was maintained the same velocity in the machine and the welding of the tubes was always keep upwards.

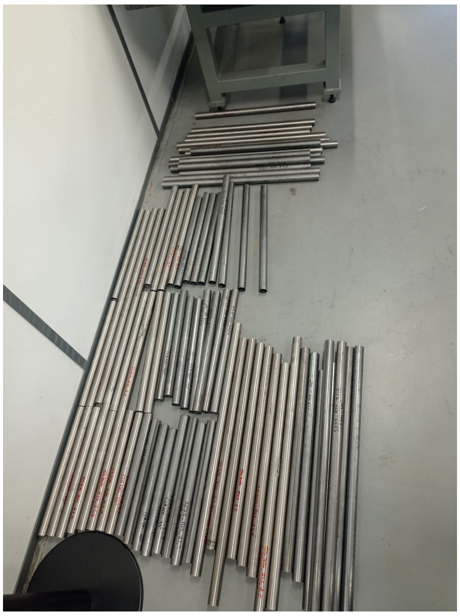

(a)

(b)

Figure 3.8: Organisation and cataloguing of the tubes, regarding the material, thickness and the corresponding CLR and bending angle.

In Figure 3.9, it is possible to see the five angles that will be done in the experiments. The results are shown in Section 4.2.

Figure 3.9: Tube with the five angle that will be analysed. In order: 45°, 70°, 90°, 150°, 180° (Example of the figure: SS304 thickness=1.5 mm CLR120)

3.4.1 3D Digitalization with Hexagon

A 3D digitalisation of every bend was done in Amob facilities with Hexagon machine equipped with Bending Studio XT. In Figure 3.10a, it is possible to see the equipment, and in Figure 3.10b the software used.

(a) (b)

Figure 3.10: a) Hexagone machine installed in AMOB; b) Bending Studio XT software.

BendingStudio XT is a comprehensive software solution that integrates every stage of the tube and wire manufacturing process, encompassing design, production, and quality control. By consolidating all relevant data sets associated with a part, the software enables manufacturers to monitor, quantify, and visualise changes throughout each phase. Through the integration of CAD data, bending corrections, and inspection plans within a unified platform, BendingStudio XT streamlines workflows, thereby enhancing accuracy and efficiency across the entire production cycle [29].

Specifically developed to support systems such as TubeInspect, Absolute Arm, and Absolute Tracker—other advanced measurement devices by Hexagon BendingStudio XT combines high-speed performance with adaptability for both manual and automated inspection processes. Its user-friendly interface facilitates efficient data management, simplifying the documentation and control of every manufacturing stage. Whether handling small components or large-scale tubes, the software ensures precise measurement and correction capabilities, thereby supporting reliable production across a diverse range of applications and geometries [29].

Regarding the process of digitalisation, there are some important aspects such as:

- position the tube with the part that has been attached to the clamp pointing towards the right side of the arm, which is a pre-definition of the machine;
- make sure to digitilise the point that touches the table, because this means that more than half of the tube is digitilised;
- make sure that every part of the tube has been scanned, since the software makes fictitious short cylinders to design the tube. If the tube is not digitilised in its majoraty, it means that what the software represents may not be reality.

After digitisation, BendingStudio XT produces a detailed report containing essential information for analysis, which can be selected based on convenience. This report presents the best-fit alignment between the reference tube and the measured tube. It provides several critical dimensional parameters, including the straight-line distance between the tube's two ends, known as the End-to-End Distance, and the rolled-out length, which corresponds to the total length of the bent tube. This measurement is particularly important for evaluating stretching and bending effects, which are fundamental to springback analysis. Additionally, the report details the lengths of the straight sections, rotation angle, bending angle, and CLR. An example of such report is provided in Section A, while Figure 3.11 highlights a key section from the report. It is also important to clarify that the term "Nominal" refers to the reference CAD tube (optimal geometry), whereas "Actual" denotes the tube as measured after bending.

End length results - BentPartComp

Component	Property	Value [mm]		
		Actual	Nominal	Act-Nom
BentPartComp	End-to-end distance	816.37	783.51	32.85
BentPartComp	Rolled-out length	1,505.33	1,500.00	5.33

Bending elements - BentPartComp

No.	Length [mm]			Rotation [deg]			Angle [deg]			Radius [mm]		
	Actual	Nominal	Act-Nom	Actual	Nominal	Act-Nom	Actual	Nominal	Act-Nom	Actual	Nominal	Act-Nom
BE1	171.79	170.00	1.79	-	-	-	40.60	45.00	-4.40	174.30	160.00	14.30
BE2	199.47	200.00	-0.53	-89.63	-90.00	0.37	135.77	145.00	-9.23	126.91	120.00	6.91
BE3	171.92	170.00	1.92	-89.74	-90.00	0.26	82.89	90.00	-7.11	128.99	120.00	8.99
BE4	351.30	342.15	9.15	-	-	-	-	-	-	-	-	-

Figure 3.11: Excerpt from the generated report with parameters of the tube.

3.4.2 3D Digitalisation with ATOS Triple Scanner

A different approach for scanning the tubes after bending was considered to guarantee the reliability and accuracy of the previous method using Hexagon machine. This method relies on the comparison between the expected geometry of the tube after bending and the actual geometry due to springback. For this analysis, the ATOS triple scanner was used.

ATOS is a high-resolution, optical 3D scanning system widely used in industrial metrology. It delivers rapid and precise three-dimensional measurement data, supporting the optimisation of engineering processes and enhancing manufacturing efficiency. The system is extensively applied across various industries for the inspection and analysis of components such as sheet metal parts, tooling, turbine blades, prototypes, as well as injection-molded and cast parts. ATOS captures complete part geometries in the form of dense point clouds or polygon meshes, providing accurate surface and geometric data essential for comprehensive analysis and quality assurance [30]. In Figure 3.12 it is represented the equipment and the setup of the tube with the targets.

(a) (b)

Figure 3.12: Scanner setup: a) ATOS triple scanner b) tube for scanning.

Chapter 4

Results

This chapter presents the results of all simulations and experimental tests, accompanied by detailed explanations and justifications of key findings. The analysis focuses on comparisons between different materials, as well as the influence of the thickness, centerline radius and bending angle used. Particular attention is given to how these factors affect springback and overall deformation behaviour.

4.1 Numerical Analysis of RDB Process

The numerical results obtained through the methodology described in Section 3.2 are presented in this section, with particular emphasis on the mesh convergence study, the process simulation data for the materials selected (SS304, S235, Fe510, Al2017A, Ti99.5) and thicknesses (1 mm, 1.5 mm and 2 mm), as well as the data for a real case scenario.

4.1.1 Mesh Convergence

Before proceeding with the full numerical analysis, a mesh convergence study was conducted to ensure the reliability and accuracy of the simulation results. This analysis was performed using Fe510 material and 200° bending angle, chosen due to its high UTS. The mesh in the finite element model (FEM) is defined by two key parameters:

- The number of elements along the tube's perimeter (cross-section);
- The number of elements along the tube's length.

The goal of the mesh convergence study is to verify that critical simulation outputs, such as the springback radius, remain stable as the mesh is refined. The optimal mesh is defined as the coarsest configuration that delivers converged results, balancing accuracy and computational efficiency.

In the mesh convergence analysis, the number of elements across the tube's cross-section was initially fixed at 24, while the number of elements along the tube length was varied. Two CLR values (120 and 160 mm) were analysed to determine whether geometry had a significant influence on mesh sensitivity. For each mesh configuration, the post-springback CLR value was extracted and is presented in Table 4.1.

As shown in the table, increasing the number of elements along the tube from 15 to 120, results in only a marginal variation in the springback radius—about 0.02% for CLR120 and 1.4% for CLR160. However, this increase leads to a substantial rise in computational time, from under 2 minutes to over 14 minutes. These trends are also illustrated in Figure 4.1, which plots the CLR after springback (ASB) for both CLR values as a function of the number of longitudinal elements. The curves clearly show that after 60 elements, the change in CLR becomes negligible, indicating mesh convergence. Based on this analysis, the configuration with 24 elements in the cross-section and 60 along the tube's length was selected as optimal.

Table 4.1: Influence of mesh density on CLR after springback and computational time for Fe510 with a 200° bend.

	Number of nodes		CLR (mm)	Computational
	Cross section	Along tube		time (min:s)
CLR120_24_15	24	15	119.351	1:43
CLR120_24_30	24	30	121.067	2:54
CLR120_24_60	24	60	121.81	5:28
CLR120_24_120	24	120	121.847	14:36
CLR160_24_15	24	15	159.214	1:54
CLR160_24_30	24	30	160.735	2:53
CLR160_24_60	24	60	162.095	5:20
CLR160_24_120	24	120	161.417	15:20

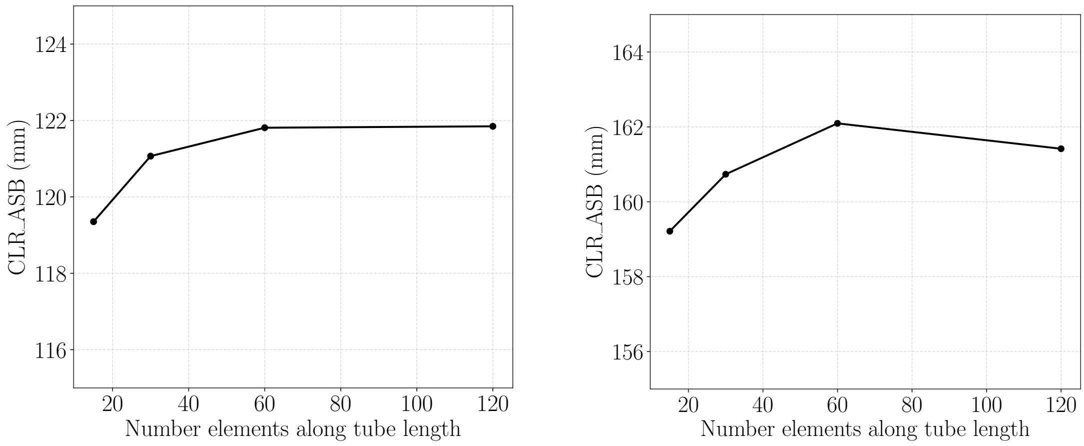

(a) (b)

Figure 4.1: Data of CLR after springback (ASB) from : a) CLR120 and b) CLR160 when there are 24 elements in cross section and the elements along the tube are varied.

Figure 4.2 presents the von Mises stress distribution for each mesh configuration described in Table 4.1. The subfigures (a) through (h) display the stress response under the same bending conditions (e.g. velocity), varying only the CLR, allowing a direct comparison of mesh sensitivity. As the mesh becomes progressively finer, a slight increase in the maximum von Mises stress values is observed. Moreover, the refinement leads to a more continuous and evenly distributed stress field, particularly in regions with high curvature and stress concentration. This enhanced uniformity in the stress contours reflects improved numerical stability and resolution. These observations support the conclusion that mesh refinement contributes significantly to simulation accuracy, especially in complex deformation scenarios such as tube bending with springback.

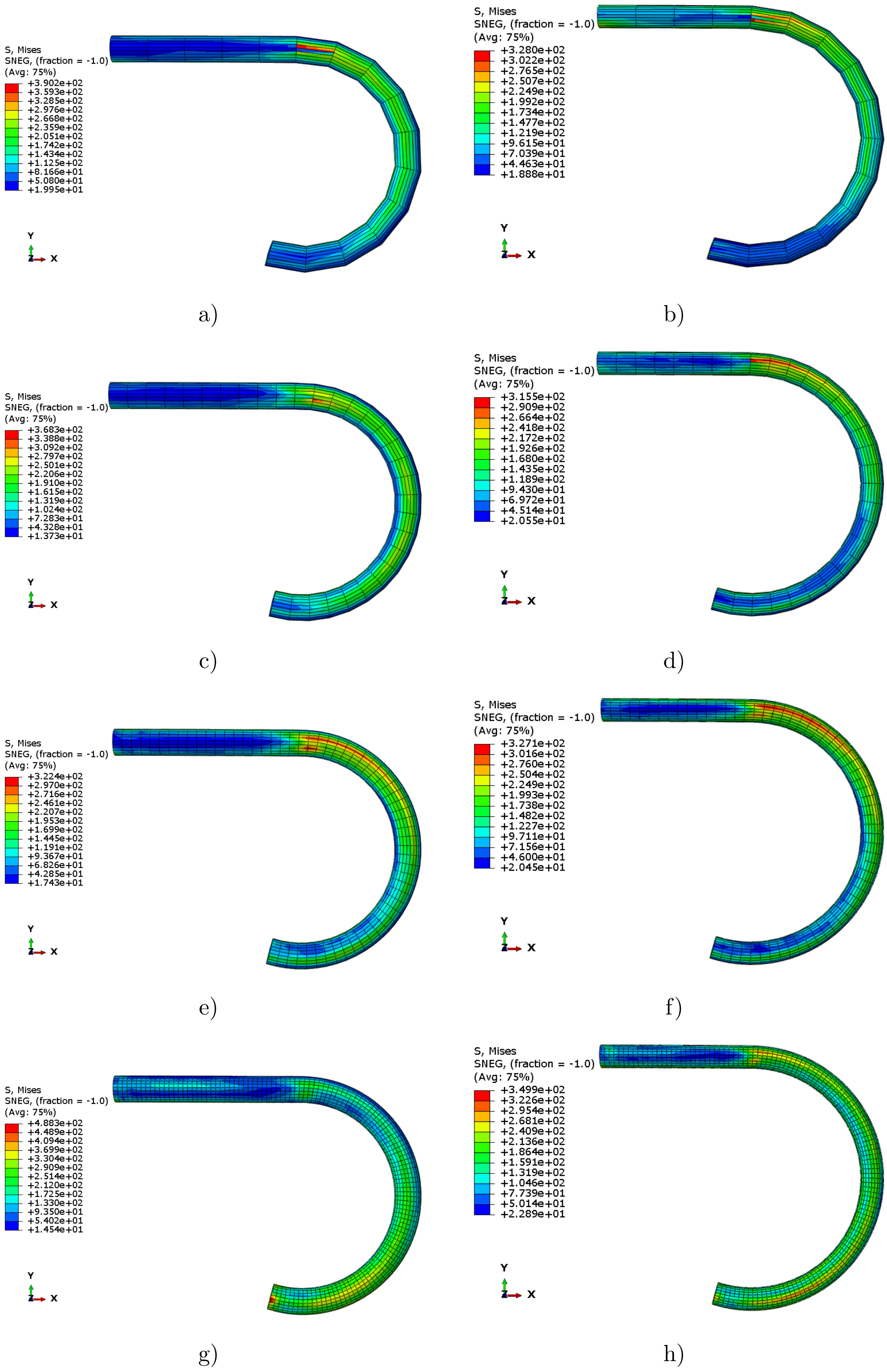

Figure 4.2: von Mises stress distribution for different elements along the length for CLR120 in left side: a) 15, c) 30, e) 60, g) 120 and for CLR160 in right side b) 15, d) 30, f) 60, h) 120.

Following the selection of the optimal number of elements along the tube's length, a second mesh convergence analysis was performed to evaluate the influence of cross-sectional discretisation. This step is critical to ensure that the numerical model accurately captures stress gradients and deformation behaviour across the tube perimeter.

In this analysis, the number of elements along the tube length was fixed at 60, as defined previously, and the number of elements around the cross section was varied: 12, 24, and 48. The results are summarised in Table 4.2, which presents the CLR values after springback and the corresponding computational times for two CLR values (120 mm and 160 mm). However, the reduction in CLR between 24 and 48 elements is minimal — only about 1.1% for CLR120 and 0.9% for CLR160 — while the computational time increases more than fourfold, from approximately 5 minutes to over 22 minutes.

Based on the trade-off between accuracy and efficiency, the mesh configuration with 24 elements in the cross section and 60 along the tube length was confirmed as optimal. This setting captures the essential mechanical behaviour of the bending process while maintaining a reasonable simulation time.

Figure 4.4 illustrates the von Mises stress distribution for tubes modelled with different mesh configurations, as outlined in Table 4.2. The images on the left — (a), (c), and (e) — correspond to the CLR120 configuration, while those on the right — (b), (d), and (f) — represent CLR160. In both cases, the mesh is progressively refined from top to bottom by increasing the number of elements in the tube's cross-sectional perimeter.

This improvement is particularly evident in the CLR160 configurations (right column), where the stress concentration zones are captured with greater clarity and resolution in the finer meshes. These results reinforce the conclusion that refining the cross-sectional mesh enhances the numerical model's ability to accurately represent stress fields in complex deformation regions.

Table 4.2: Data for elements along the tube length after choosing the number of elements in cross section.

	Number of nodes		CLR (mm)	Computational time (min:s)
	Cross section	Along tube		
CLR120_12_60	12	60	122.548	1:54
CLR120_24_60	24	60	121.81	5:28
CLR120_48_60	48	60	120.44	22:19
CLR160_12_60	12	60	163.325	1:42
CLR160_24_60	24	60	162.095	5:20
CLR160_48_60	48	60	160.591	23:12

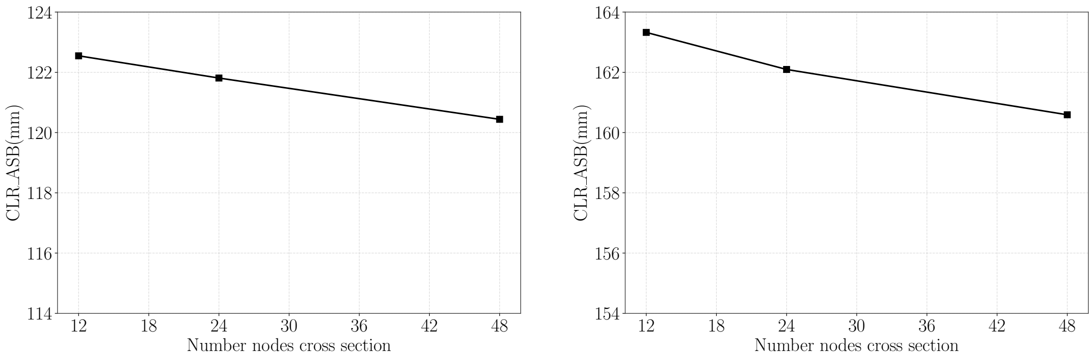

(a) (b)

Figure 4.3: Data of CLR after springback (ASB) from : a) CLR120 and b) CLR160 when there are 60 elements along the rube and the elements along the cross section are varied.

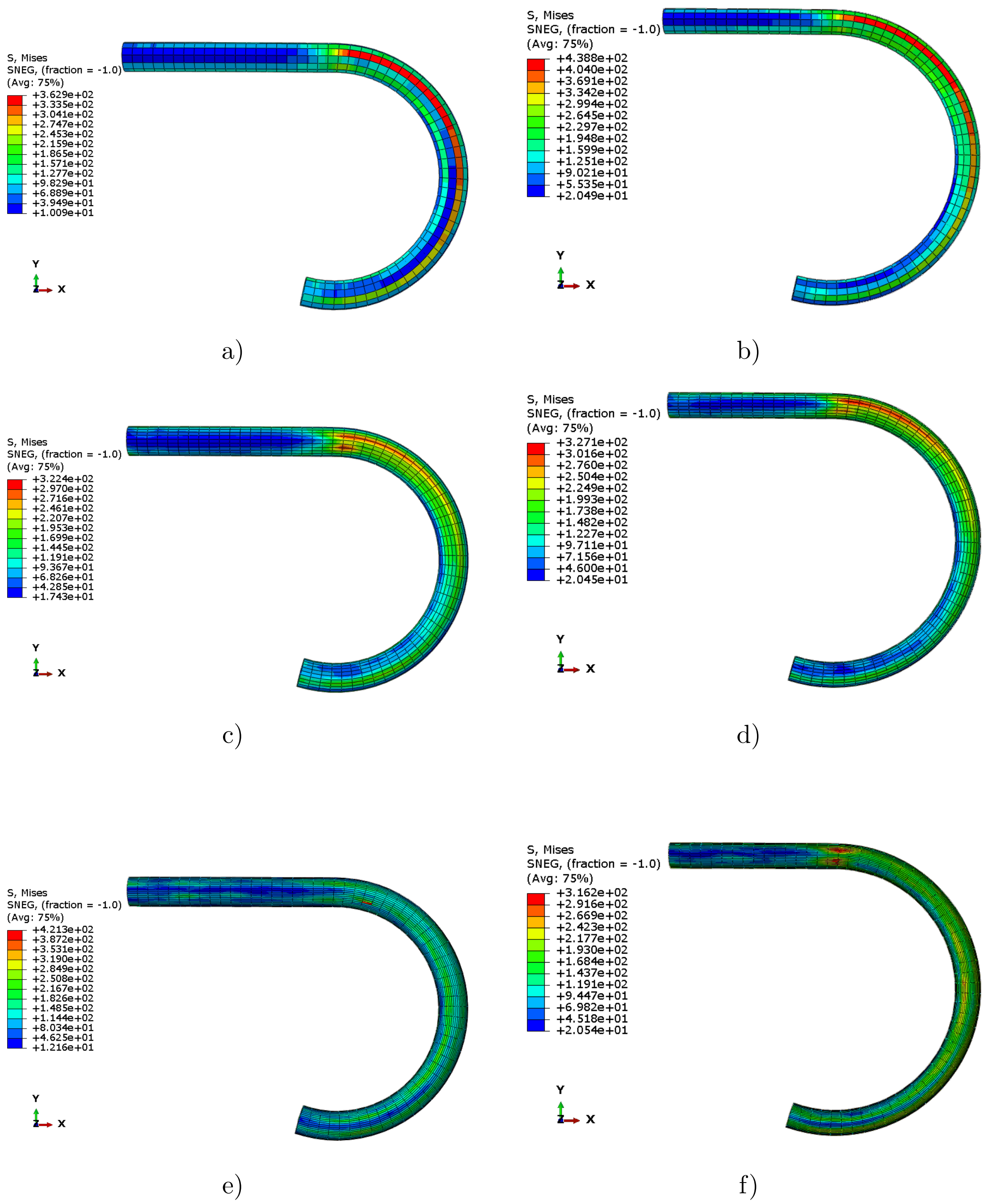

Figure 4.4: von Mises stress distribution for different elements in cross section for CLR120 in left side: a) 12, c) 24, e) 48 and for CLR160 in the right side b) 12, d) 24, f) 48.

Finally, the influence of the number of integration points through the shell thickness was analysed. Integration points are specific locations within each element where key quantities—such as stress and strain—are evaluated. These points play a crucial role in capturing through-thickness gradients, which are especially relevant in bending-dominated problems involving elastic recovery, such as springback.

As shown in Table 4.3 and Figures 4.5a and 4.5b, increasing the number of integration points from 5 to 11 resulted in negligible variation in the predicted centerline radius (CLR) after springback—less than 0.02% for both CLR120 and CLR160. However, this refinement led to a significant increase in computational time, nearly doubling between the two configurations.

Based on these results, the use of 5 integration points through the shell thickness was deemed sufficient to ensure numerical accuracy while maintaining computational efficiency. All the results presented throughout this chapter were obtained using this configuration.

Table 4.3: Data for integration points after having the best mesh.

	Integration points	CLR (mm)	Computational time (min:s)
CLR120_5	5	121.81	5:28
CLR120_9	9	121.816	9:25
CLR120_11	11	121.831	9:19
CLR160_5	5	162.095	5:20
CLR160_9	9	162.148	9:45
CLR160_11	11	162.136	9:58

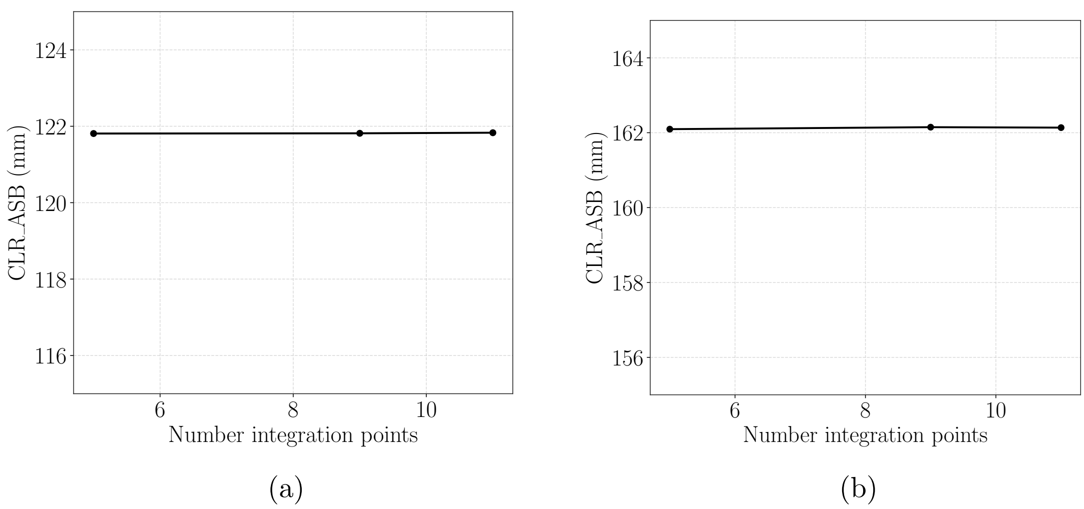

Figure 4.5: Data of CLR after springback (ASB) for : a) CLR120 and b) CLR160 when the integration points are varied.

Based on the balance between numerical accuracy and computational efficiency, the final mesh configuration selected for all subsequent simulations consisted of 24 elements along the tube's cross-sectional perimeter, 60 elements along its length, and 5 integration points through the shell thickness.

4.1.2 Influence of Material and Tool Geometry

Following the methodology described in Section 3.2, numerical simulations were performed for each material, centerline radius and wall thickness combination. The results are presented in terms of the three key variables under investigation: springback in radius (ΔCLR), springback in angle ($\Delta\alpha$), and tube elongation (ΔL). Figures 4.7 through 4.11 display the results for each material. For each material, results obtained with a CLR of 120 mm are shown on the left, while those with a CLR of 160 mm are presented on the right. Subfigures (a) and (b) show the springback in angle ($\Delta\alpha$), (c) and (d) show the springback in radius (ΔCLR), and (e) and (f) present the tube elongation (ΔL). Figure 4.6 shows the results for SS304, Figure 4.7 for S235, Figure 4.8 for Fe510, Figure 4.9 for Al2017A, and Figure 4.10 for Ti99.5.

For this study, the bending angle was varied from 30° to 180°, allowing for a comprehensive assessment across a wide range of typical forming scenarios. The analysis is structured into three main parts: the influence of tube thickness, the influence of different centerline radii, and the comparison between materials.

Regarding wall thickness, the results suggest that its influence, while not dominant, is consistent across all materials. In general, tubes with greater wall thickness tend to exhibit increased springback and reduced elongation.

This trend is clearly illustrated in the case of SS304. When comparing tubes with wall thicknesses of 1 mm and 2 mm for a CLR of 160 mm, as shown in Figure 4.6, the thinner tube exhibits a more extensive plastified region, indicated by the grey area. This greater degree of plastic deformation implies that the 1 mm tube undergoes less elastic recovery, resulting in reduced springback. This behaviour is confirmed by the simulation results presented in Figure 4.7. Furthermore, it can be observed that the influence of thickness becomes more pronounced as the bending angle increases, and this effect is particularly evident in the springback behaviour of the radius (ΔCLR).

This relationship between thickness, plastic deformation, and elastic recovery is consistent across the other materials analyzed. Although the quantitative effects vary depending on each material's mechanical properties, the overall behaviour remains qualitatively similar. Therefore, while wall thickness may not be the primary driver of springback, it remains an important consideration in precision forming processes.

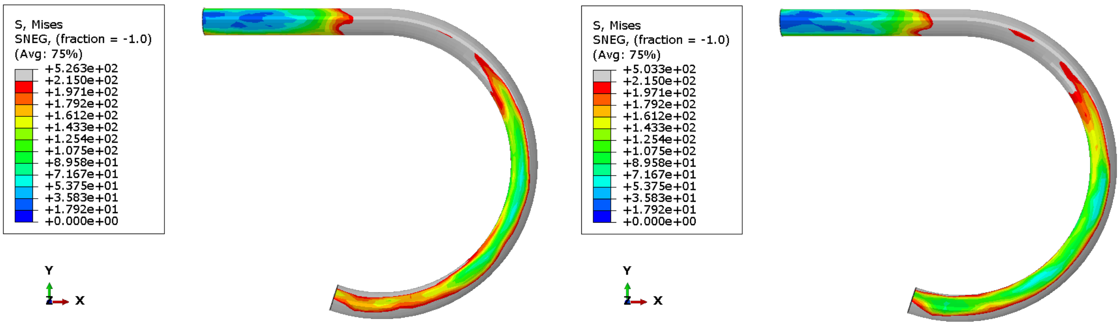

(a) (b)

Figure 4.6: Comparison of plastic area between a) 1 mm and b) 2 mm thicknesses for SS304 when CLR160, after springback.

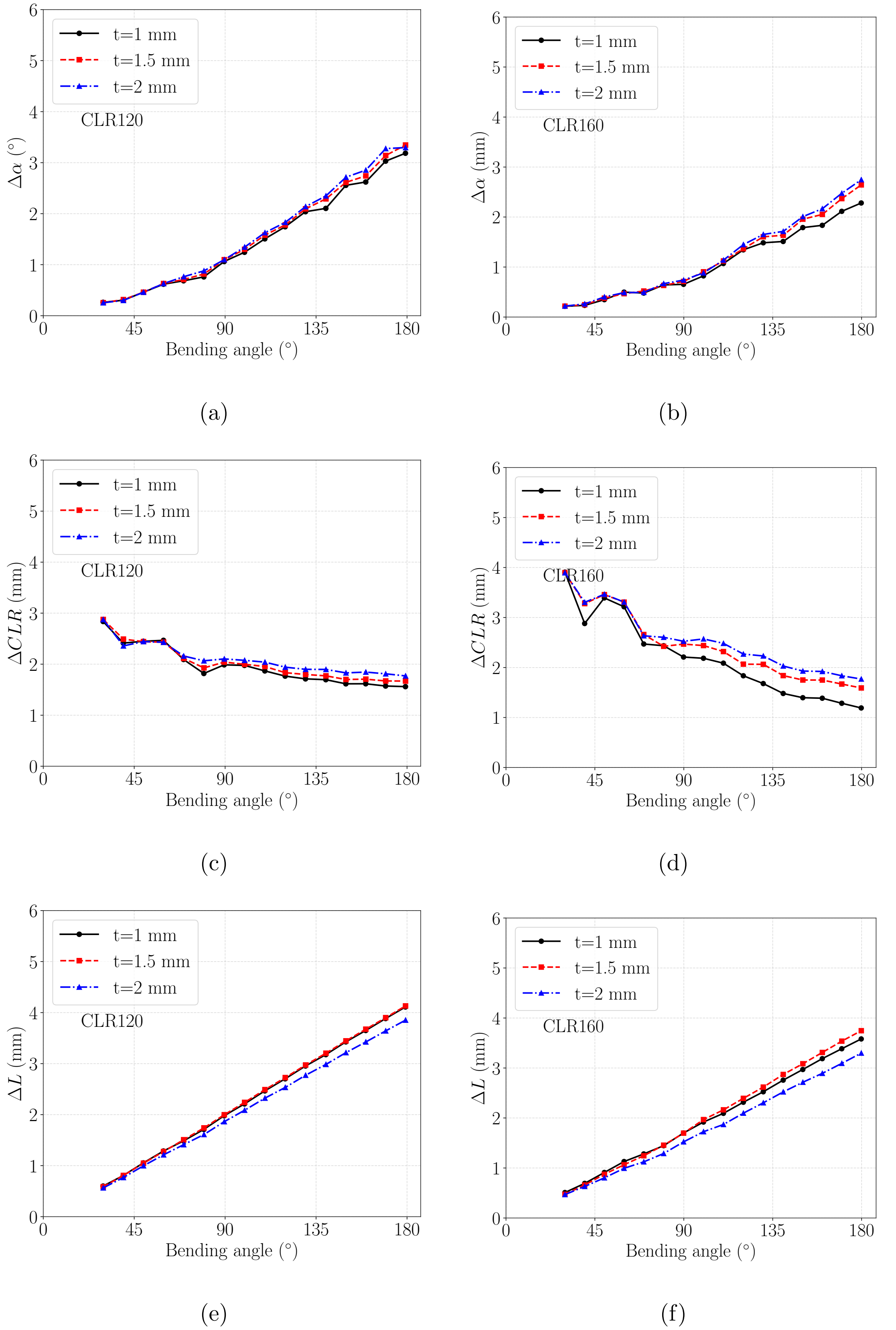

Figure 4.7: Effect of tube thickness on bending response when analysing SS304: (a–b) angular springback, (c–d) radial springback, and (e–f) final tube length for CLR = 120 mm and 160 mm.

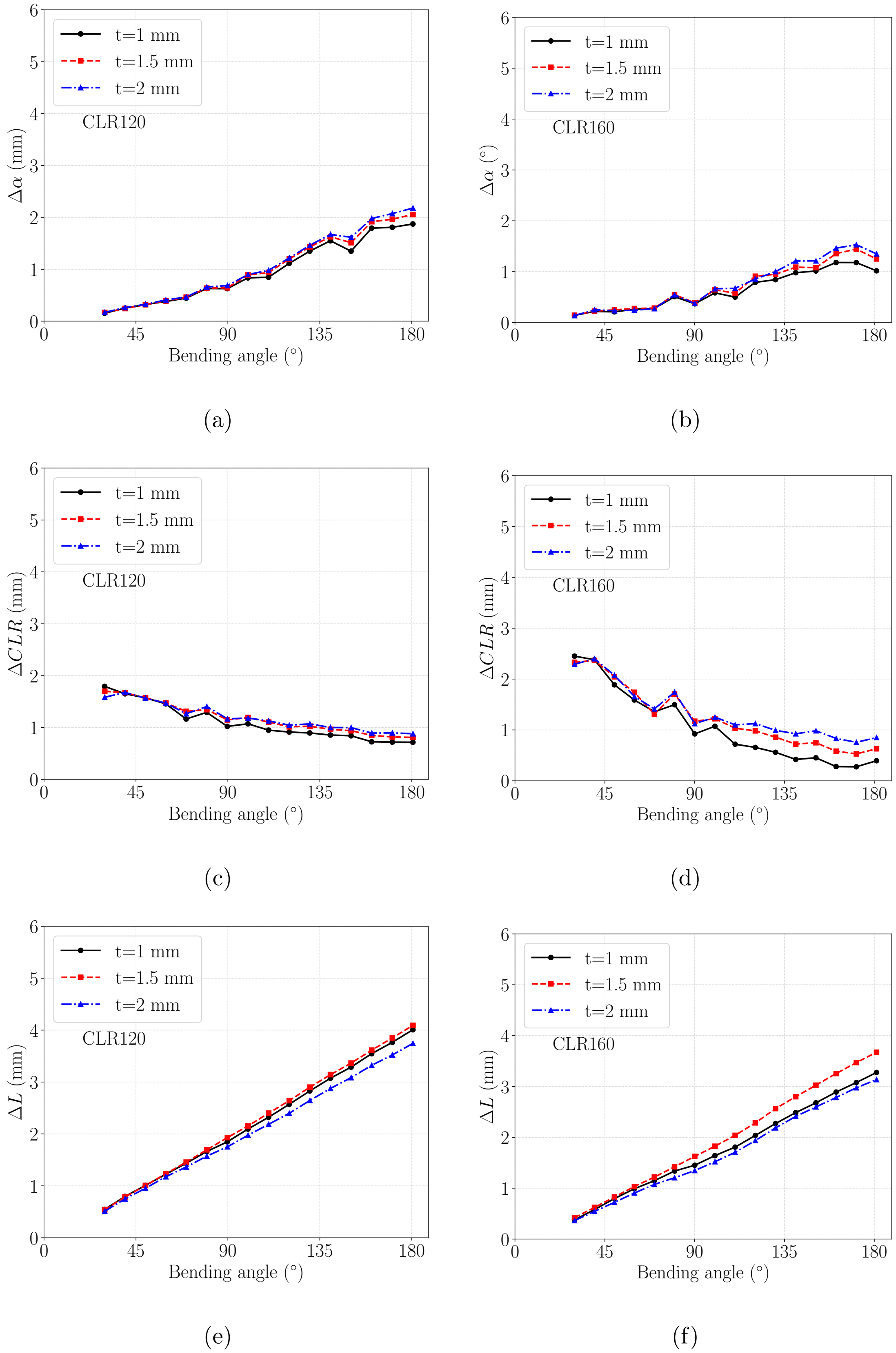

Figure 4.8: Effect of S235 tube thickness on bending response: (a–b) angular springback, (c–d) radial springback, and (e–f) final tube length for CLR = 120 mm and 160 mm.

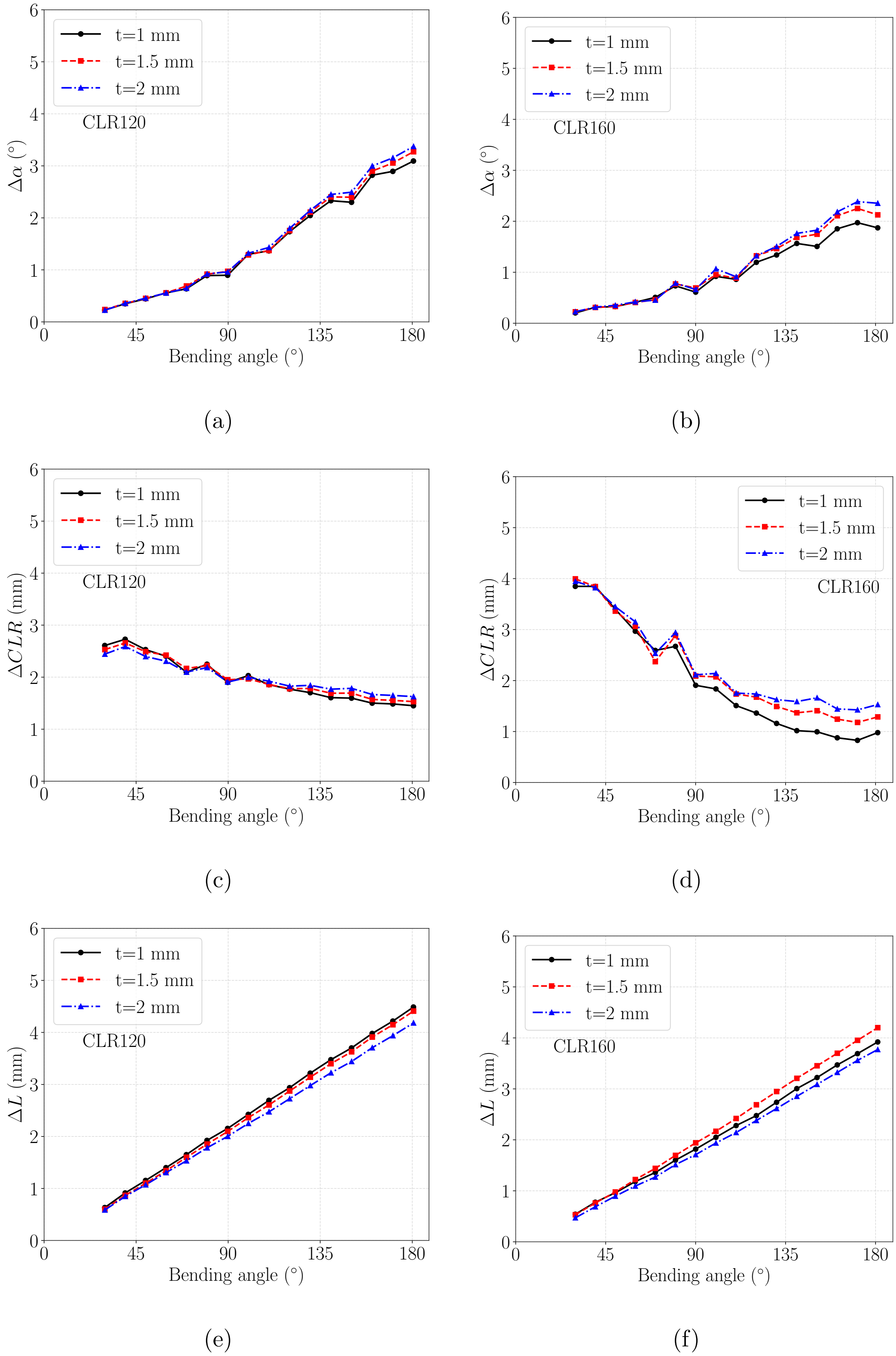

Figure 4.9: Effect of tube thickness on bending response when analysing Fe510: (a–b) angular springback, (c–d) radial springback, and (e–f) final tube length for CLR = 120 mm and 160 mm.

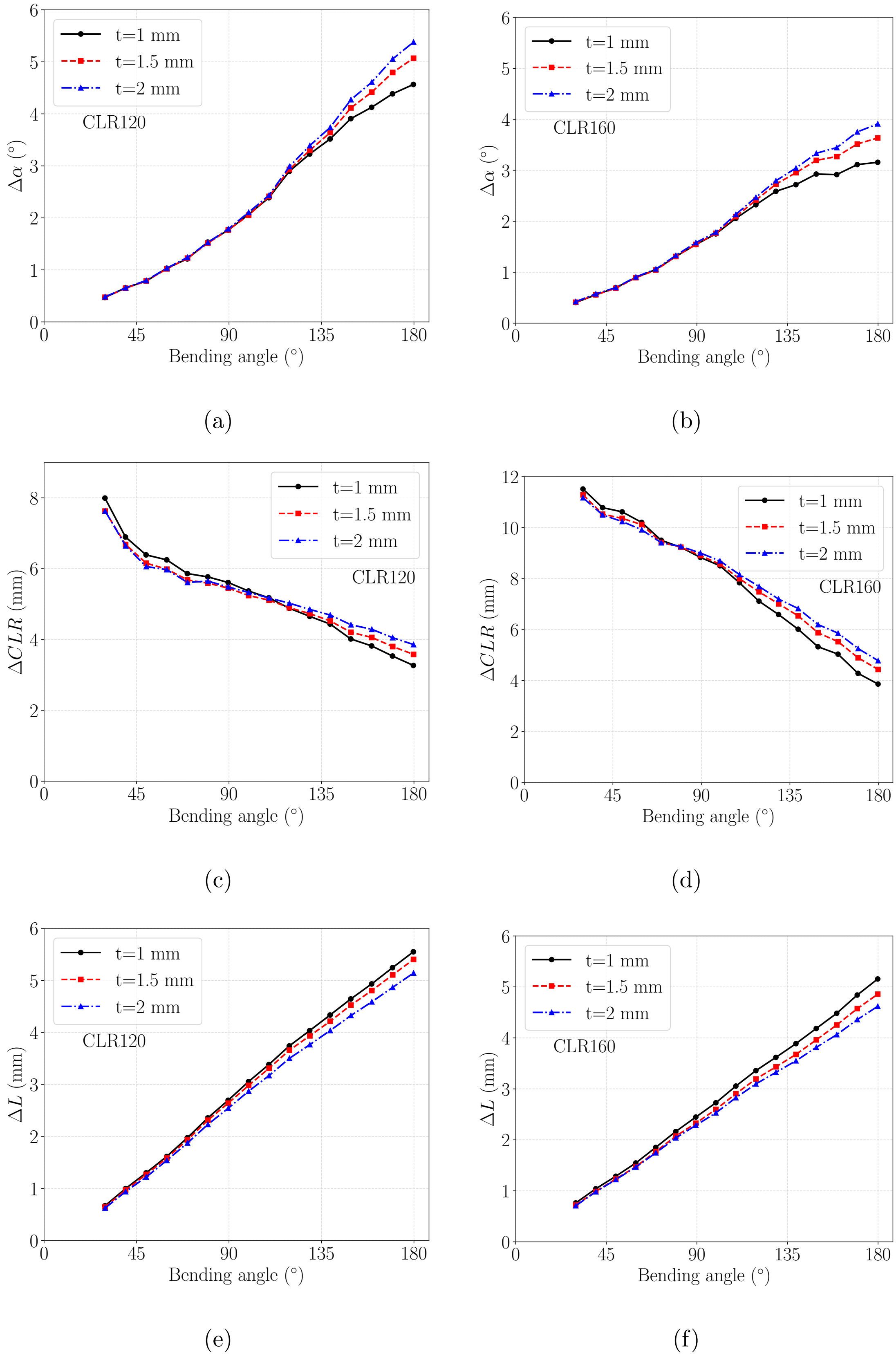

Figure 4.10: Effect of tube thickness on bending response when analysing Al2017A: (a–b) angular springback, (c–d) radial springback, and (e–f) final tube length for CLR = 120 mm and 160 mm.

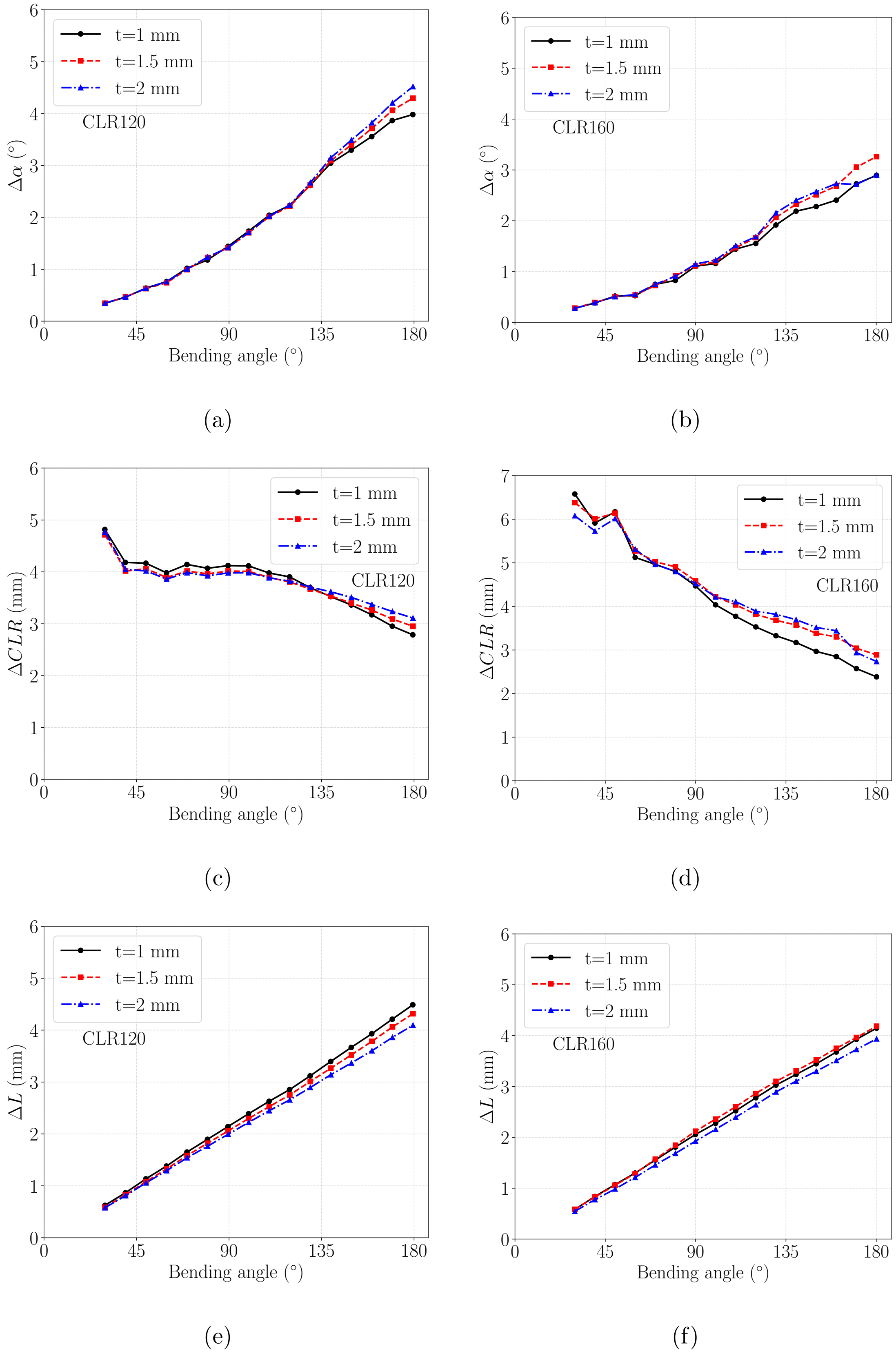

Figure 4.11: Effect of tube thickness on bending response when analysing Ti 99.5: (a–b) angular springback, (c–d) radial springback, and (e–f) final tube length for CLR = 120 mm and 160 mm.

A more detailed analysis was performed for the case of 1.5 mm wall thickness, focusing on materials SS304 and S235. As illustrated in Figures 4.12a and 4.12b, the effect of CLR on angular springback is clearly evident. Significant differences in the springback angle ($\Delta\alpha$) are observed between the two CLR configurations, underscoring the sensitivity of springback to geometric parameters in the bending process. In particular, the CLR120 configuration exhibits more pronounced angular springback compared to the larger CLR case, despite both following a similar overall trend. Additionally, the difference in angular springback between the two CLR values increases progressively with the bending angle, indicating that the influence of CLR becomes more critical at higher deformation levels. Specifically, for a bending angle of 180°, increasing the CLR results in a springback reduction of 0.703° for SS304 and 0.807° for S235, highlighting the significant impact of CLR on higher bending angles.

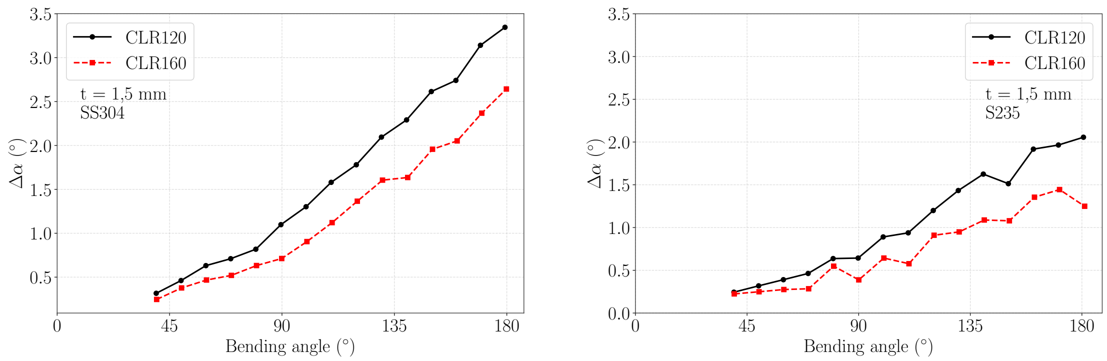

(a)

(b)

Figure 4.12: Influence of CLR in springback in angle for thickness 1.5 mm for a) SS304 and b) S235.

Figures 4.13a and 4.13b further illustrate the significant influence of the CLR, this time with respect to springback in radius (ΔCLR). The results clearly demonstrate distinct variations in springback in radius across the different CLR configurations, reinforcing the role of geometric parameters in shaping the final outcome of the bending process. In the case of CLR160, the springback in radius is particularly pronounced, whereas for CLR120, the values tend to stabilise, approaching a plateau. This behaviour can be explained by the less severe bending associated with a larger CLR, such as CLR160, which induces lower levels of plastic deformation and, consequently, results in less significant springback. As shown in Figures 4.14a and 4.14b, the CLR160 configuration exhibits a smaller plastified region (indicated by the grey area), which implies a higher springback compared to the CLR120 case.

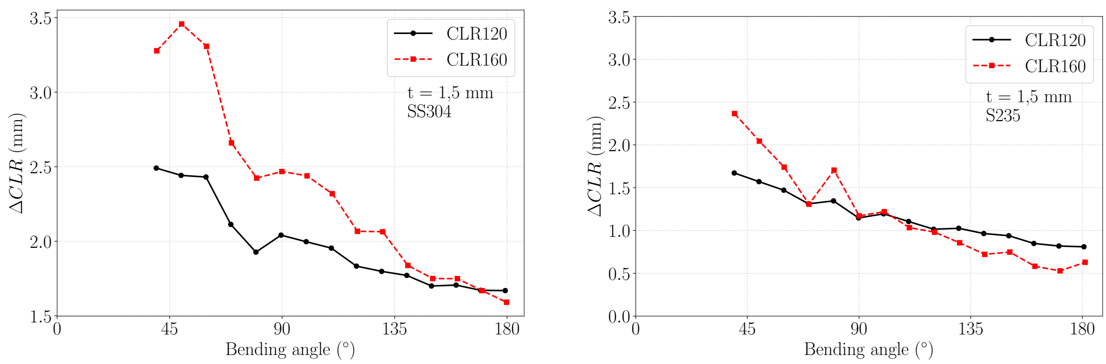

(a) (b)

Figure 4.13: Influence of CLR in springback in radius for thickness 1.5 mm for a) SS304 and b) S235.

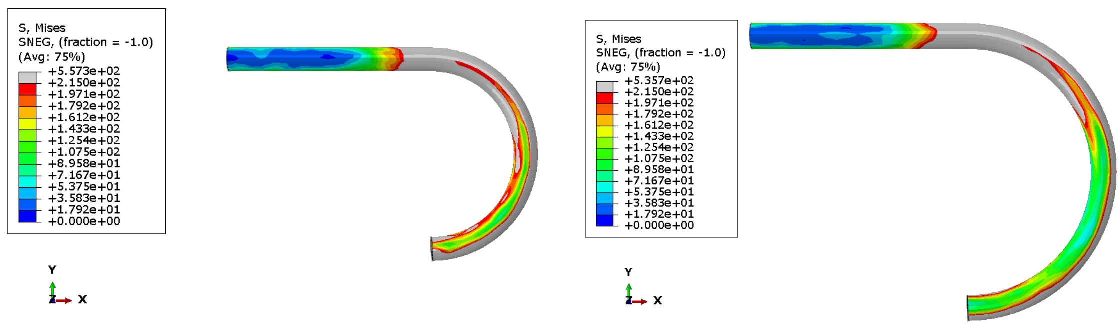

(a) (b)

Figure 4.14: Analysis of plastified area (grey area) for thickness 1.5 mm for SS304 when CLR is a) 160 mm or b) 120 mm.

Regarding elongation, the results presented in Figures 4.15a and 4.15b indicate that the configuration with a CLR of 120 mm exhibits greater elongation for both materials. Additionally, the differences in elongation between the two materials remain nearly constant as the bending angle increases, wiht a maximum value between them of 0.454 mm. This difference can be attributed to the equivalent plastic strain distributions presented in Figure 4.16. The CLR120 configuration exhibits a higher equivalent strain value (0.1314) compared to CLR160 (0.09877), which supports the observed increase in elongation associated with CLR120. In this figure, it is possible to observe that the regions of highest deformation are concentrated at the extrados and intrados of the bent section, as expected. The smaller bending radius in the

CLR120 setup promotes more extensive plastic deformation in these areas, resulting in higher elongation and reduced springback compared to the CLR160 configuration.

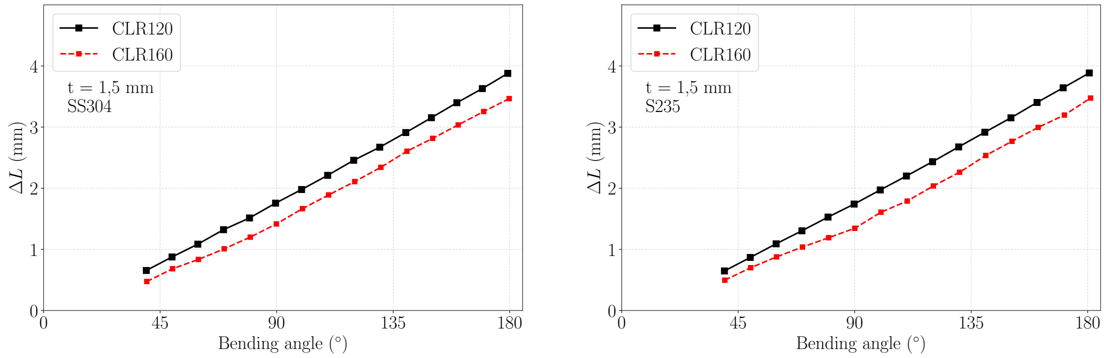

(a) (b)

Figure 4.15: Influence of CLR in elongation of the tube for thickness 1.5 mm for a) SS304 and b) S235.

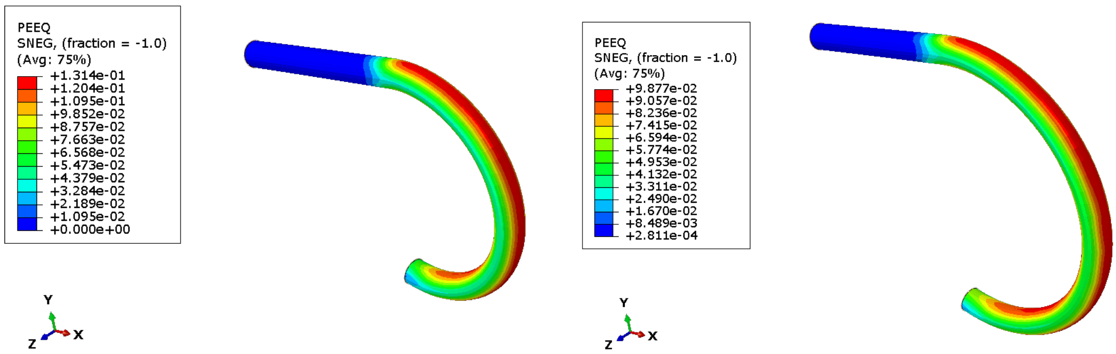

(a) (b)

Figure 4.16: Equivalent plastic defomormation for SS304 when a) CLR120 and b) CLR160.

To further understand the role of material behaviour in the rotary draw bending process, a comparative evaluation was conducted across the selected materials. The material comparison will focus on three primary case studies: Fe510 versus SS304, Fe510 versus S235, and Al2017A versus S235, using the data presented in Figure 4.17. As a general observation, the materials can be ranked in descending order of springback tendency as follows: Al2017A, Ti 99.5, SS304/Fe510 (which exhibit very similar behaviour), and S235. This trend highlights Al2017A as the material with the highest springback and S235 as the one with the lowest. Additional observations, which are consistent with previously discussed results, include the following trends: springback in angle increases with the bending angle; springback in radius decreases as the bending angle increases and tends to stabilise; and elongation increases progressively with the bending angle.

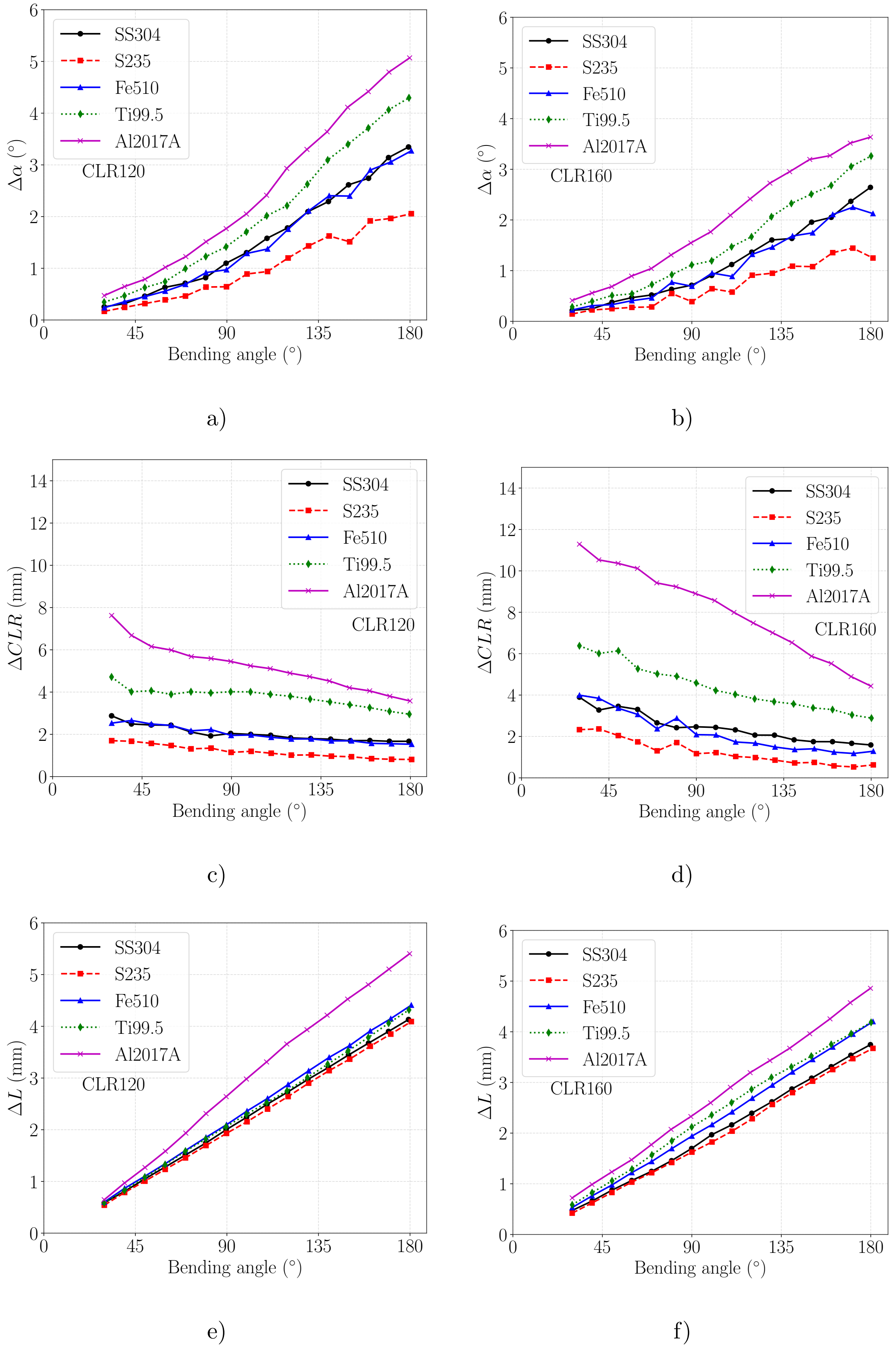

Figure 4.17: Analysis of springback in angle (a) and b)), springback in radius (c) and d)) and elongation (e) and f))for thickness 1.5 mm for CLR120 at left column and CLR160 at right column.

The comparison between SS304 and Fe510 serves as a starting point in this analysis. Although these materials present distinct mechanical properties overall, the similarity in the simulation results can be attributed to the fact that both exhibit nearly identical hardening behaviour around $\varepsilon_p \approx 0.15$ — the range of plastic strain typically developed in the bent region during the rotary draw bending process.

As seen in Figure 3.1, the hardening curves of SS304 and Fe510 converge in this strain range, which explains why both materials show nearly identical trends in springback and elongation under the same bending conditions. This interpretation is further supported by the von Mises stress distributions shown in Figures 4.18a and 4.18b, which reveal similar stress fields and regions of concentration, despite a modest difference in peak stress values (approximately 30 MPa).

Additionally, Figures 4.19a and 4.19b indicate that the equivalent plastic strain in both materials differs by only 0.00163, reinforcing the conclusion that their mechanical response under bending is effectively the same due to their aligned behaviour within the relevant plastic strain range. These values are consistent with the deformation levels discussed earlier, particularly around $\varepsilon_p \approx 0.15$, further supporting the similarity in forming behaviour between SS304 and Fe510.

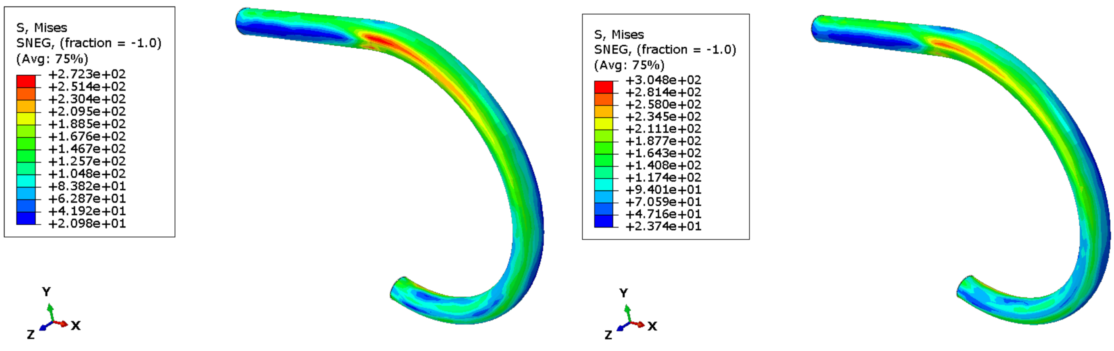

(a) (b)

Figure 4.18: von Mises stress distribution of a) SS304 and b) Fe510 when the CLR is 160 mm and the thickness is 1.5 mm.

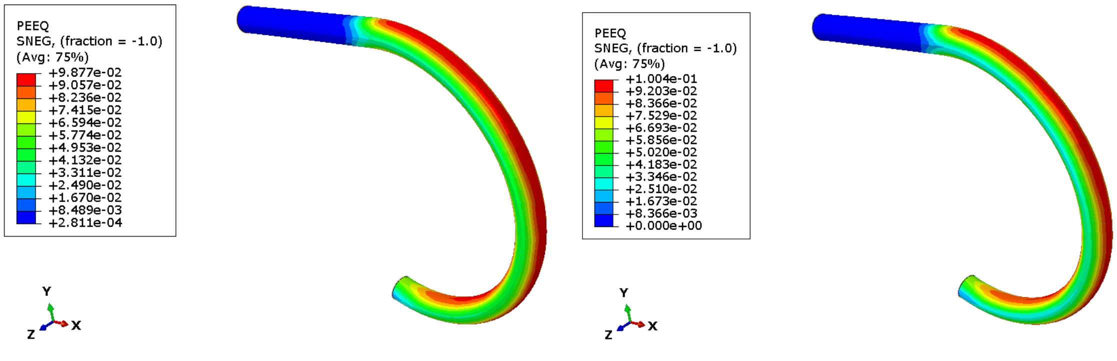

(a) (b)

Figure 4.19: Equivalent plastic deformation of a) SS304 and b) Fe510 when the CLR is 160 mm and the thickness is 1.5 mm.

Moving on to the analysis of Fe510 versus S235, these two materials exhibit some similar mechanical properties as the Young's Modulus, but differ significantly in their hardening behaviour. In such cases, springback tends to be more pronounced in the material with higher strength — in this case, Fe510. This trend can be explained by the stress–strain behaviour illustrated in the left plot of Figure 4.20, where higher strength steels (like Fe510) exhibit greater elastic recovery upon unloading. Despite both materials having the same elastic modulus, the greater stress level in Fe510 leads to a larger elastic recovery upon unloading, which results in increased springback. In Figure 4.17, it is possible to see that Fe510 consistently exhibits greater springback in radius and angle than S235, as expected.

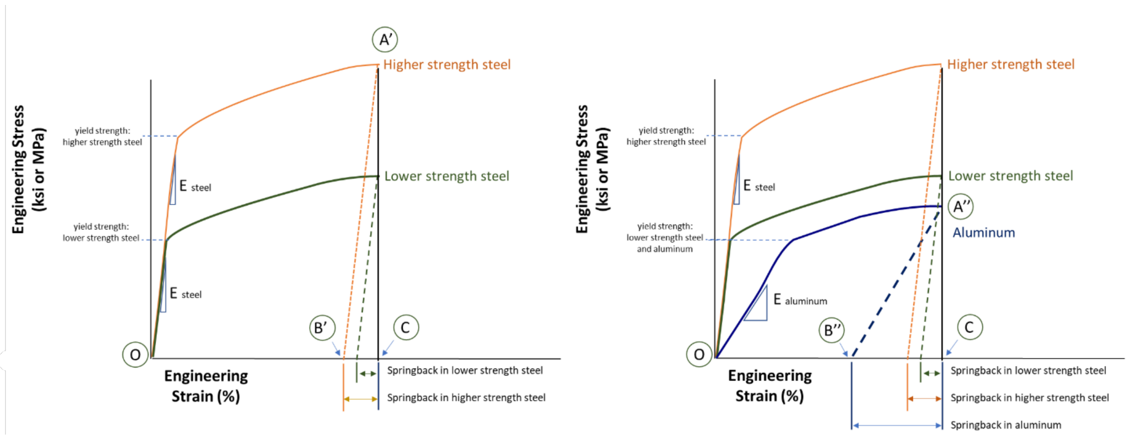

Figure 4.20: Influence of elastic modulus, yield strength and work hardening in different materials [31].

Finally, the comparison between Al2017A and S235 involves two materials with distinct mechanical properties but similar hardening behaviour. This observation highlights the dominant influence of Young's Modulus on springback behaviour. Although Al2017A and S235 exhibit similar hardening behaviour (characterised by comparable hardening exponents (n)) the significant difference in Young's Modulus, approximately 130 GPa, leads to markedly different springback responses. Al2017A, having the lower modulus, shows a much higher springback, underscoring the primary role of elastic stiffness over hardening in this context. As illustrated in the right plot of Figure 4.20, aluminium alloys such as Al2017A possess a considerably lower Young's Modulus compared to steels, which leads to a larger elastic recovery region during unloading, and so a higher springback.

An additional aspect of interest is the analysis of the von Mises stress distribution throughout the RDB process. Figure 4.21 illustrates the evolution of stress across 20 sequential tube configurations after springback (SB1–SB20, corresponding to bending angles from 10° to 200°), highlighting the progression of deformation in Al2017A tubes with a wall thickness of 1.5 mm and a CLR of 160 mm. This sequence provides valuable insights into the gradual accumulation of stress during bending. At the initial stages, the stress is relatively low and uniformly distributed; however, as the bending angle increases, pronounced stress concentrations develop, particularly at the intrados and extrados regions of the tube. By the final configuration (SB20), the highest stress levels are observed, reflecting the material's response to significant plastic deformation. This analysis emphasises the critical importance of monitoring stress evolution during RDB to ensure effective process control and to minimise the risk of failure or excessive distortion.

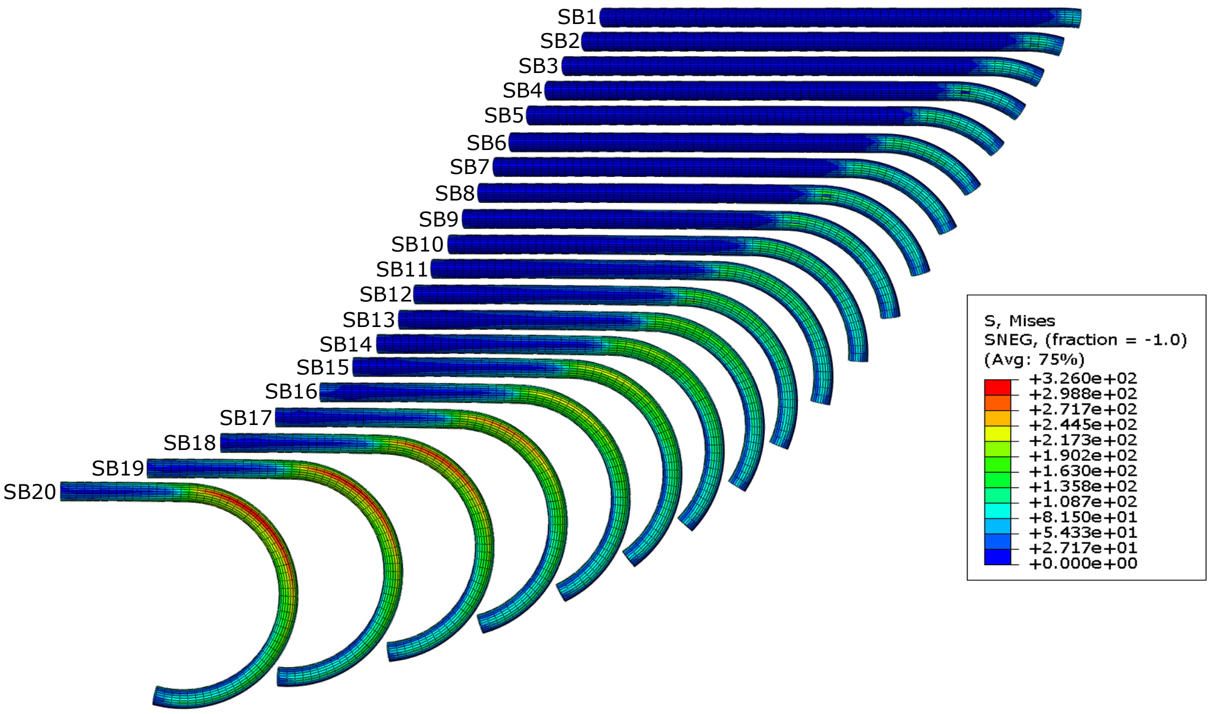

Figure 4.21: Evolution of von Mises stress across 20 tube configurations (10°-200°).

4.2 Experimental Validation

This section presents the validation of the numerical model by comparing the simulation results with experimental data, for 2D bends and 3D bends. Additionally, the repeatability of the process and accuracy of the Hexagon measurement machine are analysed.

4.2.1 2D Bending Analysis

To validate the numerical model developed in this study, a direct comparison was carried out between the simulation results and experimental measurements for 2D tube bending, following the methodology outlined in Section 3.4. The experiments and simulations were performed under identical conditions, using the same combinations of material (SS304 and S235), wall thickness (1.5 mm and 2 mm), centerline radius (CLR120 and CLR160), and bending angles (45°, 70°, 90°, 150°, and 180°).

Figures 4.22 to 4.25 present this comparison in terms of angular springback ($\Delta\alpha$), springback in radius (ΔCLR), and tube elongation (ΔL). Figure 4.22 corresponds to SS304 with a thickness of 1.5 mm for both CLR values, while Figure 4.23 shows results for S235 with wall thicknesses of 1.5 mm and 2 mm, also for CLR120 and CLR160. Figure 4.24 displays the results for SS304 and S235 with a thickness of 2 mm and CLR160, and Figure 4.25 refers to the case with 2 mm thickness and CLR120 for both materials.

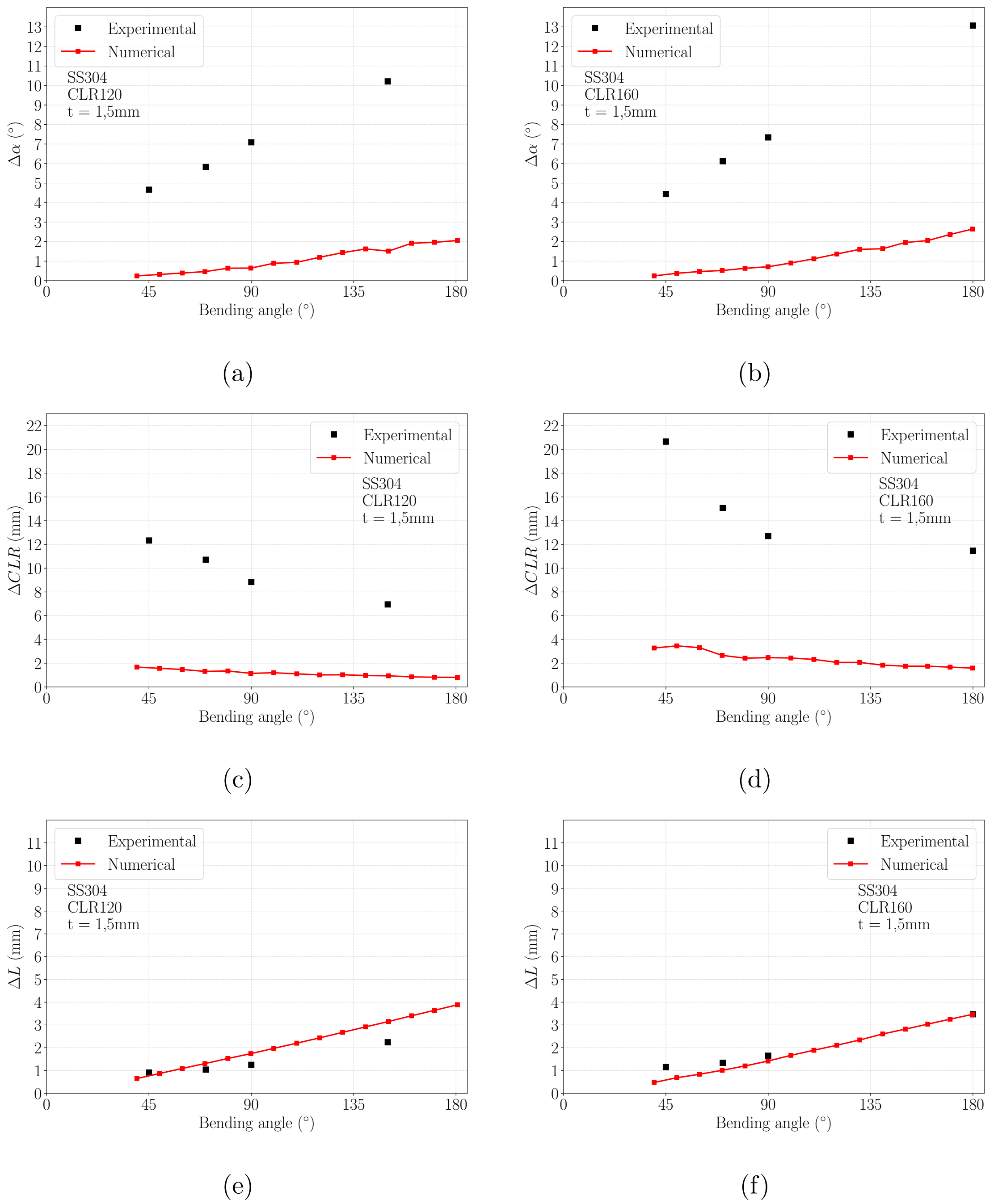

Figure 4.22: Comparison between experimental and numerical data regarding spring-back in angle and radius as well as elongation of tubes: a), c) and e) correspond to SS304, CLR120 and thickness of 1.5 mm combination and b), d) and f) correspond to SS304, CLR160 and thickness of 1.5 mm.

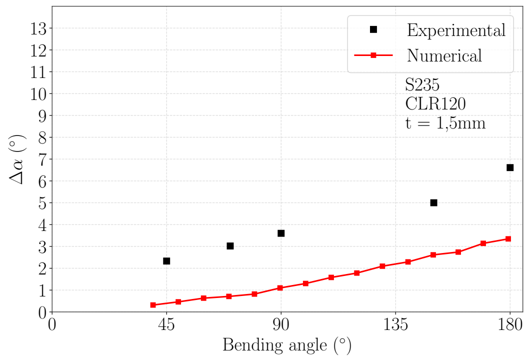

(a)

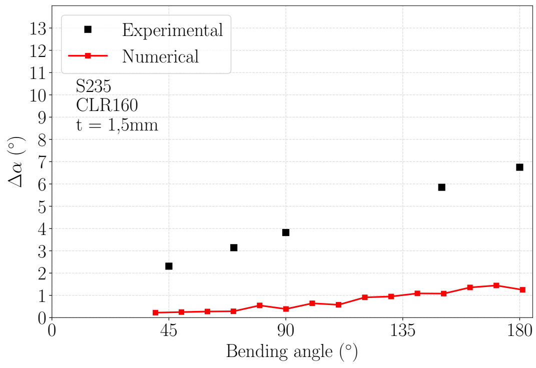

(b)

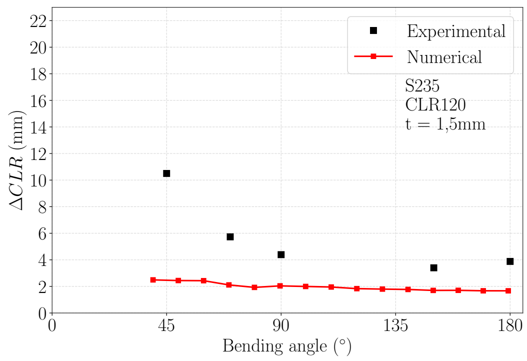

(c)

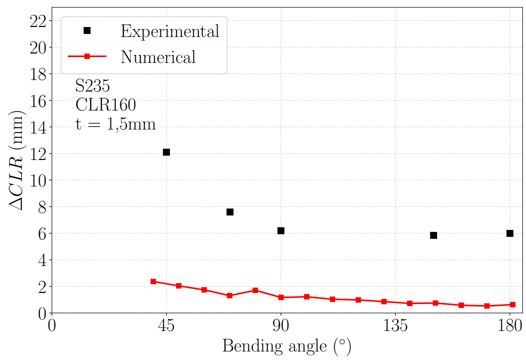

(d)

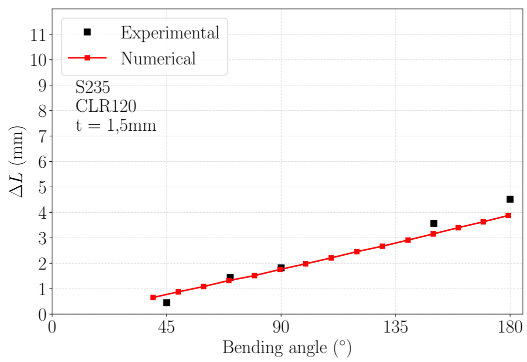

(e)

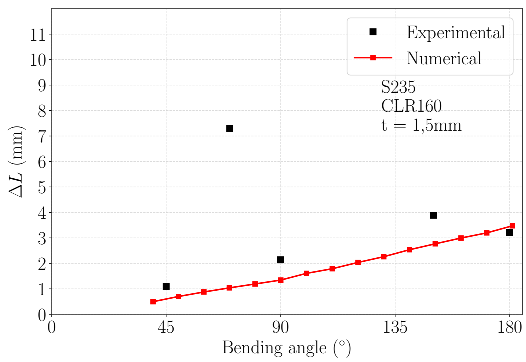

(f)

Figure 4.23: Comparison between experimental and numerical data regarding spring-back in angle and radius as well as elongation of tubes: a), c) and e) correspond to S235, CLR120 and thickness of 1.5 mm combination and b), d) and f) correspond to S235, CLR160 and thickness of 1.5 mm.

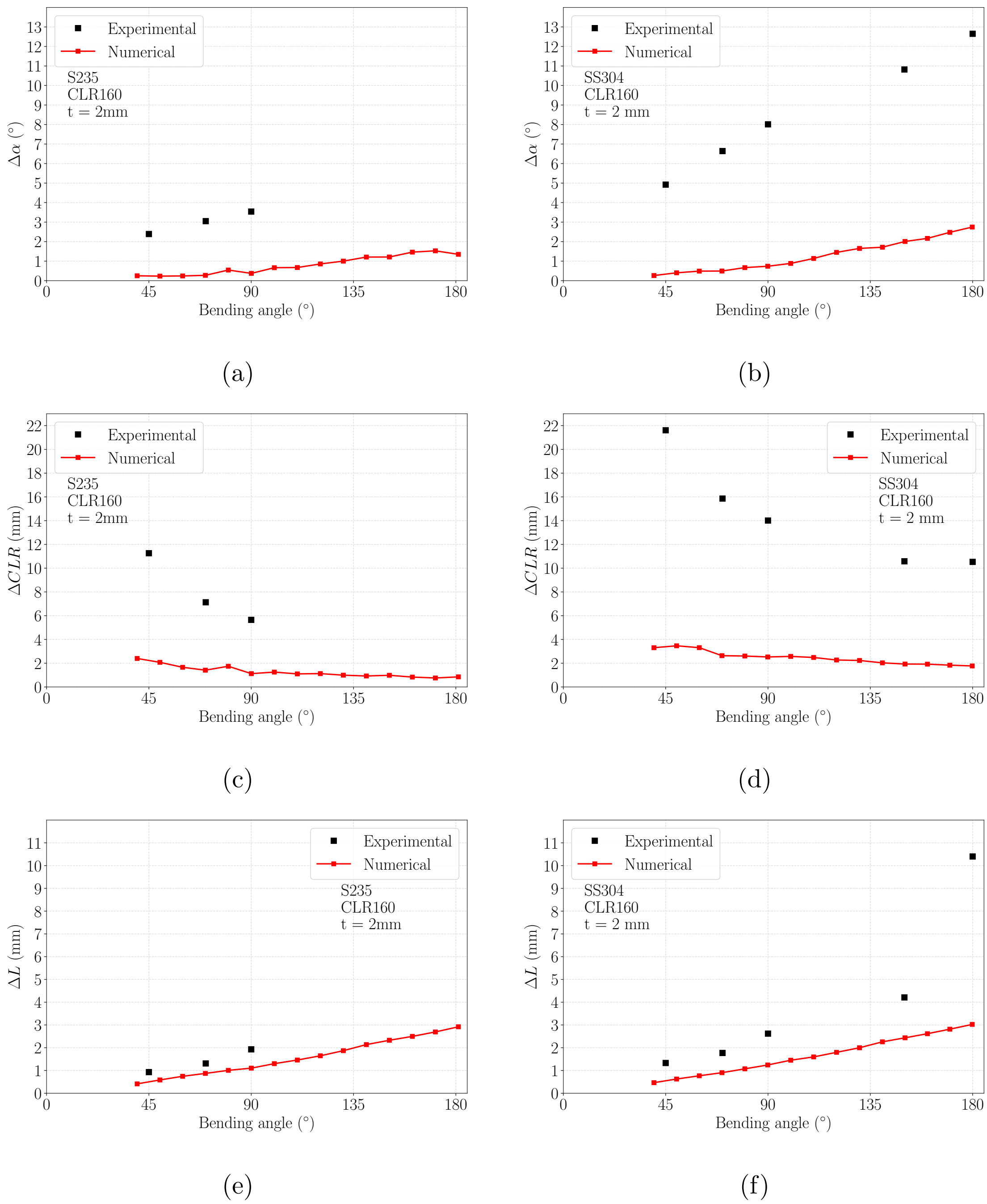

Figure 4.24: Comparison between experimental and numerical data regarding spring-back in angle and radius as well as elongation of tubes: a), c) and e) correspond to S235, CLR160 and thickness of 2 mm combination and b), d) and f) correspond to SS304, CLR160 and thickness of 2 mm.

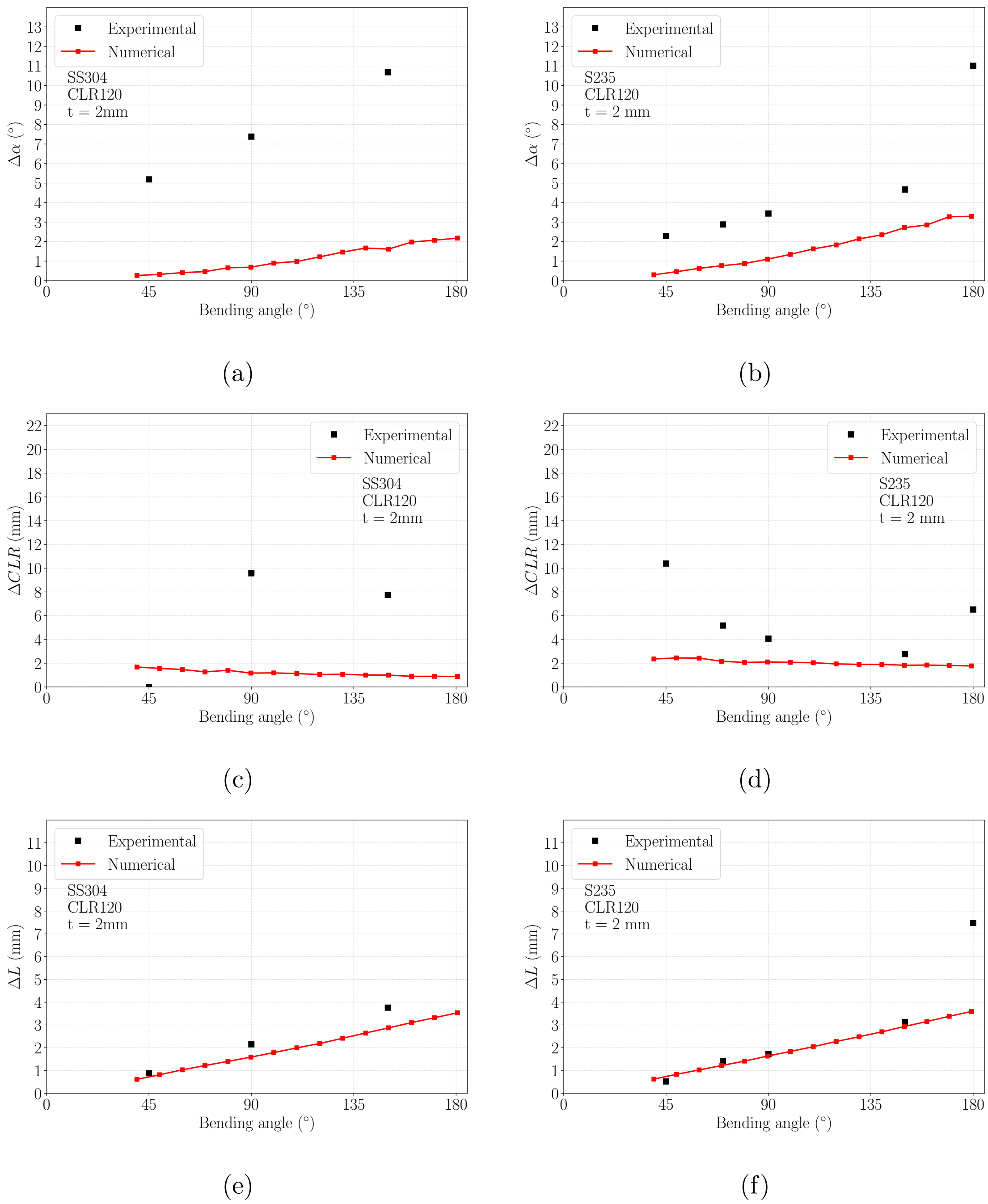

Figure 4.25: Comparison between experimental and numerical data regarding spring-back in angle and radius as well as elongation of tubes for SS304 and S235 when the CLR is 120mm and thickness is 2 mm.

After analysing all the data, a clear distinction between numerical and experimental results can be observed in $\Delta\alpha$ and ΔCLR, while variations in ΔL are less pronounced. However, although some discrepancies exist in terms of magnitude, the curves generally follow similar profiles, particularly as the bending angle increases.

The numerical predictions of ΔL align closely with the experimental measurements across all configurations, indicating that the model performs well in capturing the global deformation of the tube. In contrast, the discrepancies observed in $\Delta\alpha$ and ΔCLR are more difficult to interpret and likely result from a combination of contributing factors. Despite the offset between the experimental data and the numerical predictions, a consistent trend is noticeable across the corresponding plots, indicating that the numerical model captures the overall response reasonably well.

Several factors may contribute to the observed discrepancies, particularly in the predictions of $\Delta\alpha$ and ΔCLR. Firstly, a relevant aspect is the uncertainty regarding the material mechanical behaviour of the tested tubes. Since no material characterisation tests were conducted, the mechanical properties used in the simulations were based solely on supplier data. This mismatch could significantly affect the correlation between experimental and numerical outcomes, since the constitutive model adopted (based on the von Mises yield criterion with isotropic Swift hardening) may not capture the full complexity of material behaviour under multi-axial and non-proportional loading conditions that can occur during tube bending.

In addition to material uncertainty, modelling assumptions can also impact the accuracy of the predictions. The use of shell elements with reduced integration, although computationally efficient, may be insufficient to accurately capture stress and strain gradients through the tube thickness. Employing solid elements could improve the fidelity of the model, especially in capturing through-thickness behaviour during springback.

Another relevant point concerns the solver configuration. One stage of the simulation was carried out using an explicit solver, which may introduce unintended dynamic effects in a quasi-static process like rotary draw bending. A static formulation would likely reduce these influences and improve correlation with experimental results. Furthermore, in the springback step, a default damping factor was used without calibration. Exploring alternative damping values could potentially enhance the accuracy of elastic recovery predictions. Finally, it is important to note that the experimental measurements are limited to the final geometry, with initial reference values for bending angle and radius of curvature assumed based on equipment settings. As such, the observed differences may also stem from uncertainties in the experimental setup and measurement assumptions, not only from the numerical model. In contrast, the evaluation of tube elongation (ΔL) is considered more reliable, as both the initial and final lengths were measured experimentally. This initial baseline likely contributes to the closer agreement observed between numerical and experimental results for ΔL. On the other hand, the lack of reference data for α and CLR highlights the need for more comprehensive experimental procedures, particularly before springback, to ensure more accurate validation of numerical simulations.

To ensure the reliability and credibility of the experimental final geometry data, a repeatability analysis was conducted by measuring two tubes bent under identical conditions. Both tubes were made of SS304 with a wall thickness of 2 mm, a CLR of 120 mm, and a bending angle of 180°. Repeatability in measurement refers to the ability to obtain consistent results when the same procedure is repeated under the same conditions, using the same equipment and operator. In this study, repeatability was addressed by maintaining controlled environmental conditions and ensuring uniform parameters throughout the bending process.

Table 4.4 presents the values obtained from the two measurement reports generated by Hexagon BendingStudio XT, specifically regarding the deviations in CLR (ΔCLR), bending angle ($\Delta\alpha$), and tube length (ΔL). It can be observed that the relative error for each variable is minimal, indicating a high level of consistency. As a result, the measurement method demonstrates good applicability and reliability for this type of analysis.

Table 4.4: Comparison between the two tubes measurements.

	CLR (mm)	Bending angle (°)	Length (mm)
Tube1	126.52	168.99	827.48
Tube2	126.44	169.08	826.97
Relative error (%)	0.067	0.050	0.062

Due to unexpected deviations between experimental and numerical in some of the initial measurements, an alternative measurement technology was employed to reassess one of the test tubes, following the methodology of sub-section 3.4.2. Specifically, a stainless steel tube (SS304) with a wall thickness of 2 mm, a CLR of 120 mm, and a bending angle of 180° was selected for this re-evaluation. The measurement was carried out using the ATOS Triple Scan system developed by GOM.

After the scanning process, the resulting geometry was compared with an ideal CAD reference tube, as shown in Figure 4.26. Based on this comparison, the CLR and bending angle were determined. The CLR was determined by selecting three points along the arc of the bend and constructing a best-fit circle through these points. The radius of this circle was then measured and combined with the tube's outer radius to obtain the CLR. The bending angle was measured by creating reference axes along the straight sections at both ends of the tube. These axes were constructed by fitting cylinders to the end segments, and the angle between the two axes was calculated to determine the overall bending angle.

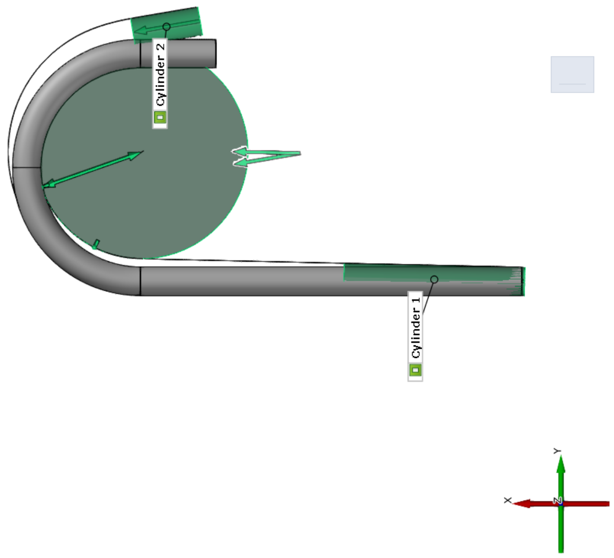

Figure 4.26: Comparison between optimal CAD and scanned geometry.

The scan results are presented in Table 4.5. When compared with the Hexagon measurements obtained under identical material and geometric conditions, the differences observed are minimal, thereby confirming the consistency and reliability of the measurement processes.

Table 4.5: Values of CLR and bending angle from ATOS and Hexagon measurements.

	CLR (mm)	Bending angle (°)
ATOS	127.33	169.11
Hexagon	126.44	169.08

4.2.2 3D Bending Analysis

Following the analysis of two-dimensional bending cases, the validation of the numerical model was extended to more complex geometries involving three-dimensional bending. The comparison between numerical and experimental results for 3D tube configurations provides an additional layer of validation, offering insight into the model's predictive capabilities under more realistic and industrially relevant conditions. The specific case under analysis is illustrated in Figure 4.27.

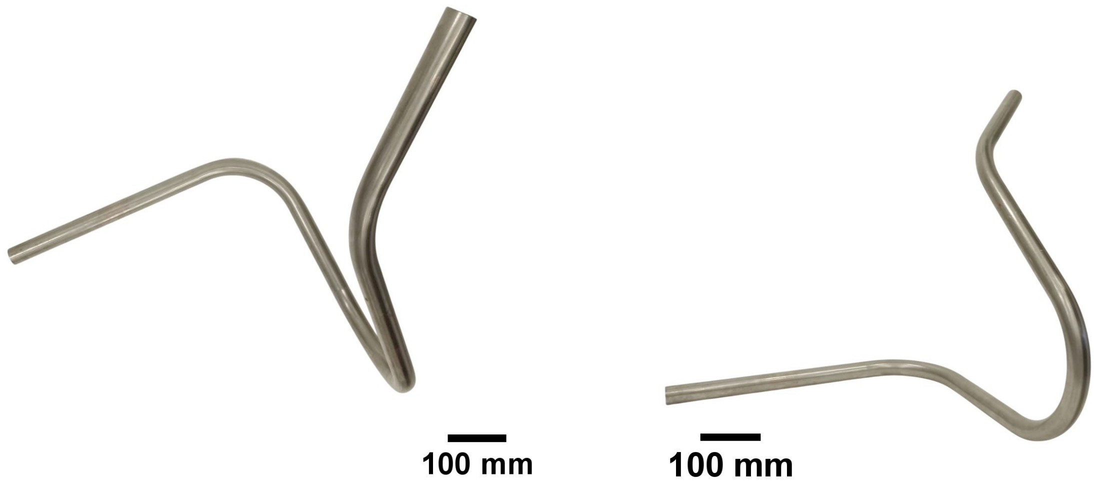

(a) (b)

Figure 4.27: Real case for validation.

The analysis strategy for this case was conducted on a bend-by-bend basis, as the entire part was not fully simulated. This approach is appropriate due to the absence of tangency points between bends, resulting in straight sections that separate each bend. However, it is important to note that this strategy is not applicable when tools with a variable CLR are used, as the geometry and deformation become more complex and interdependent.

The case for validation is composed by:

- bend of 45° with CLR 160
- bend of 145° with CLR 160 with rotation of -90°
- bend of 90° with CLR 160 with rotation of -90°

Table 4.6 presents a comparison between numerical predictions and experimental measurements for both bending angle and CLR in each individual segment, enabling a direct assessment of the model's accuracy in a multi-bend 3D configuration.

Table 4.6: Comparison of numerical and experimental data from real validation case.

	Bending angle (°)		CLR (mm)	
	Numerical	Experimental	Numerical	Experimental
45º - CLR160	0.3	4.4	3.4	14.3
145º - CLR120	2.4	9.23	1.7	6.91
90º - CLR120	1.1	7.11	2	8.99

Regarding the variation in tube length, the results are summarised in Table 4.7. The numerical value was obtained by consulting the elongation plot for the corresponding material and thickness (see Figure 4.7e), from which the individual contributions of each bend were extracted and summed. The resulting value (6.2 mm) shows good agreement with the experimental measurement (5.33 mm), with a difference of less than 1 mm, which confirms the model's ability to accurately predict cumulative elongation in multi-bend configurations.

Table 4.7: Results for variations in tube length.

Numerical	0.8+3.4+2=6.2 mm
Experimental	5.33 mm

Overall, the results demonstrate good agreement between the numerical and experimental data, particularly regarding trends in springback behaviour and final tube geometry. This correlation confirms that the model is generally robust and capable of capturing the key physical phenomena involved in the RDB process.

Nevertheless, some deviations were observed, especially in the angular springback values. These discrepancies can be attributed to several factors. First, simplifications inherent in the numerical model such as neglect of tool wear, and assumptions regarding friction, can limit its accuracy. Second, uncertainties in the experimental measurements, including potential errors in 3D scanning and variations in material properties, may also contribute to the observed differences.

Despite these limitations, the validation results suggest that the model is sufficient for predictive purposes and can be used as a tool for optimization of the RDB process.

Chapter 5

Conclusions

This thesis focused on analysing the RDB process with respect to springback and stretching phenomena using a numerical approach. The primary objective was to simplify the understanding of the manufacturing process by employing FEM through ABAQUS software. Additionally, the study aimed to evaluate the influence of key process parameters, namely the bending angle (α), CLR and tube thickness (t), on the final geometry and deformation behaviour.

The following conclusions were drawn concerning the effect of process parameters:

1. Increasing the CLR reduces angular springback, but leads to an increase in springback at the radius. The elongation is higher for lower CLR, as a result of increased plastic deformation, particularly in the extrados of the tube. For the range of CLRs analysed, the impact on tube elongation is relatively minimal, with a maximum difference of 0.545 mm observed.

2. A larger bending angle results in increased angular springback, a decrease in radius springback, and a greater elongation of the tube's overall length. This elongation occurs because of the higher degree of plastic deformation in the extrados of the tube.

In relation to material properties and geometric factors:

1. Tubes with greater wall thickness exhibit higher angular and radial springback, although the impact on total tube elongation is comparatively less significant. In general, tube thickness has a low impact on the variables studied.

2. Despite Al2017A and S235 exhibiting similar hardening behaviour, Al2017A demonstrates higher springback in angle, radius, and total length. This can

be primarily attributed to its lower young's modulus, which plays a more dominant role in the bending response than the hardening parameters alone.

3. SS304 and Fe510 exhibited nearly identical bending responses, driven by their similar hardening behaviour. Both materials showed comparable springback, elongation, and stress distribution, indicating consistent forming behaviour under identical conditions.

Despite the differences observed between the experimental and numerical data, a consistent trend is evident, indicating that the proposed approach is promising and progressing in the right direction for future discoveries. The application of two 3D digitisation methods demonstrated the consistency of the experimental results, thereby enabling the identification of potential discrepancies between experimental and numerical results. However, it is important to note that the experimental measurements are limited to the final geometry, with initial reference values assumed based on equipment settings (e.g., bending angle and curvature radius). As such, the observed differences may also be the result of uncertainties in the experimental setup and measurement assumptions, not solely from the numerical model. These aspects will be further investigated and refined in future work.

These findings emphasise the importance of considering both geometric and material characteristics when aiming to control springback and deformation in the RDB process.

5.1 Future Works

Although the numerical model yielded satisfactory results, several aspects can be improved in future work. The current use of shell elements with reduced integration, while efficient, may not fully capture the through-thickness behaviour of thin-walled tubes. Employing solid elements with suitable formulations could enhance the accuracy of stress and deformation predictions.

Additionally, the bending simulations were conducted using an explicit dynamic solver. Despite the kinetic energy remaining lower than the internal energy, indicating limited dynamic effects, a static implicit approach may better represent the quasi-static nature of the bending process, eliminating residual inertial influences.

In the springback step, the default damping factor in ABAQUS was used. A sensitivity analysis on this parameter could contribute to more accurate predictions of elastic recovery. Furthermore, although the deformation levels were relatively low, future models would benefit from incorporating experimentally derived material data to ensure a more accurate representation of mechanical behaviour and to reduce reliance on generic datasets.

To build upon the insights gained in this study, future work should also focus more in reproducibility. This includes ensuring consistent outcomes under identical input conditions, both in simulations and experiments. Additional bending trials are recommended to evaluate the repeatability of the results and validate the robustness of the methodology.

Additionally, measuring the bending angle and curvature radius prior to springback will be explored to increase the accuracy and reliability of the experimental results.

The inclusion of tooling such as a mandrel and wiper die in both numerical and experimental setups would also be an important improvement. These tools play a crucial role in industrial tube bending, particularly for tight radii or thin-walled tubes, helping to minimise defects like wrinkling or cross-sectional distortion and enabling a more realistic simulation of actual manufacturing conditions.

Finally, expanding the study to cover a broader range of tube geometries and materials would provide a more comprehensive understanding of the process. Additionally, the integration of artificial intelligence and machine learning techniques could support the analysis of large datasets, helping to optimise process parameters and predict outcomes such as springback and defect formation more efficiently, only after having an accurate numerical model.

References

[1] A. Kumar. Optimizing the rotary draw tube bending process to avoid wrinkles. *International Journal of Modelling and Simulation*, 28(3):281–291, January 2008. ISSN 1925-7082. doi: https://doi.org/10.1080/02286203.2008.11442479.

[2] He Yang, Heng LI, Zhiyong Zhang, Mei ZHAN, Jing LIU, and Guangjun LI. Advances and trends on tube bending forming technologies. *Chinese Journal of Aeronautics*, 25(1):1–12, February 2012. ISSN 1000-9361. doi: 10.1016/S1000-9361(11)60356-7.

[3] Marta Oliveira José Bessa Pacheco, José Manuel Oliveira and Ana Reis. Dobragem de tubos. *Revista Tecnometal*, (244):10–22, 2019.

[4] Marta Oliveira José Bessa Pacheco, José Manuel Oliveira and Ana Reis. Dobragem de tubos. *Revista Tecnometal*, (243):10–19, 2019.

[5] AMOB. Naval and offshore, 2025. URL `https://amobgroup.com/pt-pt/setores/naval-e-offshore`. Accessed on June 16, 2025.

[6] Omni-X. Rotary draw bending, 2024. URL `https://www.omni-x.com/rotary-draw-bending`. Accessed: 2025-02-11.

[7] Cristiano Mosqueira. *Finite Element Analysis of flexible pipes: Bending Combined with tensile Load*. PhD thesis, 10 2017.

[8] Feifei Song, He Yang, Heng Li, Mei Zhan, and Guangjun Li. Springback prediction of thick-walled high-strength titanium tube bending. *Chinese Journal of Aeronautics*, 26(5):1336–1345, October 2013. ISSN 1000-9361. doi: https://doi.org/10.1016/j.cja.2013.07.039.

[9] S.K. Panthi, N. Ramakrishnan, K.K. Pathak, and J.S. Chouhan. An analysis of springback in sheet metal bending using finite element method (fem). *Journal*

of Materials Processing Technology, 186(1–3):120–124, May 2007. ISSN 0924-0136. doi: 10.1016/j.jmatprotec.2006.12.026.

[10] A.M. Prior. Applications of implicit and explicit finite element techniques to metal forming. *Journal of Materials Processing Technology*, 45(1–4):649–656, September 1994. ISSN 0924-0136. doi: https://doi.org/10.1016/0924-0136(94)90413-8.

[11] M. Strano. Automatic tooling design for rotary draw bending of tubes. *The International Journal of Advanced Manufacturing Technology*, 26(7–8):733–740, October 2005. ISSN 1433-3015. doi: 10.1007/s00170-003-2055-6.

[12] Linda Borchmann, Christopher Heftrich, Jonas Knoche, Michael Schiller, and Bernd Engel. Control of material flow using measuring methods for wrinkle and crack detection during rotary draw bending. *Procedia CIRP*, 118:857–862, 2023. ISSN 2212-8271. doi: 10.1016/j.procir.2023.06.147.

[13] X. Xue, J. Liao, G. Vincze, and J.J. Gracio. Modelling of mandrel rotary draw bending for accurate twist springback prediction of an asymmetric thin-walled tube. *Journal of Materials Processing Technology*, 216:405–417, February 2015. ISSN 0924-0136. doi: http://dx.doi.org/10.1016/j.jmatprotec.2014.10.007.

[14] SSAB. *Precision Steel Tube Handbook*. Second edition, 2017.

[15] Mei Zhan, Yan Wang, He Yang, and Hui Long. An analytic model for tube bending springback considering different parameter variations of ti-alloy tubes. *Journal of Materials Processing Technology*, 236:123–137, October 2016. ISSN 0924-0136. doi: 10.1016/j.jmatprotec.2016.05.008.

[16] Cheng LI, He Yang, Mei Zhan, Xu-dong XU, and Guang-jun LI. Effects of process parameters on numerical control bending process for large diameter thin-walled aluminum alloy tubes. *Transactions of Nonferrous Metals Society of China*, 19(3):668–673, June 2009. ISSN 1003-6326. doi: 10.1016/S1003-6326(08)60331-3.

[17] Linda Borchmann, Peter Frohn-Sörensen, and Bernd Engel. In situ detection and control of wrinkle formation during rotary draw bending. *Procedia Manufacturing*, 50:589–596, 2020. ISSN 2351-9789. doi: https://doi.org/10.1016/j.promfg.2020.08.106.

[18] Linda Borchmann, Christopher Kuhnhen, Peter Frohn, and Bernd Engel. Sensitivity analysis of the rotary draw bending process as a database of digital equipping support. *Procedia Manufacturing*, 29:592–599, 2019. ISSN 2351-9789. doi: 10.1016/j.promfg.2019.02.100.

[19] M. Murata, T. Kuboki, K. Takahashi, M. Goodarzi, and Y. Jin. Effect of hardening exponent on tube bending. *Journal of Materials Processing Technology*, 201(1–3):189–192, May 2008. ISSN 0924-0136. doi: https://doi.org/10.1016/j.jmatprotec.2007.11.286.

[20] H. Li, H. Yang, F.F. Song, M. Zhan, and G.J. Li. Springback characterization and behaviors of high-strength ti–3al–2.5v tube in cold rotary draw bending. *Journal of Materials Processing Technology*, 212(9):1973–1987, September 2012. ISSN 0924-0136. doi: https://doi.org/10.1016/j.jmatprotec.2012.04.022.

[21] Muhamad Sani Buang, Shahrul Azam Abdullah, and Juri Saedon. An overview of the impacts of material parameters on springback. *Applied Mechanics and Materials*, 564:323–328, June 2014. ISSN 1662-7482. doi: doi:10.4028/www.scientific.net/AMM.564.323.

[22] Ramada Aços. St 52, 2017. URL `https://www.ramada.pt/pt/produtos/acos/aa-os-de-construa-ao-ao-carbono/st-52_.html`. Accessed: 2025-05-12.

[23] Ramada Aços. R 304 - aços inoxidáveis e refractários, 2025. URL `https://www.ramada.pt/pt/produtos/acos/aa-os-inoxida-a1veis-e-refracta-a1rios/r-304_.html`. Accessed: 2025-03-05.

[24] Ramada Aços. Ft c1 – construction steel data sheet, 2022. URL `https://www.ramada.pt/ficheiros_upload/ft-c1_rev01220504165723.pdf`. Accessed: 2025-04-15.

[25] Aerometals & Alloys. Titanium cp grade 1 t35, 2025. URL `https://www.aerometals-alloys.com/produit/titane-pur-grade-1-t35/?lang=en`. Accessed: 2025-04-22.

[26] Metal Ministry Inc. About us, 2025. URL `https://www.aerospacemarinealuminiumalloy.com/about-us.html`. Accessed: 2025-04-22.

[27] Pedro Alexandre Ramiro Santos. Analysis of rotary draw bending radius using fem with experimental validation. Master's thesis, Faculty of Engineering of the University of Porto, Porto, Portugal, 2023.

[28] AMOB Group. Amob group | curvadoras de tubo, conformadoras de extremos. URL https://amobgroup.com/pt-pt.

[29] Hexagon. Bendingstudio xt, 2025. URL https://hexagon.com/products/bendingstudio. Accessed: 2025-04-24.

[30] GOM GmbH. *ATOS III Triple Scan*. GOM GmbH, 2016. URL https://www.zeiss.com/metrology/en/home.html. Technical brochure.

[31] WorldAutoSteel. Springback. https://ahssinsights.org/forming/springback/, 2021. URL https://ahssinsights.org/forming/springback/. Accessed: 2025-06-04.

Appendix A

Report of real validation from Hexagon Machine

Hexagon
Biberweg 30C
38114 Braunschweig

Result properties

General properties	
Created on	6/6/2025 4:21:06 PM

Specific properties	
Part name	Teste3
Operator name	AMOB S.A.
Result	

3D view of bending coordinates - Bending coordinates

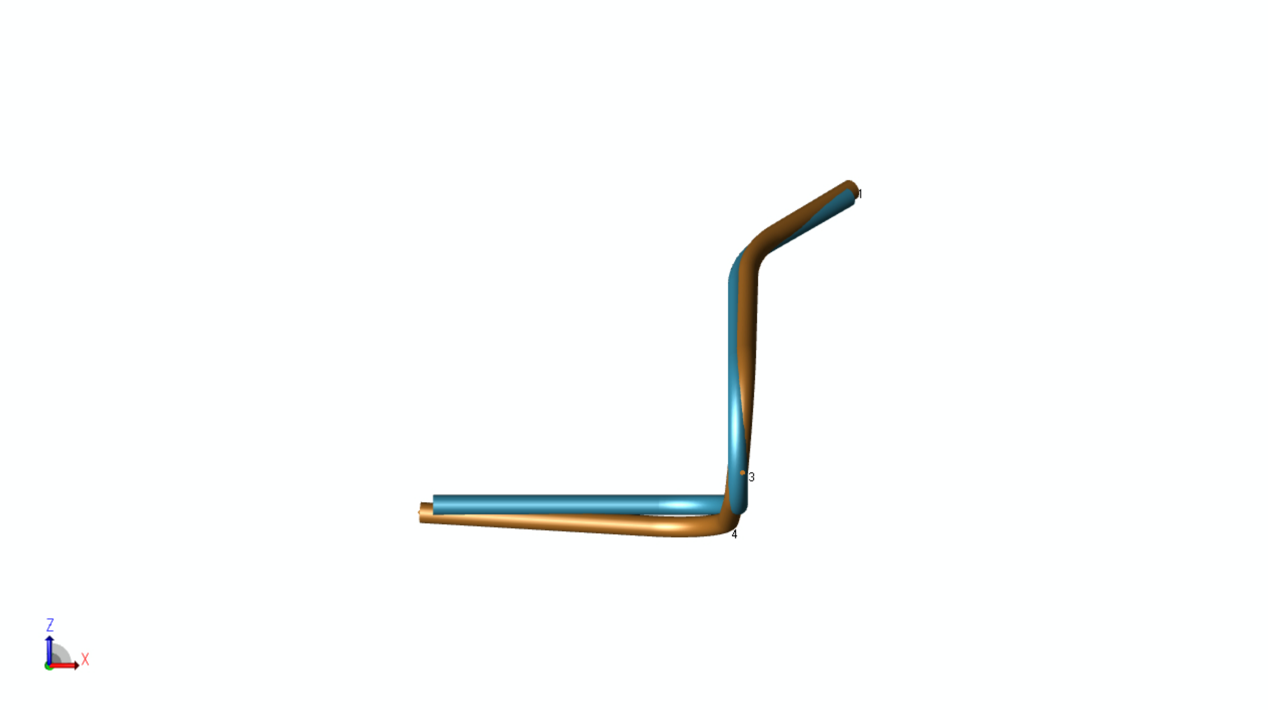

Legend	Reference tube Measured tube

Hexagon
Biberweg 30C
38114 Braunschweig

Result properties

General properties	
Result name	2025/06/06-16:21:06
Comments	

Specific properties	
Part name	Teste3
Alignment	Best-Fit_1
Inspection criteria	Sheath deviation (default)

Kontakt: Hexagon
Telefon: +49 531 58 000 58
Fax: +49 531 58 000 60

Hexagon
Biberweg 30C
38114 Braunschweig

Component properties - BentPartComp

Dimensions	30.00 mm
Wall thickness	1.50 mm
Material	-
Elasticity	-
Start adapter	Normal end
End adapter	Normal end

End length results - BentPartComp

Component	Property	Value [mm]		
		Actual	Nominal	Act-Nom
BentPartComp	End-to-end distance	816.37	783.51	32.85
BentPartComp	Rolled-out length	1,505.33	1,500.00	5.33

Bending elements - BentPartComp

No.	Length [mm]			Rotation [deg]			Angle [deg]			Radius [mm]		
	Actual	Nominal	Act-Nom	Actual	Nominal	Act-Nom	Actual	Nominal	Act-Nom	Actual	Nominal	Act-Nom
BE1	171.79	170.00	1.79	-	-	-	40.60	45.00	-4.40	174.30	160.00	14.30
BE2	199.47	200.00	-0.53	-89.63	-90.00	0.37	135.77	145.00	-9.23	126.91	120.00	6.91
BE3	171.92	170.00	1.92	-89.74	-90.00	0.26	82.89	90.00	-7.11	128.99	120.00	8.99
BE4	351.30	342.15	9.15	-	-	-	-	-	-	-	-	-